ARISTOTLE UNIVERSITY OF THESSALONIKI
Interinstitutional Program of Postgraduate Studies in
PALAEONTOLOGY – GEOBIOLOGY

Nikolaos Gerakakis
Geologist

DIGITAL IMAGING AND RECONSTRUCTION OF *HIPPOPOTAMUS CREUTZBURGI* CRANIUM (ARTIODACTYLA: HIPPOPOTAMIDAE) FROM KATHARO PLATEAU (CRETE)

MASTER THESIS

DIRECTION: Macropalaeontology
Directed by: National & Kapodistrian University of Athens

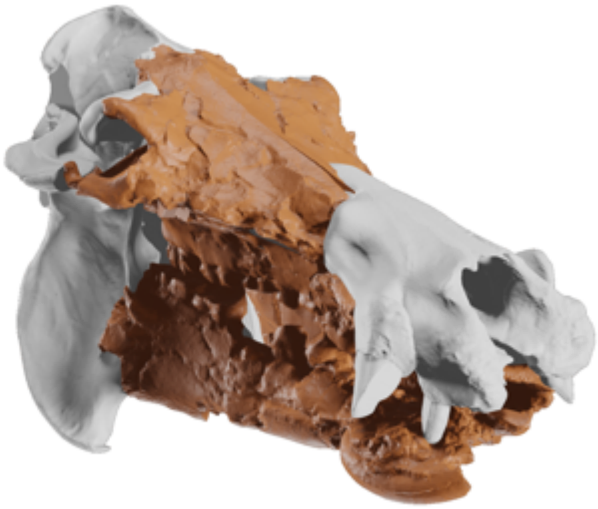

ATHENS
2023

Interinstitutional
Program of
Postgraduate
Studies in
PALAEONTOLOGY – GEOBIOLOGY

supported by:

SCHOOL OF GEOLOGY AUTH

Τμήμα Γεωλογίας ΑΠΘ
School of Geology AUTh

school of biology

Τμήμα Βιολογίας ΑΠΘ
School of Biology AUTh

National and Kapodistrian University of Athens
Faculty of Geology
and Geoenvironment

Τμήμα Γεωλογίας & Γεωπεριβάλλοντος
ΕΚΠΑ
Faculty of Geology & Geoenvironment
NKUA

Department of GEOLOGY

Τμήμα Γεωλογίας Παν/μίου Πατρών
Department of Geology, Patras Univ.

UNIVERSITY OF THE AEGEAN

Τμήμα Γεωγραφίας Παν/μίου Αιγαίου
Department of Geography, Aegean Univ.

Nikolaos Gerakakis
Νικόλαος Γερακάκης
Πτυχιούχος Γεωλογίας και Γεωπεριβάλλοντος

DIGITAL IMAGING AND RECONSTRUCTION OF *HIPPOPOTAMUS CREUTZBURGI* CRANIUM (ARTIODACTYLA: HIPPOPOTAMIDAE) FROM KATHARO PLATEAU (CRETE)

ΨΗΦΙΑΚΗ ΑΠΕΙΚΟΝΙΣΗ ΚΑΙ ΑΝΑΤΑΞΗ ΤΟΥ ΚΡΑΝΙΟΥ ΤΟΥ *HIPPOPOTAMUS CREUTZBURGI* (ARTIODACTYLA: HIPPOPOTAMIDAE) ΑΠΟ ΤΟ ΟΡΟΠΕΔΙΟ ΚΑΘΑΡΟΥ (ΚΡΗΤΗ)

Υποβλήθηκε στο ΔΠΜΣ Παλαιοντολογία-Γεωβιολογία

Ημερομηνία Προφορικής Εξέτασης: 04/07/2023
Oral Examination Date: 04/07/2023

Three-member Examining Board

Associate Professor George Lyras, Supervisor
Associate Professor Socrates Roussiakis, Member
Associate Professor Dimitrios Makris, Member

Τριμελής Εξεταστική Επιτροπή

Αναπληρωτής Καθηγητής Γεώργιος Λύρας, Επιβλέπων
Αναπληρωτής Καθηγητής Σωκράτης Ρουσιάκης, Μέλος Τριμελούς Εξεταστικής Επιτροπής
Αναπληρωτής Καθηγητής Δημήτριος Μακρής, Μέλος Τριμελούς Εξεταστικής Επιτροπής

Digital imaging and reconstruction of *Hippopotamus creutzburgi* cranium (Artiodactyla: Hippopotamidae) from Katharo plateau (Crete) – *Master Thesis*

Ψηφιακή απεικόνιση και ανάταξη του κρανίου του *Hippopotamus creutzburgi* (Artiodactyla: Hippopotamidae) από το οροπέδιο Καθαρού (Κρήτη) – *Μεταπτυχιακή Διπλωματική Εργασία*

Citation:
Gerakakis N., 2023. Digital imaging and reconstruction of *Hippopotamus creutzburgi* cranium (Artiodactyla: Hippopotamidae) from Katharó plateau (Crete). Master Thesis, Interinstitutional Program of Postgraduate Studies in Palaeontology-Geobiology. School of Geology, Aristotle University of Thessaloniki, 96 pp.

Abstract

In this study, we describe new cranial material of *Hippopotamus creutzburgi*, the endemic hippo of Crete, from the site Anáskama, located on the Katharó plateau and we digitally reconstruct the cranium of this species.

The specimens from the Katharó plateau are preserved in poor condition as they are worn and flattened, and fossils ideally should be undistorted to be studied thoroughly. Five specimens were digitized with photogrammetry using the software, Reality Capture. The retrodeformation and the composition of the final model took place in the free and open-source software, Blender. Two partial skulls and an almost complete mandible were used. We checked the validity of the reconstructed flattened skull by comparing the ratio of its height to the length of the post-canine battery with other Hippopotaminae. The ratio was placed within the area of the Malagasy hippos. To make the model more presentable we add its missing parts from a 3D model of *Hippopotamus amphibius.* We used several tools in Blender to sculpt them until they fit as well as possible. Of course, this final model is a more subjective and artistic version of this species.

We detected some new characteristics of this species based on the fossil material. On the skull, the zygomatic crest is relatively thin, the relative position of the anterior border of the orbit is above M3, the supraorbital margin is thick, and the notch on the anterior border of the orbit is deep and narrow. The nasal bones run from the level of the middle of the orbits, they are almost parallel and at the level of the anterior of the orbits diverge and then converge. Posteriorly, they create a small hollow that the anterior of the frontal bone fills.

Its teeth are big compared to the overall skull size, and the diastemas are either small or absent. The palatinum is narrower in the middle (M1-M2 area) and wider in the rostral and caudal portions. Compared to the lateral extension of the skull canine apophyses, it has a weak post-canine constriction of the muzzle. The morphology of the facial crest is consistently convex, gradually sloping postero-laterally from the zygomatic process of the frontal bone toward the maxilla. The outline of the glenoid articular area is enlarged with diffuse borders with an elongated shape. These anterior and posterior borders are not rectilinear and laterally converging.

On the mandible, the i1-i1 diastema is longer than the mesiodistal diameter of the i1. The position of the canine alveolus is at the same level or posterior relative to the incisor alveoli. The canine processes are developed. The mandibular symphysis extends posteriorly as far as the anterior of p3. The orientation of the symphysis plane is anterodorsally inclined. The alveolar walls of the lower canines are relatively thick. The gonial angle is well-developed and has a hook shape. The lateral expansion of the gonial angle is laterally warped away from the corpus direction.

Hippopotamus creutzburgi presents similar characteristics to its ancestor *Hippopotamus antiquus* as well as differences such as a thicker supraorbital margin and a shorter muzzle. Its thick supraorbital margin is a similar feature to *Hippopotamus lemerlei*. We detected a significant difference in size among some specimens that we interpreted as a possible sexual dimorphism of this species expressed in the mandible. We suggest that males have bigger, more robust mandibles with thick clades, more developed canine alveolus, and longer, more robust lower canines and incisors than females. However, molars have relatively the same size.

Table of Contents

1. Introduction

1.1. General introduction and aims of this study

During the Pleistocene, *Hippopotamus* colonized Sicily, Malta, Cyprus, Madagascar, and Crete. Those populations evolved into different endemic species, one for each island. *Hippopotamus creutzburgi* is the endemic species of Crete. It is mainly known from postcranial material and teeth from the Katharó plateau.

Raulin was the first who discovered this material, in 1845, being sold by villagers of Kritzá (Spratt, 1865). After buying some jaw fragments, he visited the Katharó plateau, the location of the material for finding more fossils, but his attempt was fruitless. The description of these fossils was made in 1847 by Blainville (Boekschoten and Sondaar, 1966). In 1904, Bate (1905) organized excavations in several places in Crete, and she was the first scientist who found and studied this species for the first time by herself. In 1965, Melentis published extra material housed at the Vienna Museum. In 1966, Boekschoten and Sondaar published their study after visiting Katharó. They revised and studied new material from the British Museum (now the Natural History Museum of London) and the Muséum d'Histoire Naturelle in Paris, respectively. They named the species and provided additional data on the fossils, the stratigraphy, and the origin of the Katharó plateau. In 1975, Kuss described material from Stavrós and Káto Zákros coastal caves, and despite the scarcity of the material, he decided to name a new smaller-sized subspecies, the *H. creutzburgi parvus*. In 1982, Capasso Barbato and colleuges described material from Katharó plateau from the 1972 expedition of A. Malatesta, C. Petronio, T. Kotsakis and V. Pattinella and later in 1996, Caloi and Palombo reviewed the same material in a morphofuctional perspective. This material included cranial remains, too. Spaan (1996) studied new postcranial material from Katharó and developed the views of the aforementioned authors.

The Katharó plateau is a location extremely rich in fossils. However, the material is preserved in poor condition as it is worn and flattened, and fossils ideally should be undistorted to be studied thoroughly. It is considered a lacustrine basin between mountains at an altitude of 1,100 m (Boekschoten and Sondaar, 1966). For the extant common *Hippopotamus amphibius*, passing through all these rocky hillsides would be an unrequited dream, though for *H. creutzburgi* was routine. It was adapted to walking more tiptoed than its mainland ancestor, *H. antiquus*. Its highly adapted pes and manus to the rocky environment of Katharó made it look different from any other known extant or extinct hippo and more like a goat (van der Geer et al., 2010). Thus far, no detailed description of the cranium has been published.

There is an abundance of new material found during the 1998-2004 excavations on the site "Anáskama" in the Katharó plateau led by Dermitzakis and Pavlakis, including specimens of the cranial skeleton, that would add more information about this species, remaining unpublished to date. Questions about the morphology and the cranial adaptions of this species can be answered with the present material. We decided to process our material digitally to extract as much information as possible and to ensure the integrity of the specimens.

This thesis describes new cranial material of *H. creutzburgi*. The cranial material used in this study is the most numerous and the best yet found. For the first time, we reconstruct almost the whole cranium of this species by producing a digital 3D model of the skull and mandible joining parts of different specimens.

What did this hippo look like; how much was differentiated from its ancestor, *H. antiquus*, and the extant *Hippopotamus amphibius*; are there any differences and similarities to the cranium of other endemic species of the Mediterranean and Madagascar; these are some of the questions answered in this study.

1.2. Virtual palaeontology

In 2014, Sutton and colleagues defined the term "Virtual Palaeontology" as the study of 3D fossils that have been digitally visualised. There are several techniques with many advantages in comparison to the classical palaeontology methods of study. The most important step for successful research with the use of virtual palaeontology is the choice of the ideal technique for the samples. The two main approaches of these techniques are tomography and surface-based methods (Sutton et al., 2014). Tomography uses 2D slices extracted from a 3D specimen with a tomograph, either by serial grinding or X-rays, or other more sophisticated methods (Sutton et al., 2017). The whole set of the slices is called "tomographic dataset" and an individual slice is called "tomogram".

Tomography have been used in Palaeontology since the early 20th century. William Sollas introduced a manual serial grinding technique for fossils that were preserved in rock. His tomograph was operating at intervals of 25 μm. He was taking photos of the exposed surfaces and manually tracing them from glass photographic plates. Sollas was also making several serial 2D slices from bee wax and combining them to produce a physical 3D model by cutting, stacking, and heating them until they fused. He was making similar models with cardboard and polystyrene, too. This method is intensely time-consuming, and Erik Jarvik proved it by spending 25 years making a wax model of *Eusthenopteron* using 500 detailed drawings. Besides being time-consuming, this method is also destructive. To expose the different surfaces to sketch or photograph them the use of a saw is necessary (Cunningham et al., 2014). Technology came to overcome all these drawbacks.

Nowadays, most of the techniques being used are non-destructive, less time-consuming, and more accessible year after year. The most common are those using X-Rays. A significant problem in palaeontology is the difficulty of preparing certain fossils, either because they are inside a rock and not accessible without destroying some parts or because they are too sensitive. After the X-rays discovery in 1895, palaeontologists began to experiment with solving the problem of fossil examination, which are not easy to prepare. At the end of the 20th century, a combination of tomography and X-ray techniques was a fact. The result was Computed Tomography (CT) which is widely used in palaeontology. These methods, excluding the ability to study the external surface, are ideal for examining the interior of a specimen, too. Surface-based techniques focus on the external geometry by digitizing it using a variety of scanners or photogrammetry, and the study of the interior is impossible.

There are several techniques available to help palaeontologists with their research. Tomographic methods are divided between traditional destructive (e.g., serial griding) and modern non-destructive methods (e.g., CT scanning). Surface-based methods are divided between contact and non-contact.

1.2.1. Tomography

i. Destructive Tomography

The characteristic of this category is that the fossil is entirely or partially destroyed at the end of the process. This is the biggest drawback of these methods because although there is a final product, it could never be as perfect as the original was. Lost data, lack of information, errors, and mishaps are the main problems in the production of the final model. Another drawback is that they consume a great amount of time and have high labour requirements. Sometimes, these techniques cannot be avoided. A well-known case is the Herefordshire Lagerstätte (Briggs et al., 2008). Fossils from this area are X-ray attenuated, so CT scanning is useless, optical tomography cannot be selected due to the high opaque of the material, and their small size excludes them from other techniques.

Physical-optical tomography

This term was invented by Sutton (2008), who categorized the different methods used by palaeontologists. The physical exposure of the sections and the imaging of those surfaces were necessary for tomogram creation.

Serial grinding is the most common approach. A custom-made apparatus was used by Sollas (1903) to grind some of the material, around 10μm to 1mm, and then the exposed surface was photographed. In the final step, the structure was manually traced from the photos. Simpler equipment, like a glass plate with abrasive powder, could also be used. The modern version of the technique uses lapping machines that produce thin sections. Those methods are time-consuming, and by the end of the process, the specimen is destroyed. However, they create high-resolution reconstructions due to the small spaces between the tomograms.

Serial sawing was another method that Sollas used to make tomograms. This method uses an annular or a diamond wire saw and is less destructive. The lost material is about 200-300μm thick. Every type of saw has a different price range and speed. Fine-bladed saws are cheap, work at low speeds, and have kerfs smaller than 0.4mm. The process takes a lot of time and is limited to small specimens (only a few cm). More expensive fine-bladed saws are just faster. Wire saws can cut larger specimens but are pricey and more time-consuming. Sawing has lower resolution results compared to gridding but sometimes could be the only option, especially for large specimens. Serial slicing is a similar technique capable of very high resolution, but it uses a microtome blade and is applied to soft specimens.

Sollas also found a way to record the tomographs permanently. He used cellulose acetate peels, but even the best-made ones are prone to wrinkles, or other destructions, which render their digitizing impossible.

Focused Ion Beam tomography (FIB)

This method uses a lab-based tool with extremely high resolution, the FIB, which can mill and image small specimens (<5nm). In palaeontology, it is used for providing data on the crystallographic structure of the specimen. It requires up to an hour for a tomogram and the specimen is destroyed.

ii. Non-destructive tomography

Tomographic datasets are being created without visible light penetration or physical exposure of surfaces but with the use of electromagnetic radiation or subatomic particles. They interact with the specimen generating no damage or causing minimum damage during the preparation stage to achieve extremely high-resolution tomograms. This condition ensures that the samples will be available for future studies. Another advantage of these methods is that they are less time-consuming. The most widespread of all the forms is the X-ray CT, specifically micro-CT scanning. A CT scanner collects X-radiographs of a specimen from different angles and then computes the tomographic dataset (Abel et al., 2012). Micro CT scanners have a resolution of 1 μm and can scan specimens with a diameter of up to 200 mm. A source generates X-rays transmitted through the specimen and recorded by an X-ray detector as a 2D projection image.

Medical and other scanners rotate the X-ray source and the detector around the object, which is stable. This process is repeated while the sample rotates by a degree until it makes a 180° turn or even 360° for more complicated samples. Subsequently, these images are computed into tomograms cross-sectional images, namely, tomograms with specific algorithms. Tomographic datasets are 3D maps of X-ray attenuation of the interior of a sample, which is linked to the atomic number and the mass density variations. This is very useful in the differentiation process of the fossil from the host rock or sediment.

Medical CT

The specimen is placed on a table that gets through a rotating tube while a row of detectors inside the gantry measures the X-ray attenuation. The position of the sensors allows them to collect multiple slices at the same time. The resolution range is in millimetres, though it can be improved by using specialized spiral scanners. These scanners are great for bigger size vertebrate specimens.

Micro and nano CT

In this method, the specimen is mounted to foam on the rotation stage with its longest axis vertically for easier penetration of the beams. The specimen starts rotating, polychromatic X-rays from the source penetrate it, and a 2D detector panel array collects the radiographs. The target material, the voltage and the current of the X-rays source, the exposure time of the specimen, its distance from the source, and the number of projections and frames, are important adjustable parameters depending on the specimen. The use of the lowest possible energy X-rays is the suggestion of Sutton et al. (2014). There are lab-based CT scanners with resolutions from 1μm to 50nm. The resolution is linked to the size of the object, the X-ray focal spot size, and the use of additional optics.

Synchrotron CT

It is a cyclic particle accelerator in which the accelerating particle beam travels around a fixed closed-loop path and produces extremely powerful X-rays. The well-known synchrotron of CERN was built in 2008. It is enormous, with a circumference of 27 km. Synchrotrons produce a powerful monochromatic parallel beam that creates high-resolution tomographic datasets. Except for attenuation maps, synchrotrons can produce phase shift maps of the X-ray beam based on the refraction within a sample. This is very helpful for specimens with low attenuation contrast. The resolution that can be achieved is 200 nm, and the features that can be imaged with this technique range from 50 μm to 600 mm (Cunningham et al., 2014).

1.2.2. Surface-based methods

They are non-destructive techniques that capture the 3D topology of an object (Sutton et al., 2014). These techniques are more accessible and widespread due to their relatively low cost, rapidity, and simplicity. Contrary to the tomographic techniques, they cannot capture the interior of a specimen, although most of them capture the surface colour. For the best results in palaeontology, specimens must be prepared and isolated from their matrix to get the surface right. These methods are mainly used in vertebrate palaeontology (Sutton et al., 2017).

Laser scanning

Nowadays, it is the surface-based technique used by palaeontologists the most. There is a variety of scanners. For example, handheld scanners are ideal for smaller samples such as vertebrate bones, while long-range systems, e.g., LiDAR, can scan whole areas and are valuable in capturing excavation sites. They use laser light to define the 3D positions of surface points as coordinates, creating a final point cloud. A combination of scanning and digital photography can produce point clouds with colour. Laser scanners are divided into three categories based on their operational principles: triangulation, time-of-flight, and phase shift.

Triangulation-based scanners project a laser light spot or strip to an object. Then a sensor, located next to the source shaping a right triangle with it and the object, receives the reflected light. For the definition of the position of the points, the distance between the source and the sensor, as well as the angles at which the laser light hits the object, and the reflected light on the sensor, is calculated. To scan the whole object, there are scanners with beams that scan it automatically and others with a turntable rotating it. Handheld scanners (e.g., ZScan 700CX 3D) belong to this category. Their scanning resolution is up to 0.1 mm on the Z axis and up to 50 μm accuracy in XY and can also capture texture colour. Two laser beams placed at a right angle are projected onto the item for faster and denser coverage. They usually scan specimens smaller than 1 m. However, they can scan larger objects or different sides of them in multiple parts. These sub-parts should overlap to be positioned in one triangulated mesh with a texture map. The incapability of scanning shiny folding surfaces is a drawback of this method (Makris et al., 2018).

Time-of-flight scanners work by sending out a short pulse of laser light to the object and detecting the reflected light with a sensor. The distance from the object for a specific surface point is calculated by dividing the reflecting time by two and multiplying it by the speed of light. This process is repeated until the whole specimen is captured. They can image a wide range of objects from millimetres to entire sites terrestrially or airily. These scanners have been used for capturing large trackside like dinosaur trackways (e.g., Bates et al., 2008) and gigantic skeletons.

Phase-shift scanners work like turn-of-flight scanners but with a sinusoidally modulated beam power. To calculate the distance with the specimen, they compare the phase of the reflected beam with the emitted one. They are capable of fast imaging large surfaces but are rarely used in paleontological applications (e.g., Haring et al., 2009).

Mechanical digitization

This method uses a mechanical arm (e.g., MicroScribe) with sensors at each joint, and a digitizing tip. The tip records the 3D coordinates of the several landmarks. The digitization of a sample is done by moving the tip to several points on the surface of the specimen. Mechanical digitization is widespread for morphometric studies for collecting landmark data (Green and Alemseged, 2012), while some researchers use it to capture data for virtual palaeontology, too (Mallison et al., 2009). It is a relatively cheap method with easy and fast operation. The accuracy of this technique is lower than that of laser scanning and photogrammetry, as well as the point density, but its files are much smaller. However, the final model lacks colour. It is best applied to large, robust specimens to avoid damaging them by contact with the tip.

Photogrammetry

Photogrammetry uses 2D photos to image the 3D surface of an object or an area. This method can be divided into close-range and aerial photogrammetry, accordingly to how the pictures are photographed.

This method begins in the early-mid 19th century with the invention of photography and the development of stereoscopic viewing. It was used for aerial mapping and reconnaissance during the First and Second World Wars. The widespread came with the invention of the computer and the digital camera. Nowadays, digital photogrammetry constitutes a tool for different scientific fields such as architecture, cartography, archaeology, and palaeontology.

Photogrammetry works by finding homologous points on overlapping images from different positions of the same object to reconstruct a point cloud. The overlap of the photos must be at least 66% (Falkingham, 2012), or the software could experience problems with the aligning process. This method also captures the colour and the texture from the surface of the object and integrates them into the final 3D model.

In close-range photogrammetry, a tripod for mounting the camera is suggested, as well as the placement of the object on a turntable for easier turning. For big objects, the photographer must turn around the specimen capturing every side of it. Achieving high-quality results requires consistent lighting and as many photos as possible (>100) than a high-end digital camera with an expensive lens. Modern smartphones have appropriate cameras, too. Point-cloud reconstruction is automated using paid (Agisoft Metashape, Reality Capture etc.) or open-source software (VisualSFM, Meshroom).

The time of reconstruction depends directly on the hardware of the computer. Also, more photos with higher resolution equal more processing time. The final models of this method sometimes have even higher resolution than models from laser scanning. However, the final model requires scaling. Photogrammetry with a digital camera works on specimens bigger than 10 mm. For smaller specimens, taking photos from a microscope may be a solution (Sutton et al., 2014). The continuous improvement of digital cameras, computers, and photogrammetry software has led to an increase in the usage of this method in many sciences making photogrammetry the number-one choice for surface digitizing (Díaz et al., 2021).

Aerial photogrammetry is operated with drones, and it is automated and fast. In palaeontology, except for digitizing excavation sites or trackways, it could be used for giant skeletons with some restrictions, but there are no such examples.

Easy access and exchange of 3D models were the main reasons for creating virtual collections such as SketchFab, MorphoSource, DigiMorph, etc. However, a minority of palaeontological specimens are being uploaded to these collections.

1.3. Island Endemism

1.3.1. The island rule and factors affecting size reduction

Thousand years before, the Mediterranean fauna was not the same as today. Remarkable creatures used to live and evolve in different Mediterranean islands. These species living in isolation were following the island rule (Van Valen, 1973). According to this rule, small species tend to become bigger, and large species tend to become smaller. Several factors play a significant role in the formation of endemic faunas. The type of island, the possible ways that animals can colonize it, how far it is from the mainland, and of course, the relief, the climate, and the physiography of the island.

There are three main ways of dispersal for vertebrate mammals: over land, over water, and through the air. The first type is possible for every animal except for the aquatic taxa. The second type is possible only for animals that they can swim, float or travel on floating masses (e.g., woods), the last type refers to bats. In addition, it is essential to be capable of surviving a trip on the open sea, concerning the long time it may need. Few taxa appear to be successful colonizers. Continental islands, it is the easiest destination, and practically all taxa can arrive. Oceanic islands, on the other hand, can be colonized only by large herbivores like deer, hippopotamuses, proboscideans and by rodents, bats, and some reptiles. After their arrival, they must deal with living in a different habitat. So, colonization it is not the easiest way of living, and only a few taxa can finally adapt and evolve into endemic forms (van der Geer et al., 2010).

More island area tends to increase the number of species (Lomolino, 2000). Cyprus and Crete are the largest islands in the Eastern Mediterranean and the only ones with more than one elephant species. These two elephant species are not contemporaneous. In Crete, there are two endemic faunas in two different periods: an Early-early Middle Pleistocene one, composed of *Mammuthus creticus* and *Hippopotamus creutzburgi*, and one from the late Middle-Late Pleistocene, composed of the bigger Cretan elephant *Palaeoloxodon creutzburgi* and eight cervid species (de Vos, 1979; de Vos and Dermitzakis, 1986; Poulakakis et al., 2002; van der Geer, 2018). Even islands that are considered large like Crete and Cyprus are not capable of supporting two proboscidean species and this is a common fact worldwide, too (Athanassiou et al., 2019).

The degree of isolation is not correlated with the degree of body size reduction (van der Geer et al., 2016). However, there is a correlation between island isolation and body size reduction. It is necessary to say that every dwarf species lived on paleo-islands that used to be at least 10 km far from the mainland, except for *Palaeoloxodon mnaidriensis* from Sicily. In the case of the elephants from Kythera and Kefalonia, where elephants were normal-sized, the explanation is that these islands were too close to the mainland, and when the sea was at a lower level, the distance was approximately 4-6 km (van der Geer et al., 2016). Nowadays, Asian elephants cross 2-3 km daily, but their dispersal ability is way larger (Johnson, 1980). Due to that fact, the island population was not completely isolated, and there was a high gene flow between them, so the population of the mainland and their phenotype remained the same.

In 2016, van der Geer and colleagues after a statistical analysis suggested that the existence of competitors can have a noticeable effect on endemic faunas. This is clear in most cases, but there are some exceptions. In Crete, the endemic elephants had to compete with several deer species, and as a result, their size was not as reduced as the elephants from Cyprus, which are about the same size, and elephants had no competitors. Tílos is an interesting case, though, as the smallest island with endemic elephants worldwide. *Palaeoloxodon tiliensis* was expected to be the smallest one ever found if we consider only the size of the island, but it is not (Athanassiou et al., 2019).

1.3.2. Abilities of a great colonizer

Swimming

Evidence from fossil faunas indicates that pachyderms and deer were successful in colonizing oceanic and oceanic-like islands. They are great marine swimmers, and gasses being produced by their digestive systems provide them with better buoyancy. The proboscis of an elephant can be used like a snorkel expanding its time in the water, making its living more comfortable, and providing better chances to survive. Proboscidean fossils are present on several islands. For example, extinct elephants have been found on several islands in the Aegean Sea, plus mammoths and elephants from Crete. Hippos reached Cyprus and Malta, while deer reached Kárpathos and Crete. The excellent swimming capacities of proboscideans and deer can be probably explained by the existence of an aquatic ancestry. Hippos are aquatic mammals though they are not swimmers. In the sea, they float, and in their usual habitats (lakes, rivers), they ‘walk’ over the bottom. Carnivores can swim while they lack the floating capacity. Endemic otters, which are frequently present in endemic fossil faunas, are an exception (van der Geer et al., 2010).

Holding over

In the beginning, the population of a disconnecting area is the same as the mainland. The gradual extinction of the taxa begins after the disruption, either because they are less adaptable and do not fit in the new environment or because there is not enough food. The latter cause answers the question of why there are no endemic top predators, they disappear first. Only a few taxa can survive longer, and these are especially small bovids. Other common taxa found on endemic faunas are pigs, moles, and lagomorphs (van der Geer et al., 2010).

1.3.3. Craniodental changes occurring during dwarfism

Generally, in vertebrates, as the size of the animal increases, the neurocranium becomes proportionally smaller in contrast to the muzzle, which becomes proportionally larger (Weston, 2003). This general pattern of cranial growth could be interpreted as structures having positive allometric growth increasing their size rapidly in the early ontogenetic stages, as the brain, but later shifting to isometric or negative allometric growth (Emerson and Brambe, 1993). The increase in overall size is focused on postnatal development (Ravosa, 1991). Therefore, brain size does not change significantly compared to facial structures (Weston, 2003). The increase or decrease of the evolutionary size is accomplished through maintaining ancestral growth patterns (Weston, 2003).

Lack of strong pneumatization is common in dwarf proboscideans such as *P. falconeri*, *Mammuthus creticus* (Bate, 1907)*, Mamuthus exilis* (Agenbroad et al., 1994), and *Stegoloxodon celebensis* (Hooijer, 1949). A short muzzle is a feature of many insular endemics. These endemics, *H. minor, M. batei, N. melonii, C. sardous, S. sondaari*, have more arcuate maxillary tooth row and loss or reduction of (pre)molars (van der Geer, 2014). Others, like *Gymnesicolagus gelaberti* and *Nuralagus rex*, combine short muzzles with short diastema with or without loss of m3, respectively (van der Geer, 2014). Short snout or reduced prognathism is also observed in *H. floresiensis* (Kaifu et al., 2011).

The relative size of the brain can be the same as their mainland ancestors*, Candiacevus* spp. II (Lyras et al., 2009), smaller as *H. minor* (Lyras, 2018)*, H. madagascariensis and H. lemerlei* (Weston and Lister, 2009; Lyras, 2018) or larger, as *P. falconeri* (Palombo, 2001). Dwarf hippos have relatively smaller brains than the average mammal of the same size, contrary to dwarf elephants, which have relatively larger brains (Lyras, 2018). Although the relative brain size of insular hippopotamuses is slightly larger than that of *H. amphibius*, it does not reach the value of the pygmy hippo, *Choeropsis liberiensis* (Lyras, 2018). Another trend could be more frontally oriented orbits like in *H. minor* (van der Geer, 2014) and *M. balearicus* (Alconer et al., 1981) as well as not reduced, in *H. floresiensis*, or larger orbit area in the Malagasy hippos compared to their ancestors (Weston and Lister, 2009).

The endocranial capacity of the Malagasy hippos was smaller than predicted according to the ontogenetic model of *H. amphibius*. The example provided by Weston and Lister (2009), later confirmed by Lyras (2018), suggests that insular dwarfing does not necessarily comply with predictions based on the ontogenetic scaling of the mainland ancestor. Reduced duration of rapid early brain growth could explain a “grade shift” in phyletic dwarfs to a lower brain-body ratio (Weston and Lister, 2009), and van der Geer (2014) suggested that dwarfism is likely established by a reduction of growth speed and not by curtailment of growth length.

1.3.4. Endemic Hippopotaminae

In the Pleistocene, hippos colonized the Mediterranean islands. These populations developed specialized and variable morphological characteristics and size variations that made them unique compared to their continental ancestors. Endemic forms have been described from Crete, *H. creutzburgi*, and Cyprus, *H. minor*. The forms from Sicily and Malta, *H. pentlandi* (von Meyer) and *H. pentlandi* and *H. melitensis*, respectively, display the minimum body size reduction. There is also one form from Sardinia, but this form is still doubtful. The ancestral species of *H. creutzburgi* seems to be *H. antiquus* (Marra, 2005; Sondaar and Van der Geer, 2005), whereas *H. pentlandi and H. melitensis* from Sicily and Malta may have as an ancestral form other hippos from the Middle and Late Pleistocene of Europe. The ancestor of *Hippopotamus minor*, as the result of ancient DNA analysis, is the *Hippopotamus amphibius* (Psonis et al., 2021).

Hippopotamus creutzburgi is a dwarf form from Crete which is larger than the one from Cyprus but smaller than the one from Malta. Its hypsodont dentition might be a sign of feeding on hard plants (Caloi and Palombo, 1994). Bethune and colleagues (2019) suggest a similar diet of *H. creutzburgi* to *H. amphibius* due to their matching enamel surface textures. An almost complete skeleton of *Hippopotamus pentlandi* was found in Grotta della Cannita near Palermo in 1955, and it is the bigger hippo ever found in the Mediterranean islands. More of its remains have been found later in the 1980s at Acquedolci in Sicily. This hippo is alike to *Hippopotamus amphibius* from the mainland except for its slightly reduced size, but its large size variability is a common feature of insular species.

Hippopotamus minor has dental modifications that suggest a different type of nutrition Caloi and Palombo, 1985). Lophodont molars suggest feeding on sprouts, leaves, and small shrubs. Of course, a different type of nutrition means a different type and mode of intake and mastication of food. Additional hints such as the conformation of the snout, the masseter muscle insertions, and the loss of P4 confirm this hypothesis (Boekschoten and Sondaar, 1972; Caloi and Palombo, 1994; Boisserie et al., 2011). Its dentition belongs to the lophodont type and indicates that this animal was more a browser than a grazer, exactly the opposite of its ancestor, *H. amphibius* (van der Geer et al., 2010). This character is an environmental adaption and not a retention of an older character, it is a typical character of older hippos, though, and in combination with other characters, it is indicated that this hippo had probably shifted towards a niche similar to deer. The lophodonty and brachydonty adaptions classify *H. minor* as a terrestrial browser (Bethune et al., 2019).

The most remarkable modifications in endemic hippos are observed in the post-cranial skeleton. *Hippopotamus creutzburgi* had developed different walking characteristics from its ancestor, which emphasize more on its hooves and less on its footpad. This is probably an adaption to a less aquatic environment, like the rockier one of the Katharó (Boekschoten and Sondaar, 1966). Compared to *H. antiquus*, its humerus was noticeably longer, although its radius, the pes, and manus were relatively shorter. In addition, the knee, the femur, and the tibia were less vertically arranged than *H. antiquus* (Spaan,1996). *Hippopotamus minor* from Cyprus was the most adapted insular species with outstanding biometric and morphological variations mostly in its limb bones and the autopodium (Houtekamer and Sondaar, 1979; Caloi and Palombo, 1985). To reduce lateral skidding joints of the limb had the appropriate shape that allow wide anteroposterior movements, but it was not a good runner. Better stability was succeeded with short phalanges and specific inclination of the joint surfaces (Caloi and Palombo, 1994). These modifications indicate fast adaptation due to environmental stress because of uneven ground and the lack of marshes and waterways. It preferred to live beside the water, but it also had a climbing aptitude that allowed moving on uneven grounds. Its very small body size could be explained by the absence of both terrestrial predators and food competitors (Marra, 2005).

David Reese (1974) suggested and later Alan Simmons (1988) repeated that may the arrival of humans in Cyprus during the transition from Pleistocene to Holocene is the reason behind the extinction of hippos, but this suggestion is still debated. Falconer believed that all the dwarf hippos from Malta, Sicily, and Crete belonged to the same species, *H. pentlandi*. Nowadays, every island has a species with a unique name.

The effects of island endemism on large animals seem to be size reduction, limb modifications, and different diets. The size reduction does not depend on how far an island from the mainland is but on the size of the island, the presence of competitors that occupy the same ecological niche, and the time in isolation. However, a great distance from the mainland does not allow genetic contact between the parent and the insular populations, so there is a better chance of evolving in endemic fauna and new species. Species tend to adapt to different environments and evolve limbs adapted to soft or hard grounds. Finally, insular populations tend to develop different nutrition to survive, and as a result, species could evolve hypsodonty as an environmental adaptation to a hard-plant-based diet.

1.4. Crete

1.4.1. Pleistocene biozones of Crete

There are two main biozones in the Pleistocene of Crete based on the species of Muridae (Dermitzakis, 1977; Lax, 1996; Iliopoulos et al., 2010). The replacement of *Mammuthus creticus*, the Cretan dwarf mammoth, and *Hippopotamus creutzburgi*, the dwarf hippo by the Cretan deer and the dwarf elephant, indicates the major faunal turnover during that period. Mayhew (1977, 1996) recognized three and two subzones, respectively, related to the phylogeny of the murids. The endemic genus *Kritimys* was the oldest and was replaced by the genus *Mus*, the common mouse. According to Mahyew's findings in Stavrós cave, there was an overlap of the two biozones indicated by *Mus bateae* fossils that were found together with *Kritimys catreus* (Fig. 1).

i. The *Kritimys* zone – Early-early Middle Pleistocene

The fauna of this zone includes the endemic giant mouse, *Kritimys*, with two or three species depending on the period, *Mammuthus creticus*, *Hippopotamus creutzburgi,* a turtle, *Mauremys* cf. *capsica*, and a frog, *Pelophylax* cf. *ridibundus*. After AAR and ESR dating using fragments of hippopotamus molars from Katharó, the absolute date of these zone ranges between 375 and 850 Ka (Lax, 1996). A radiocarbon dating was also performed on a hippopotamus bone from the same location, and the age indicated was 12,500 Ka. In 1996, David Reese and colleagues rejected that age as unreliable based on the geology of the site and the tooth enamel dating.

Sitía is the oldest Pleistocene locality in Crete and includes the earliest findings of hippopotamus fossils and the earliest form of the genus *Kritimys*. In younger locations, the dwarf hippo is found together with the middle *Kritimys* species, never with the younger giant form or representatives of the genus *Mus* (van der Geer et al., 2021). *Mammuthus creticus* was present from the biggening of the *Kritimys* zone, indicated by a *Kritimys kiridus* jaw found attached to its molar (Mol et al., 1996). The two or three species of *Kritimys* were never found together, so a lineage formed from the oldest *K.* cf. *kiridus* to the youngest *K. catreus* (van der Geer et al., 2021).

ii. The *Mus* zone – late Middle-Late Pleistocene

The fauna of this zone includes two species of mice, *Mus bateae* and the larger, younger *Mus minotaurus*, a dwarf elephant, *Palaeoloxodon creutzburgi*, eight species of deer, *Candiacervus* spp., an otter *Lutrogale cretensis* and a shrew, *Crocidura zimmermanni.* Except for mammals, there are reptiles like an endemic tortoise, *Testudo marginata cretensis,* and birds like the endemic *Athena cretensis*, a long-legged walking owl, and *Aquila chrysaetos simurgh* an endemic giant golden eagle among to continental birds (van der Geer et al., 2021).

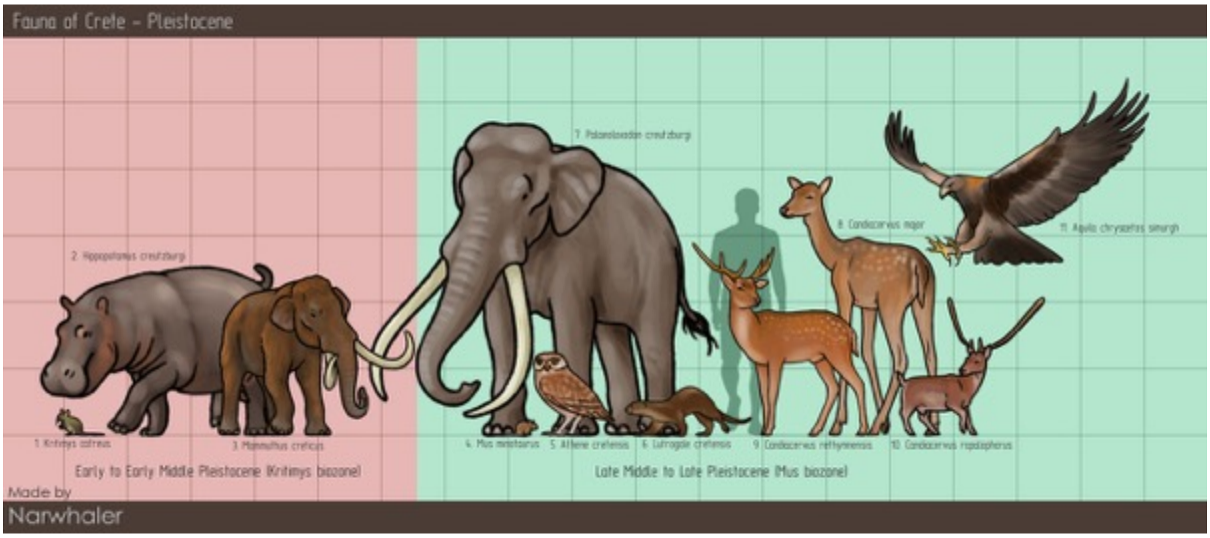

Figure 1. The two biozones of Crete. The *Kritimys* zone (left) and the *Mus* zone (right). The illustration was made by Narwhaler. Source: www.deviantart.com.

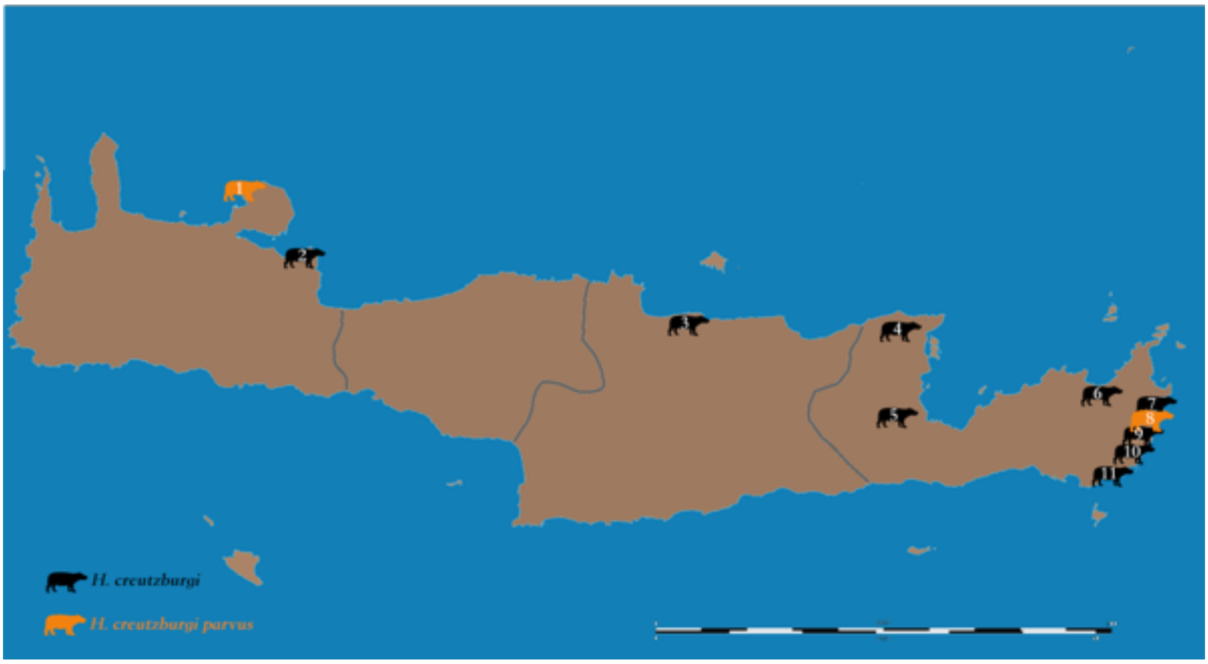

Figure 2. Simplified map with the Pleistocene localities of Crete with fossils of *H. creutzburgi* and *H. creutzburgi parvus*. **1** Stavrós Cave, **2** Koutalás Cave, **3** Mastabás, **4** Mílatos Caves, **5** Katharó Plateau, **6** Sitía I, **7** Karoúbes I, IV, V, **8** Káto Zákros, **9** Xerókambos, **10** Katharádes, **11** Alogarás. The map was made by modifying a file obtained from Wikimedia Commons using GIMP v. 2.10.34 : https://commons.wikimedia.org/, Hippopotamus figure source: http://phylopic.org/, localities are based on maps of Iliopoulos et al., 2010 and Lyras et al., 2021.

1.4.2. Katharó plateau

Katharó is located in the Lassíthi regional unit of eastern Crete. It is a basin-shaped flat terrain with a 4 km length and 1.5 km width, and an average altitude of 1,100 m, surrounded by Díkti mountains. The basin is a polje (Psarianos, 1961). Pleistocene sediments are detected on a few parts of the bottom of the valley (Boekschoten and Sondaar, 1966). On the northeastern side of Katharó, there are mountains consisting of Miocene well-sorted coarse-grained conglomerates with a white limestone matrix. The age was indicated by the fossils found in this formation, such as *Cerithium dertonense*, and *Terebralia bidentata*. The other mountains that encircle the plateau consist of limestone of Middle Pleistocene age (Boekschoten and Sondaar, 1966). Molar fragments of the hippo were dated with ESR and AAR between 375 Ka to 800 Ka (Lax, 1996). The Pleistocene sediments consist of clays, clayey sands, and angular gravel with a maximum thickness of 20 m. The consistency of the sands is mostly rounded grains, but there are also more angular quartz grains in the coarser part of the sediments. Grains of micaceous shales, cherts, steatite, diabase, and muscovite can be found, too (Boekschoten and Sondaar, 1966). These sediments were characterized as lacustrine (Boekschoten and Sondaar, 1966).

Figure 3. Profile of the Pleistocene deposits of the Katharó plateau consisting of poorly sorted grey and brown sediments of sand and clay. *Hippopotamus* fossils are found on the lower levels. Photo from: van der Geer et al., 2011.

Figure 4. Holotype of *H. creutzburgi*. Fragmented maxilla with P4-M3 (specimen NHMUK PV M 10286) housed at the National History Museum of London. Source: https://www.gbif.org/occurrence/1057354514

Figure 5. Fragmented skull (specimen MPUR/V 2031) in ventral view housed at the Museo di Paleontologia dell Università di Napoli Federico II. Photo: Caloi and Palombo, 1996.

Anáskama site

Anáskama was a new site discovered during the excavations in 1998. At this site 230 cranial and 274 post-cranial fossils of *H. creutzburgi* were uncovered since now. The area of the site is 95 m^2, and its depth of exposure exceeds 1 m. The site contains a large concentration of fossils that appear aligned in a particular direction, and several limb fragments have been discovered in their correct anatomical position. Additionally, the use of ESR dating on four tooth fragments, executed by Henry Schwarcz, resulted in an estimated age of 365 ± 50 Ka (Dermitzakis et al., 2005).

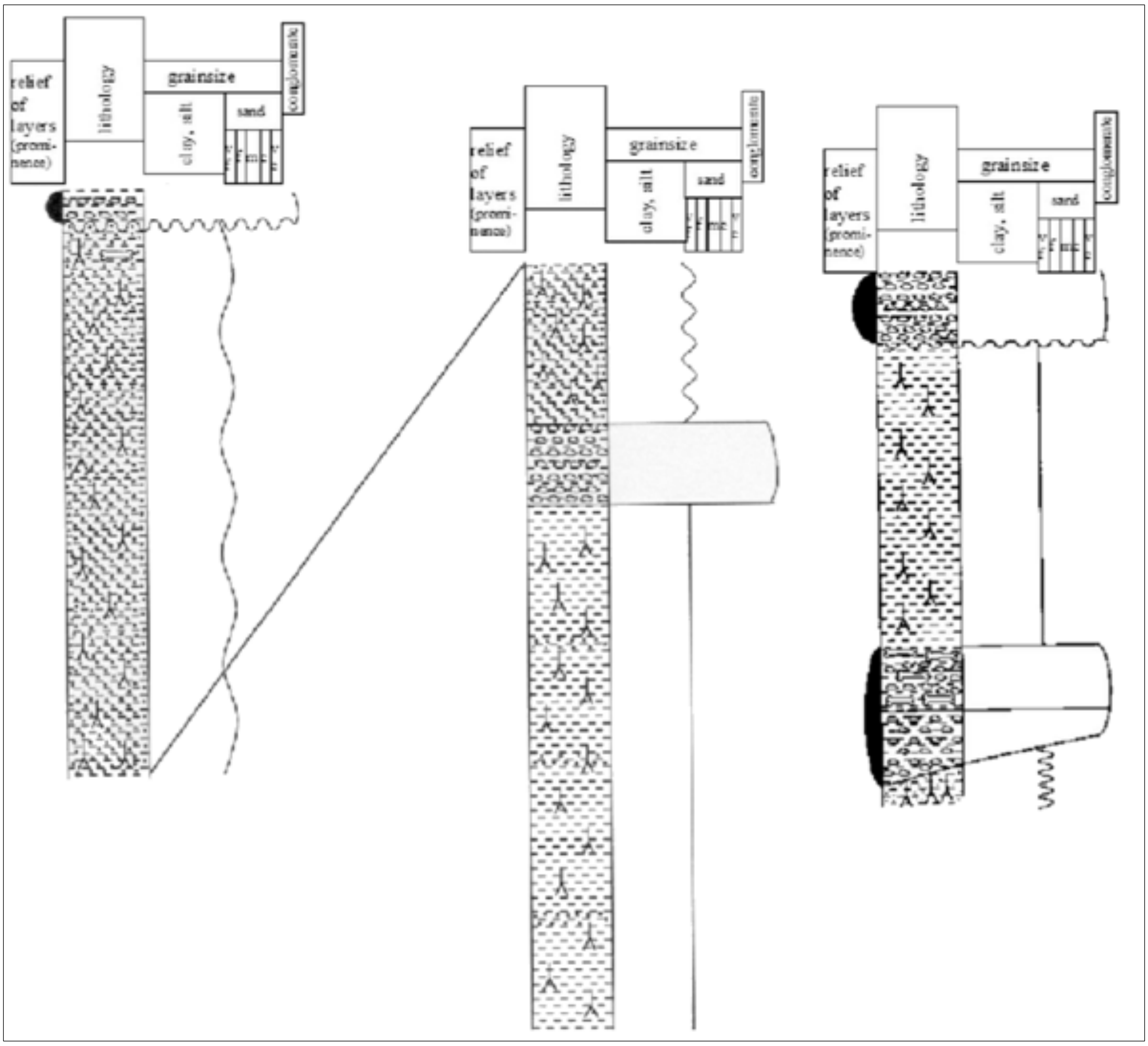

Figure 6. Profiles near the site Anáskama in Katharó plateau drawn by Hannie de Visser in 2001 (van der Geer and Lyras, 2011).

2. Material and methods

2.1. Material

Our sample comprises three differently preserved partial skulls, an almost complete mandible, and several fragments of *H. creutzburgi* from the site Anáskama on the Katharó plateau. KA-A-109 is housed at the Museum of Palaeontology and Geology in the University of Athens (AMPG). The specimen is a partial skull of an adult *H. creutzburgi* preserving the left teeth row P4-M3 and the right P3-M3 (Fig. 7, 8, 9). A broken part of KA-A-109 is housed at the AMPG. This specimen preserving the left canine eminence with the C and P2-P3 (Fig. 10). KA-A-105 is housed at the AMPG. This specimen is a partial skull preserving part of the occipital bone, the left teeth row P2-M3 and the right P2, M1-M3 (Fig. 12). PCUP.14.77 is housed at the Palaeontological Collection of the University of Patras (PCUP). This specimen is preserving almost the whole ventral side of the skull of *H. creutzburgi* (Fig. 11). KA-A-106 is housed at the AMPG. This specimen is an almost complete mandible (Fig. 13, 14, 15). Specimen KA-A-1098 is an isolated fragmented right upper canine housed at the AMPG. Several uncatalogued fragments housed at the AMPG including a big part of a lower canine with a part of the canine alveoli (Fig. 16, A), a part of the left mandibular corpus preserving the canine and p4 (Fig. 16, B), a part of the right mandibular ramus preserving a fragmented m3 (Fig. 17, B), a part of the left mandibular ramus preserving m2, m3 (Fig. 16, A) and two isolated lower first incisors (Fig. 16, C). A dataset with 33 skulls of fossil and extant Hippopotaminae from several museums was used for the reliability test (see Appendix I). Finally, we used a 3D model of *H. amphibius* from the D'Arcy Thompson Zoology Museum at the University of Dundee, created by Dr Caroline Erolin and downloaded from https://sketchfab.com/.

Figure 7. Partial skull of *H. creutzburgi* (KA-A-109) in (A) anterior and (B) posterior views. Scale = 5 cm.

Figure 8. Partial skull of *H. creutzburgi* (KA-A-109) in (A) left and (B) right lateral views. Scale = 5 cm.

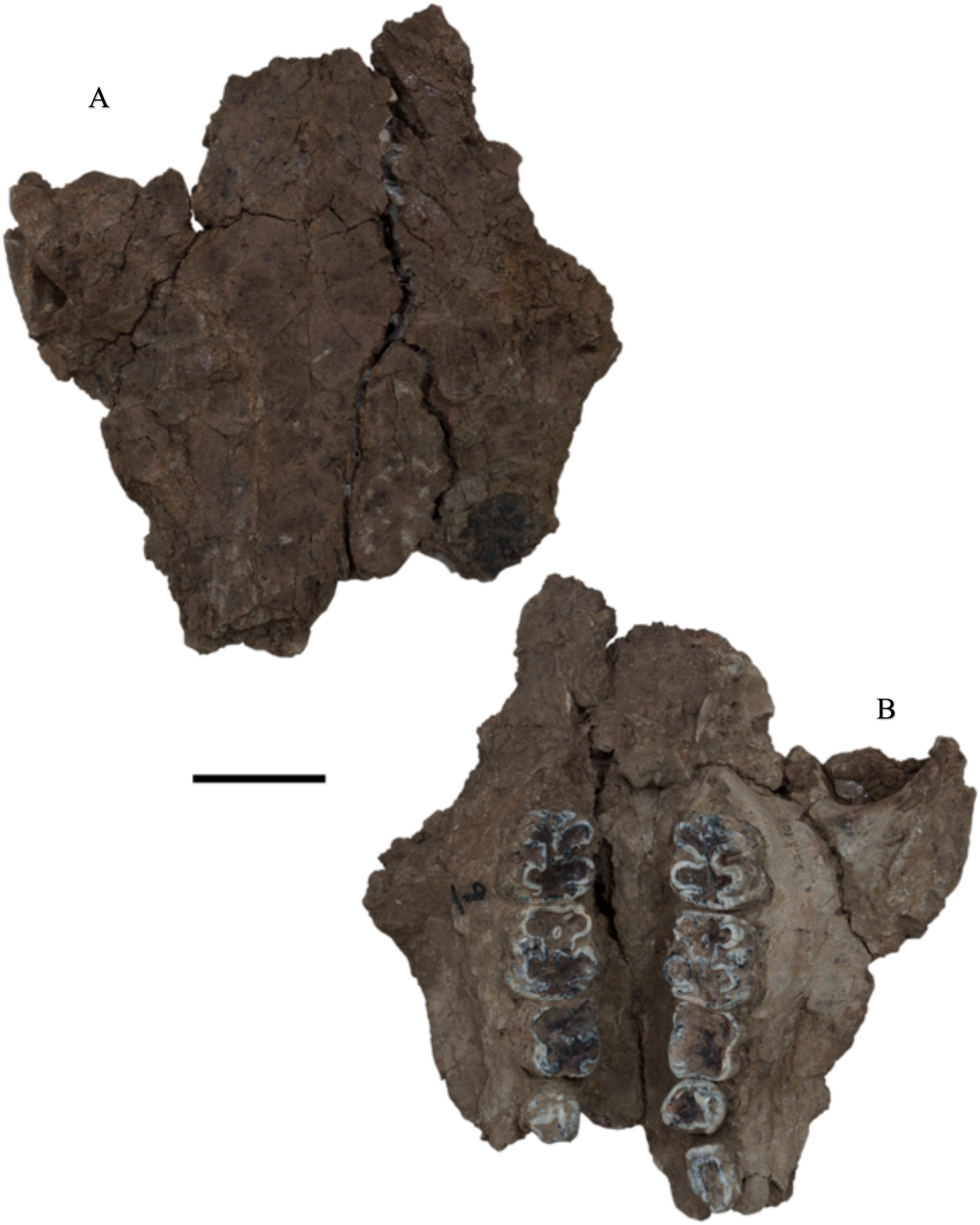

Figure 9. Partial skull of *H. creutzburgi* (KA-A-109) in (A) dorsal and (B) ventral views. Scale = 5 cm.

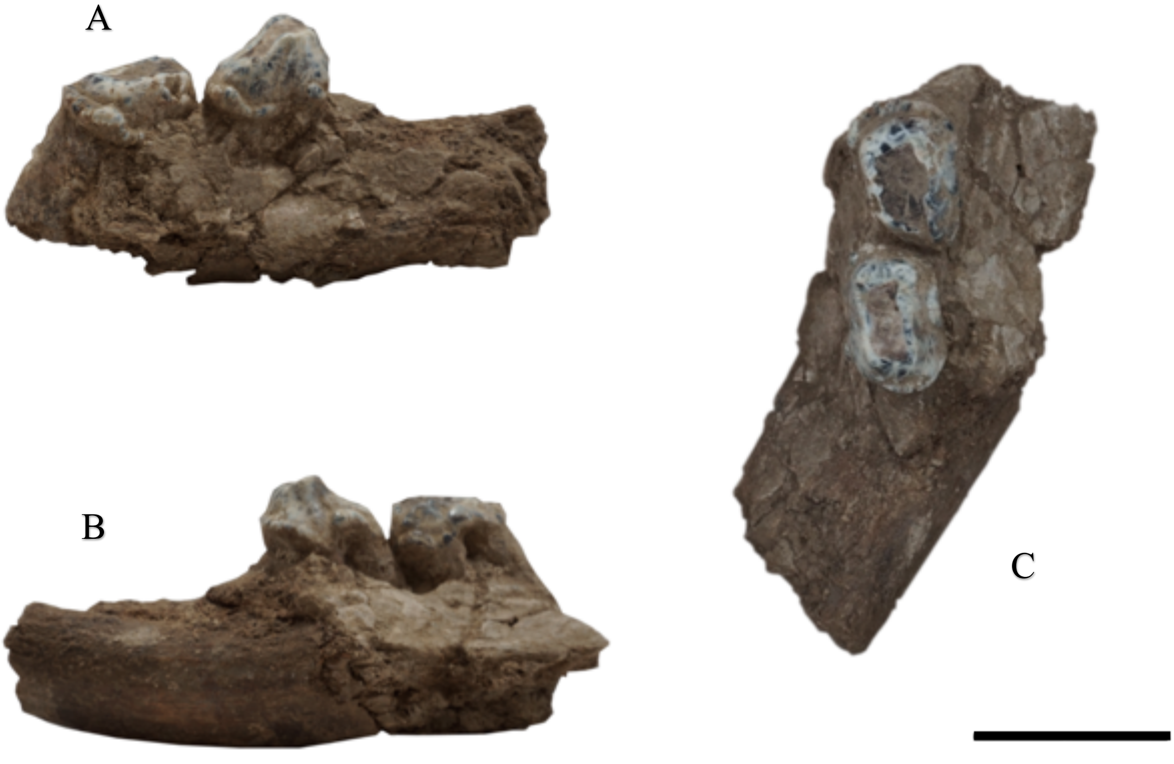

Figure 10. A broken part with C, P2 and P3 (from KA-A-109) in (A) buccal, (B) lingual and (C) occlusal views. Scale = 5 cm.

Figure 11. Partial skull of *H. creutzburgi* (PCUP.14.77) in ventral view. Scale = 10 cm.

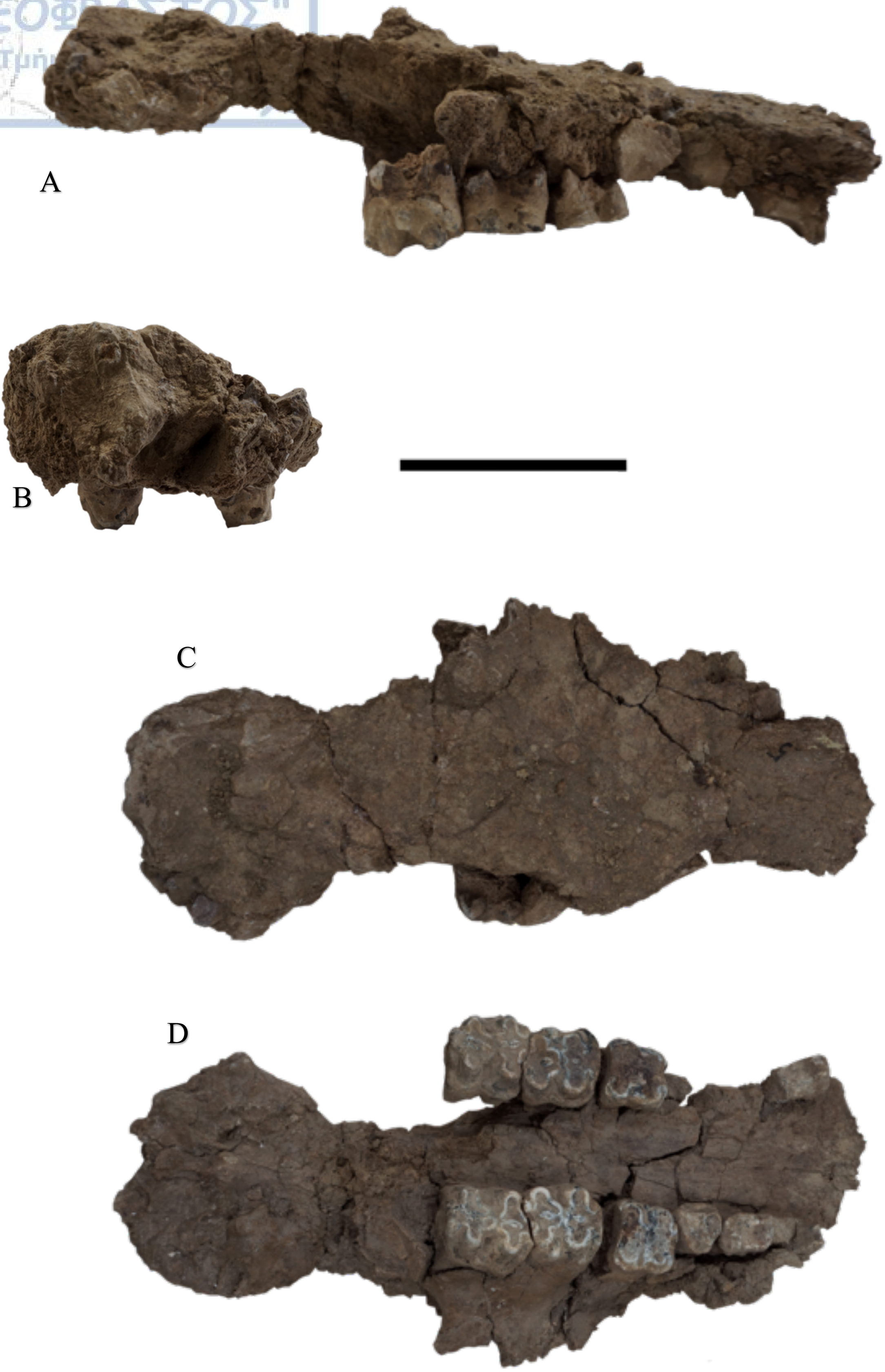

Figure 12. Partial skull of *H. creutzburgi* (KA-A-105) in (A) right lateral, (B) occipital, (C) dorsal and (D) ventral views. Scale = 10 cm.

Figure 13. Almost complete mandible of *H. creutzburgi* (KA-A-106) in (A) anterior and (B) posterior views. Scale = 5 cm.

Figure 14. Almost complete mandible of *H. creutzburgi* (KA-A-106) in (A) left lateral and (B) right lateral views. Scale = 10 cm.

Figure 15. Almost complete mandible of *H. creutzburgi* (KA-A-106) in dorsal view. Scale = 10 cm.

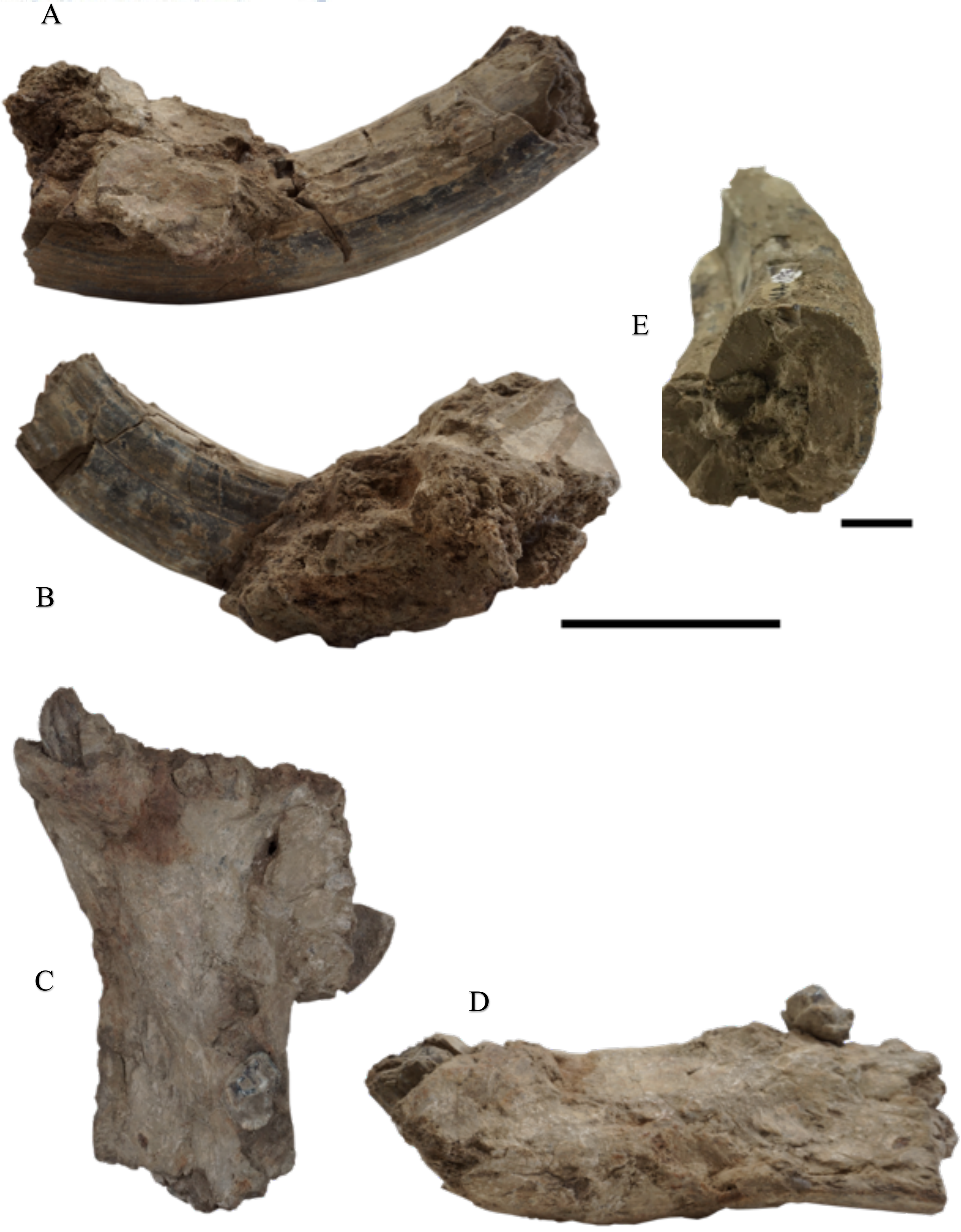

Figure 16. Part of lower canine and canine eminence in (A) buccal and (B) lingual lateral views and a left part of mandible of *H. creutzburgi* in (C) dorsal, (D) left lateral views and (E) isolated fragmented right upper canine (KA-A-1098) in facial view at its occlusal side. Scale = 10 cm and 1 cm for KA-A-1098.

Figure 17. (A) Part of the left mandibular ramus preserving m2, m3, (B) part of the right mandibular ramus preserving a fragmented m3 and (C) two isolated lower incisors. Scale = 10 cm.

2.2. Methods

Photogrammetry was used for digitizing our specimens. For the retrodeformation process we were inspired by the study of DeVries and colleagues (2022) and followed some of their instructions. A similar approach was used for retrodeforming artworks (Makris et al., 2021). For the description of the specimens, we used some characters of Hippopotaminae noted by Boisserie (2005) and Weston (1998). For the teeth description we followed the terms of Hooijer (1946, 1950) and Gregory (1951) based on Osborn (1907). For the discussion about sexual dimorphism, we based on observations by Weston (1998) on *H. amphibius*. The age stages were calculated according to Laws (1968). For the reliability check of the reconstructed model, we took two measurements. The vertical distance from the anterior part of nasal to the palatum (NF-PAL) and the horizontal length of the post canine dental battery (PCL), (see Appendix III). We compared the muzzle to the cranium length ratio of *H. creutzburgi* to *H. amphibius* 3D model from D'Arcy Thompson Zoology Museum at the University of Dundee as well as the orbit to the face length ratio (see Appendix III).

Photogrammetry was selected as a more reliable and affordable method for the current approach framework that produces fantastic results with high resolution and accuracy. However, another reason was that these specimens are very fragmented, and using CT-Scanning, would be a very time-consuming process for making the final model by merging all these fragments. The ideal placement for the specimens during the photography session would be vertically, but due to their susceptibility, we placed them horizontally for safety.

2.2.1. Equipment

The camera that was used was Sony a6000, a cropped frame mirrorless camera with a 24.3 MP sensor. We also used the 16-55mm power zoom kit lens. The Vanguard SBH-50 tripod with the Alta pro 264AT multi-action ball head tripod was used for stabilizing the camera. A turntable, normally used for making ceramics, was used for turning the specimen at different angles. The turntable was covered with a piece of newspaper for better recognition of the specimen from the software. As an experiment, sometimes we used a white styrofoam piece for the background and others not. A specialized light setup was not used, but we ensured stable lighting for the specimen with the room lights. The creation of the 3D meshes were made with a Dell Precision 7560 laptop with 32GB RAM, a NVIDIA RTX A4000-8GB graphics card and a xeonW-11955M processor. The post processing with an Apple Macbook Pro 2015 with 8GB RAM, a 256GB SSD, an Intel Iris Graphics 6100 1536 MB graphics card, and a 2.7 GHz Dual-Core Intel Core i5 processor. For the whole process we used the following software: Reality Capture v.1.2.1 (Capturing Reality, 2016) as it is considered the fastest and easiest photogrammetry software for beginners (Kingsland, 2020), with an educational licence (116295), the free and open-source Meshlab v. 2022.02 (ISTI - CNR, 2005) for scaling and decimating the 3D meshes, Meshmixer v. 3.5.474 (Autodesk, 2017) for repairing the meshes and the free and open-source Blender. v. 3.4.0 (Blender Foundation, 2002) for the retrodeformation process.

2.2.2. Photography

Specimen KA-A-109

One set of photographs at different heights was taken for each side. For the dorsal side, we took 385 photos, and for the ventral 258, 643 photos in total. The six levels that we set the tripod were 56, 60, 66, 73, 80, and 87 cm from the floor to the camera. From level 73 cm to 87 cm, we set an angle of 45° to the camera for better capturing. For the dorsal side, we took a photograph every 4º and for the ventral every 6º. The higher level was omitted from the set of the downside. The camera lens was 50 cm away from the specimen, the exposure time was set at 0.8′′, the focal length was at 20 mm, the ISO speed was 100, the F-number was f/13, and the white balance was set to auto. A 2′′ timer was also set to ensure camera stability. In total, we spend 1 hour and 40 minutes for the photography process, 1 hour for the dorsal side, and 40 minutes for the ventral.

Specimen KA-A-109 (broken part)

One set of photographs at different heights was taken for each side. For the dorsal side, we took 255 photos, and for the ventral 283, 538 photos in total. The three levels that we set the tripod were 95, 100, and 105 cm from the floor to the camera. At levels 100 cm and 105 cm, we set an angle of 45º to the camera for better capturing. For both sides, we took a photograph every 4º. The camera lens was 40 cm away from the specimen, the exposure time was set at 0.8′′, the focal length was at 16 mm, the ISO speed was at 100, the F-number was f/13, and the white balance was set to auto. A 2′′ timer was also set to ensure camera stability. In total, we spend 1 hour and 10 minutes on the photography process, 30 minutes for the dorsal side, and 40 minutes for the ventral.

Specimen KA-A-105

One set of photographs at different heights was taken for the ventral side. The dorsal side was deformed, and as a result, we decided to take no photos. We took 362 photos, in total. The two levels that we set the tripod were 95 and 105 cm from the floor to the camera. At level of 105 cm, we set an angle of 45º to the camera for better capturing. We took a photograph every 3º. The camera lens was 55 cm away from the specimen at the level of 95 cm, and then we placed the camera 30 cm away for a second set at the same distance and for the level 105 cm. The exposure time was set at 1/1.6′′, the focal length was at 16 mm, the ISO speed was 125, the F-number was f/13, and the white balance was set to auto. A 2′′ timer was also set to ensure camera stability. We spend 40 minutes on the photography process.

Specimen PCUP.14.77

One set of photographs at different heights was taken for the ventral side. The dorsal side of this specimen is not available because it is placed in a plaster cast. We took 337 photos in total. We did not measure the different levels we set for that sample, and due to the lack of a tripod, we made an improvised one with a chair, some books, and boxes. Some photos were captured with a handheld camera, too. Instead of the turntable, we used a hard cardboard. The exposure time was set at 1/40′′, the focal length was at 16 mm, the ISO speed was 320, the F-number was f/7.1, and the white balance was set to auto. A 2″ timer was also set to ensure camera stability. In total, we spend 40 minutes on the photography process.

Specimen KA-A-106

One set of photographs at different heights was taken for each side. For the dorsal side, we took 337 photos, and for the ventral 289, 626 photos in total. The three levels that we set the tripod were 95, 100, and 105 cm from the floor to the camera. From level 100 cm to 105 cm, we set an angle of 45º for the camera for better capturing. For the dorsal side, we took a photograph every 3º and for the ventral every 4º. The camera lens was 40 cm away from the specimen, the exposure time was set at 0.8″, the focal length was at 16 mm, the ISO speed was 125, the F-number was f/13, and the white balance was set to auto. A 2″ timer was also set to ensure camera stability. In total, we spend 1 hour and 30 minutes on the photography process, 50 minutes for the dorsal side, and 40 minutes for the ventral.

Figure 18. During the photography session.

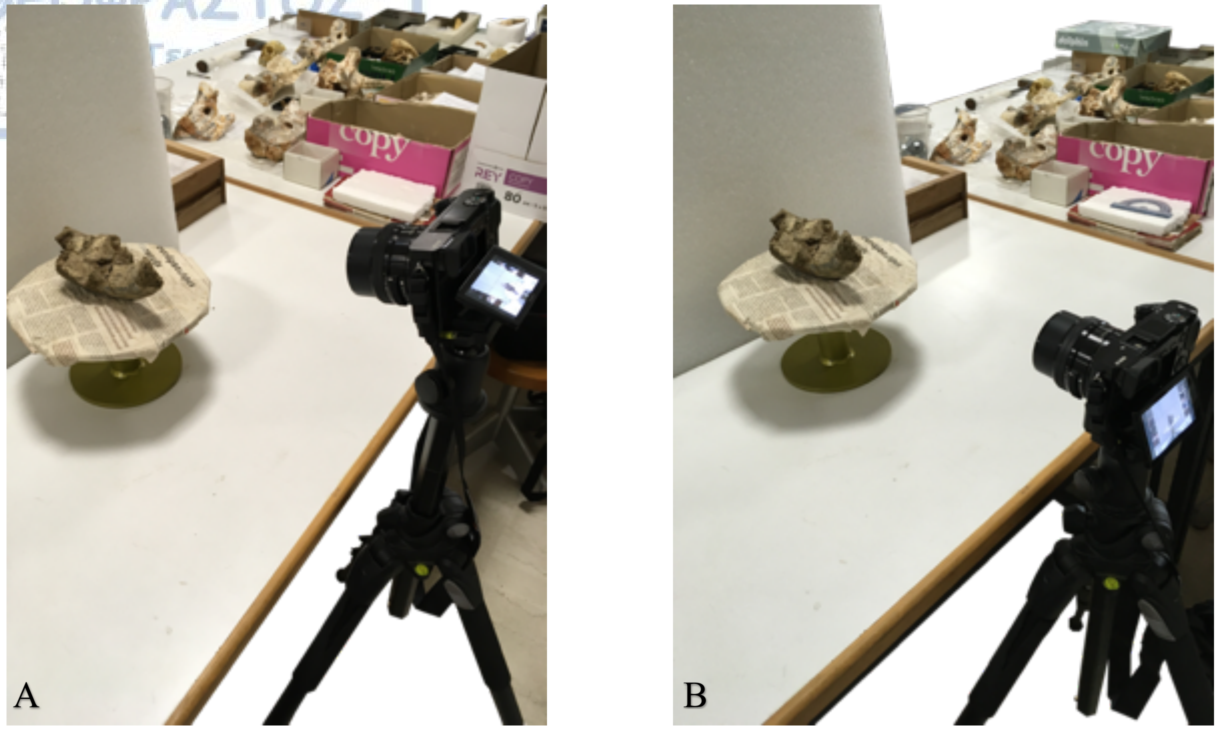

Figure 19. The two different positions of the camera: (A) the 45º and (B) the horizontal.

2.2.3. Photogrammetry

We shot our photos in RAW, but this file format is massive, so we had to transform them to JPEG files before importing them in the software, but without any compression to avoid decreasing the quality of the photos. For creating every 3D model in Reality Capture, we made a point cloud for the dorsal and the ventral side, exported masks and then combined them into one mesh.

After importing the photos of the dorsal side, we aligned the images by hitting the Align Photos button in the Process section located in the ALIGNMENT tab. During the image alignment the software calculates camera positions, orientations and internal camera states for every imported image based on several common points. The result was a sparse point cloud. Then we selected Cut by Box in the TOOLS tab and we cut the turntable and part of the specimen by reducing the size of the rectangle surrounding the mesh. After that, in the TOOLS tab in the Export section, we selected Depth and Mask to export the masks of the mesh to the same folder with the photos.

The next step was to create the masks of the ventral side of the model with the same way. For creating the whole specimen, we imported all the photos and the masks of the two sides in a new project and continued with the aligning process. Then we generated the final 3D model by hitting the Normal detail button in the MESH MODEL tab, and we got a triangulated mesh. To make the texture of the mesh we selected the Texture button in the same section, and we got the complete mesh of our specimen (see Appendix II). We exported the mesh as a Stanford PLY file to include the colour and the texture of the 3D meshes.

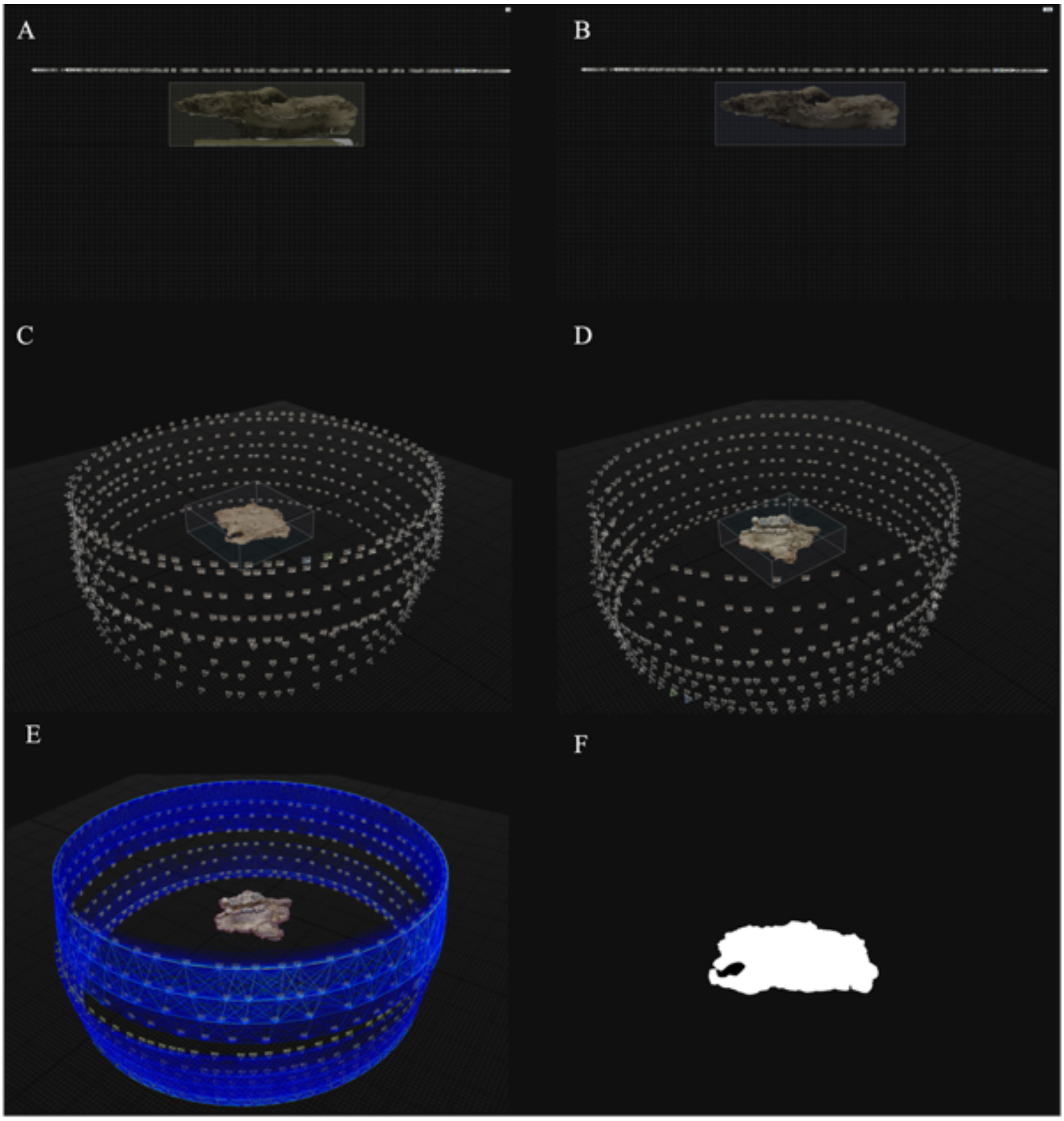

Figure 20. Different snapshots inside Reality Capture. (A) The mesh of the dorsal side of the specimen before masking and (B) after masking, (C) the dorsal and (D) the ventral side of the final mesh, (E) inspect quality mode highlighting every correctly aligned camera with blue colour, and (F) an exported mask.

2.2.4. Scaling and decimating

Photogrammetry does not reconstruct the specimens on a scale, so scaling is necessary after the creation of the model. The ratio between a measurement on the actual specimen and the corresponding measurement on the digital model is called scale factor. In Meshlab the process is simple, selecting: Filters→Normals, Curvatures, and Orientation→Transform: Scale and Normalize, typing the scale factor in the box of X-Axis, and applying it, the scaled model is ready. For easier and faster editing of the 3D meshes, we had to decimate them to fewer faces. For better results, a progressive decimation process is suggested. In Meshlab, the process is: Filters → Remeshing, Simplification and Reconstruction → Simplification: Quadric Edge Collapse Decimation and typing the preferable number of faces in the box of "Target number of faces" and applying. We targeted 500.000 faces which is the lower quality without losing significant details from our specimens.

Figure 21. 3D models of various *H. creutzburgi* specimens. (A) KA-A-109, (B) KA-A-105, (C) broken part of KA-A-109, (D) PCUP.14.77 and (E) KA-A-106.

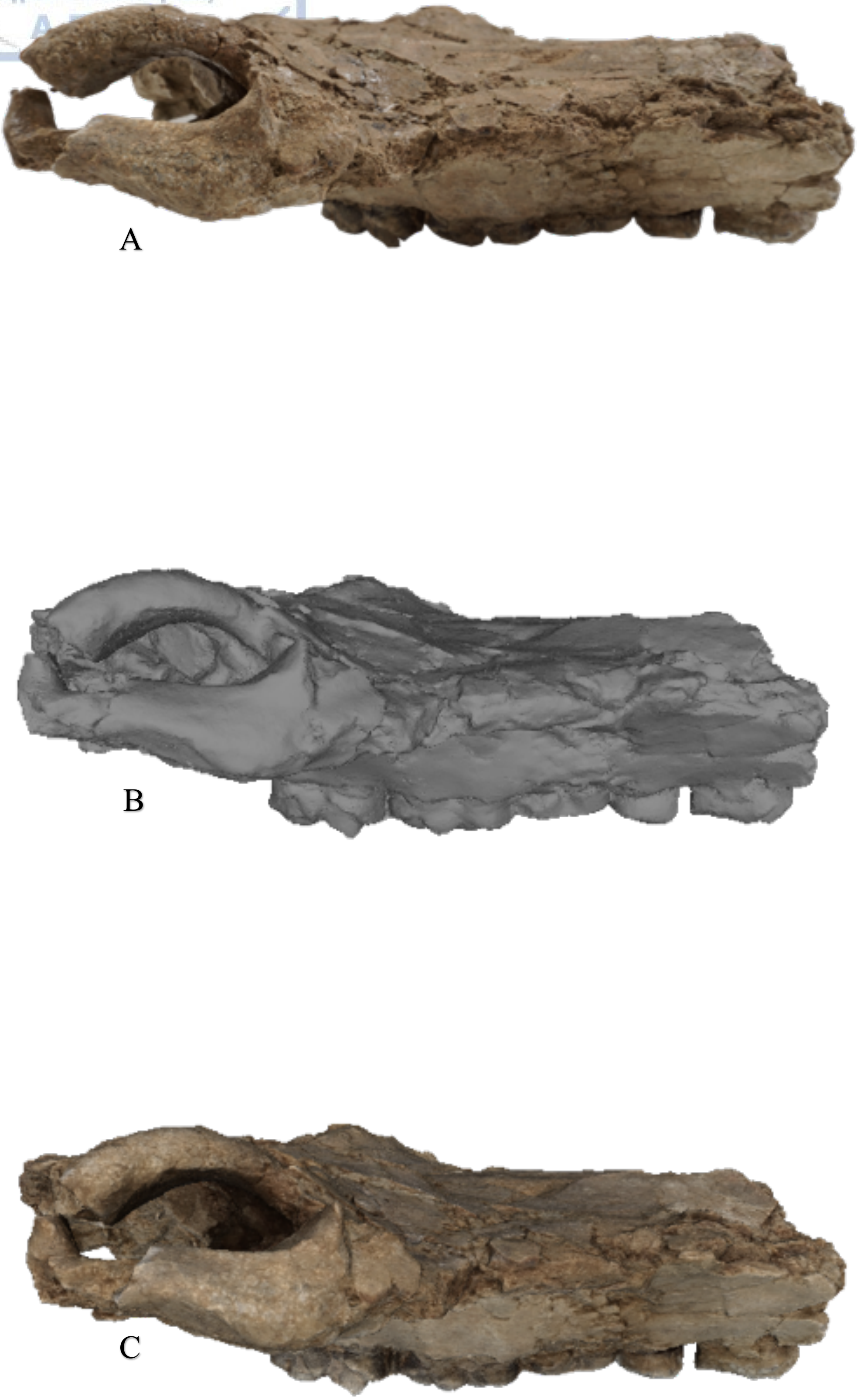

Figure 22. (A) Photo, (B) mesh without and (C) with the texture of the skull (KA-A-109) of *H. creutzburgi*.

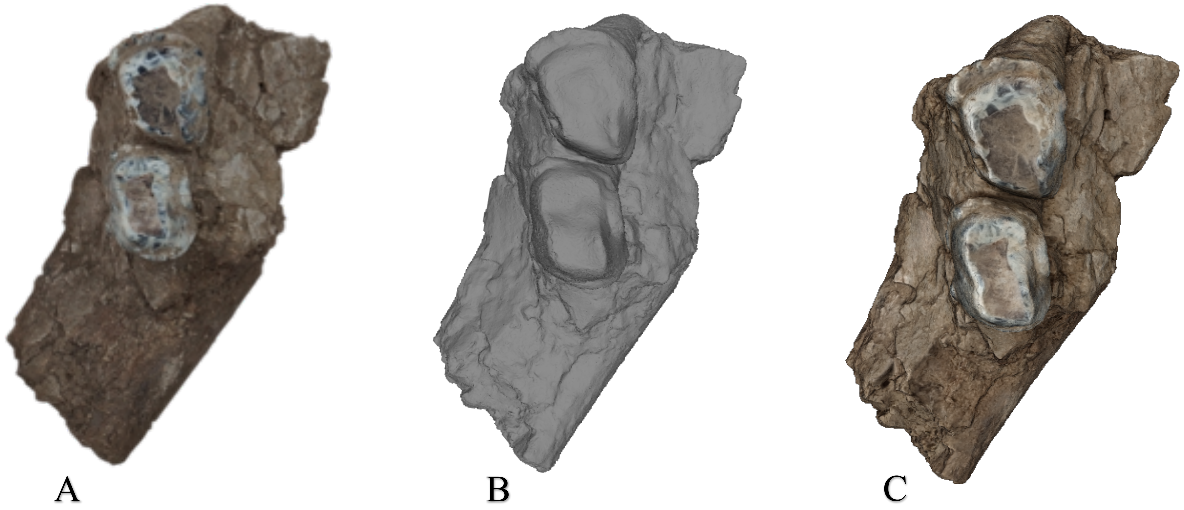

Figure 23. (A) Photo, (B) mesh without and (C) with the texture of the broken part of the skull (KA-A-109) of *H. creutzburgi*.

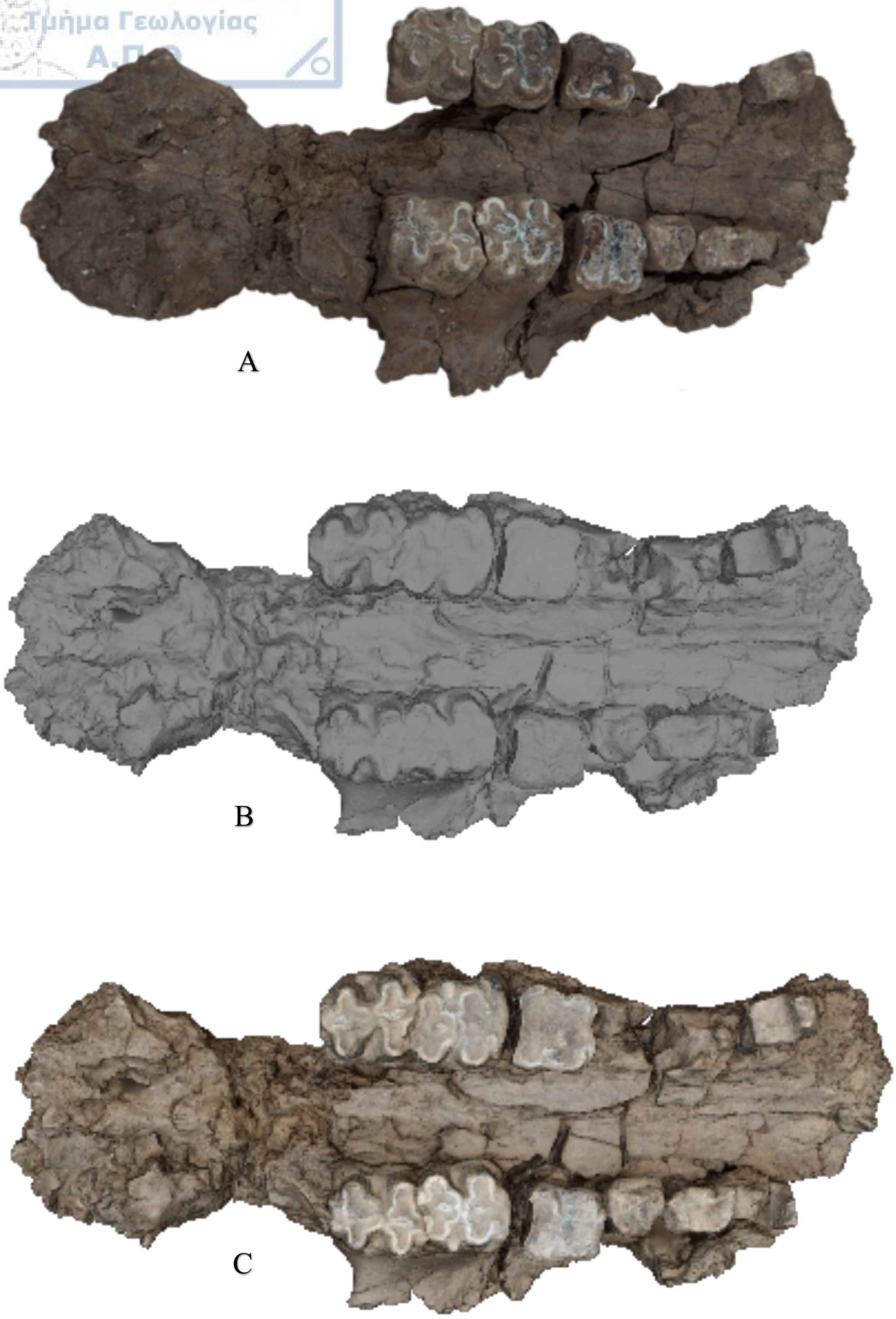

Figure 24. (A) Photo, (B) mesh without and (C) with the texture of the skull (KA-A-105) of *H. creutzburgi*.

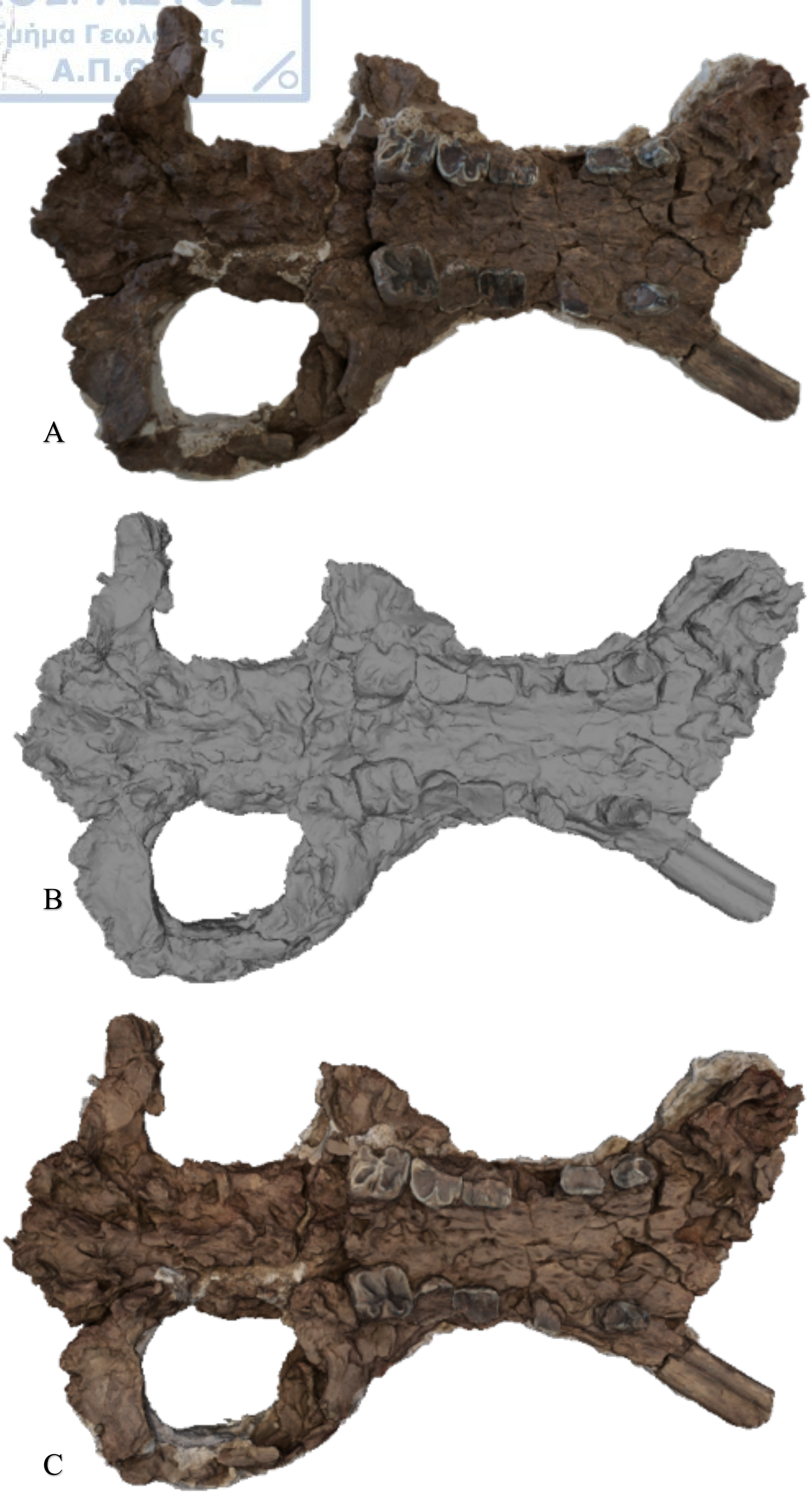

Figure 25. (A) Photo, (B) mesh without and (C) with the texture of the skull (PCUP.14.77) of *H. creutzburgi*.

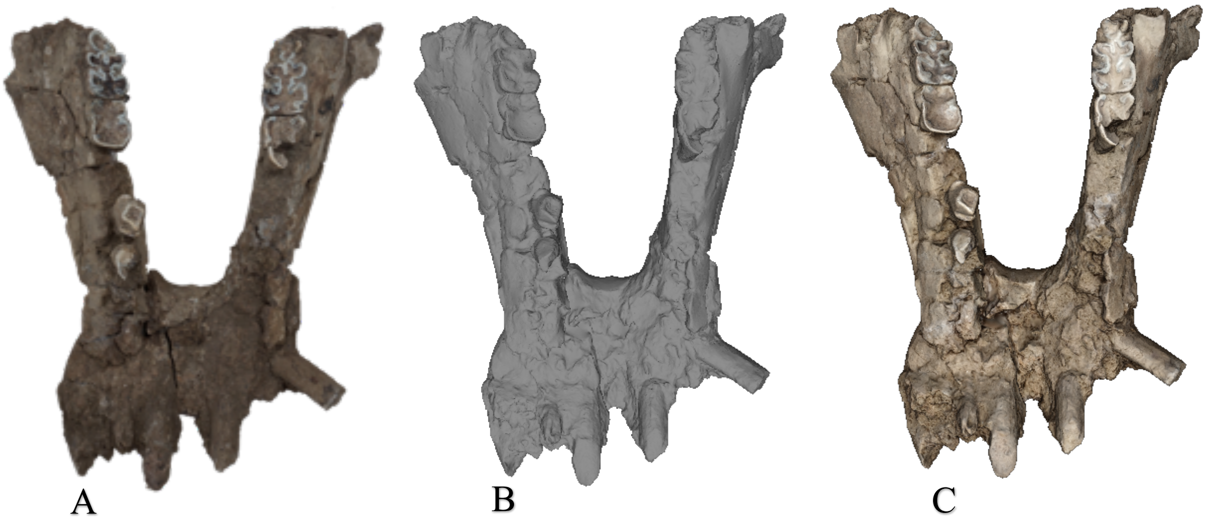

Figure 26. (A) Photo, (B) mesh without and (C) with the texture of the mandible (KA-A-106) of *H. creutzburgi.*

2.2.5. Repairing

Two of the specimens, KA-A-105 and PCUP.14.77, had only the ventral side digitized. To close the holes of the dorsal sides we used the Meshmixer software. Selecting Analysis → Inspector → Auto Repair all. Inspector mode detects all the problems of the model and then suggests how they can be solved.

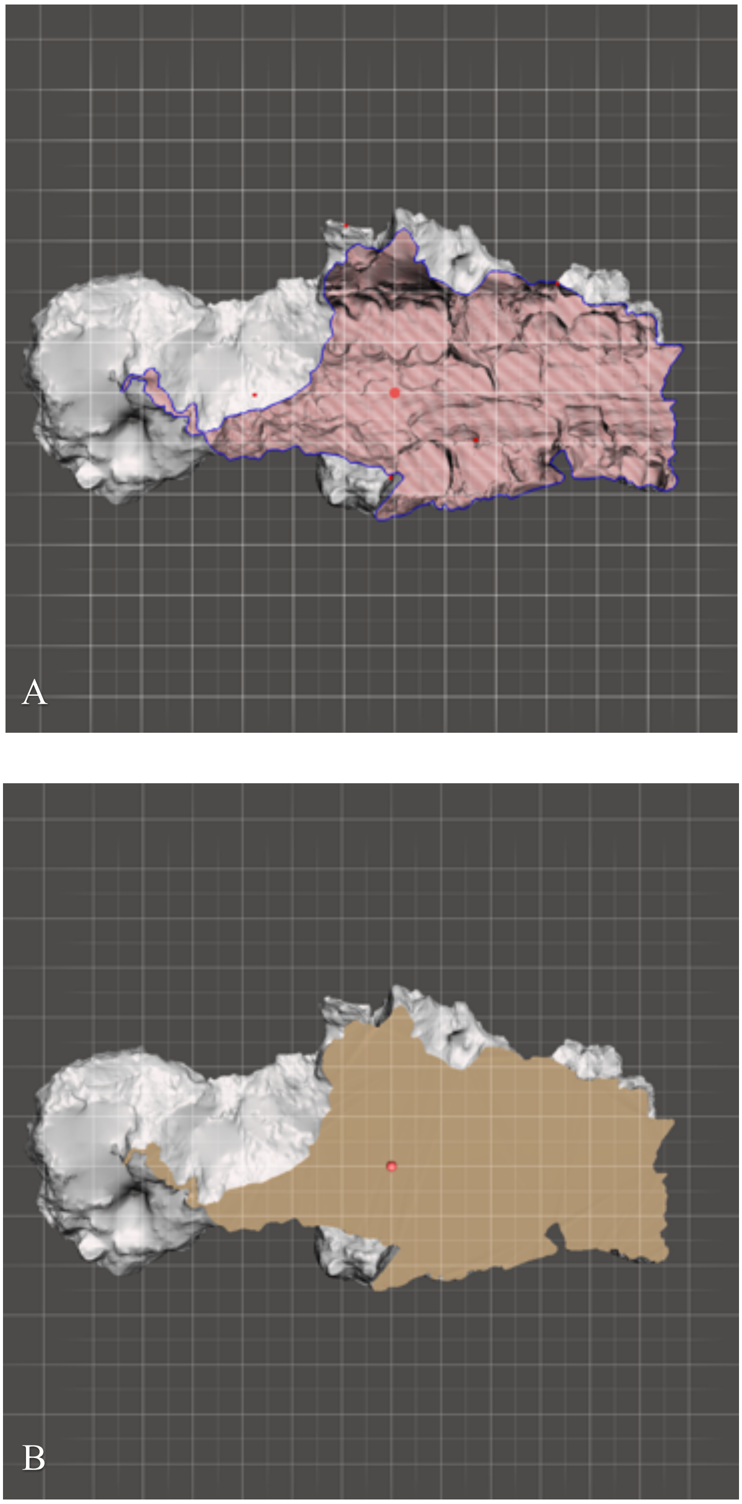

Figure 27. (A) Before and (B) after repairing the specimen KA-A-105 in Meshmixer.

2.2.6. Retrodeformation

Bringing the flattened skull back to its primary state was our first concern. At first, to retrodeform it, we experimented with Blender's armature. We constructed a spider-like structure with bones and tried to straighten up the palatum. A bone is created by adding an armature Shift + A → Armature. Then in Edit Mode, selecting one of the two ball-shaped joints of the bone and pressing E, another bone is extruded. Selecting more joints and pressing E equal number of bones are extruded simultaneously. For the skeleton that was used, we created the middle bones and then extruded the others. To parent the bones with the mesh, we selected the mesh, and then with Shift + left click the armature. Pressing cmd/ctrl + P → With Automatic Weights or With Empty Groups to paint the weight manually.

We followed the instructions of DeVries and colleagues (2022) and chose a specific colour gradient: indigo (0.000), blue (0.001), green (0.500), red (0.999), and grey (1.000). Weight painting creates a weighted link between a group of vertices in the mesh and an armature segment. To enter the Weight Painting mode, we selected the armature, then with Shift + left click the mesh and changed to Weight Painting mode from the menu. In this mode, the weight, the radius, and the strength of the brush are fully customisable. We tried the automatic weight, and since our bones were placed correctly, it worked. Although we made the palate straight, the skull continued to be flat. Therefore, we decided to apply a more traditional approach that would have been destructive for the actual specimen, but in the digital world, the possibilities are more.

We relied on the admission that maxillary bones and masticatory surfaces are flat, and the cranial bones are preserved though flattened. Firstly, we cut with a vertical plane the orbit including the zygomatic crest and part of the frontal bone. Then, we cut the skull with a horizontal plane at the level of the upper border of the maxillary bone with the flattened dorsal side, creating two pieces. Finally, we cut the upper part in the middle of the nasal bone with a vertical plane, and in the same way, we cut the lower part in the mid-palatal suture creating five parts in total. The eye, the left dorsal, the right dorsal, the left ventral, and the right ventral.

The plane was 0.0006 m. A plane is created by pressing Shift + A → Mesh → Plane. Pressing the S key and moving the cursor, you can scale it until it is big enough for your specimen. In the context menu in the Modifier Properties, we changed its thickness by adding the Solidify modifier to 0.0006 m. The cuts were done by selecting the plane and then the object with Shift + left click. By pressing Slice in the Bool tool menu, the section is created. To divide the object into two sliced parts, we selected the original object, pressed Tab to enter the Edit Mode, pressed P, and then selected By Loose Parts.

The left ventral part was rotated upwards along the Y-axis with the Rotation tool until the palatum was straight. The process was repeated for the right ventral part rotating the former 28.56º and the latter 23.03º. In the next step, we moved the dorsal parts upwards by grabbing them from their inside lateral part until their less deformed contact was connected with the corresponding ventral parts. The nasal bone was restored by moving forward the right dorsal part. To fix the eye, 3 bones were placed. We parent the bones with the model by pressing cmd + P → With Automatic Weights. The part of the zygomatic bone was moved downwards until it was like *H. antiquus*, then the supraorbital ridge of the frontal bone upwards until the orbit was round.

For the mandible, we took specimen MPUR/ V2032 (Museo di Paleontologie, Università di Roma), as a standard. We relied on the admissions that masticatory surfaces are flat, the shape of the area created between the two corpora is symmetrical, and that lower teeth must be in contact with the upper teeth. We placed 23 bones, the centrals, the parallels (to the ground), and the verticals (to the ground). The bone numbering is increasing from the anterior to the posterior of the mandible. The left corpus and ramus were almost undistorted. They were just straightened by rotating the 4th vertical bone along the Y-axis by 12.38º. The right corpus and ramus were dorsoventrally distorted. We moved the 5th parallel bone along the Y-axis by 33.01º, the 5th vertical bone along the Y-axis by -72.18º and along the X-Axis by 20.86º, the 4th parallel bone along the Y-axis by 3.12º, the 4th vertical bone along the Y-axis by -23.94º, the 3rd vertical bone along the Y- axis by -7.97º, the 1st and 2nd parallel bones along the Y-axis by 2.43º, and the 1st and 2nd central bones along the Z-axis by -8.23º.

Figure 28. (A) Mesh of *H. creutzburgi* skull before and (B) after the retrodeformation in right lateral view.

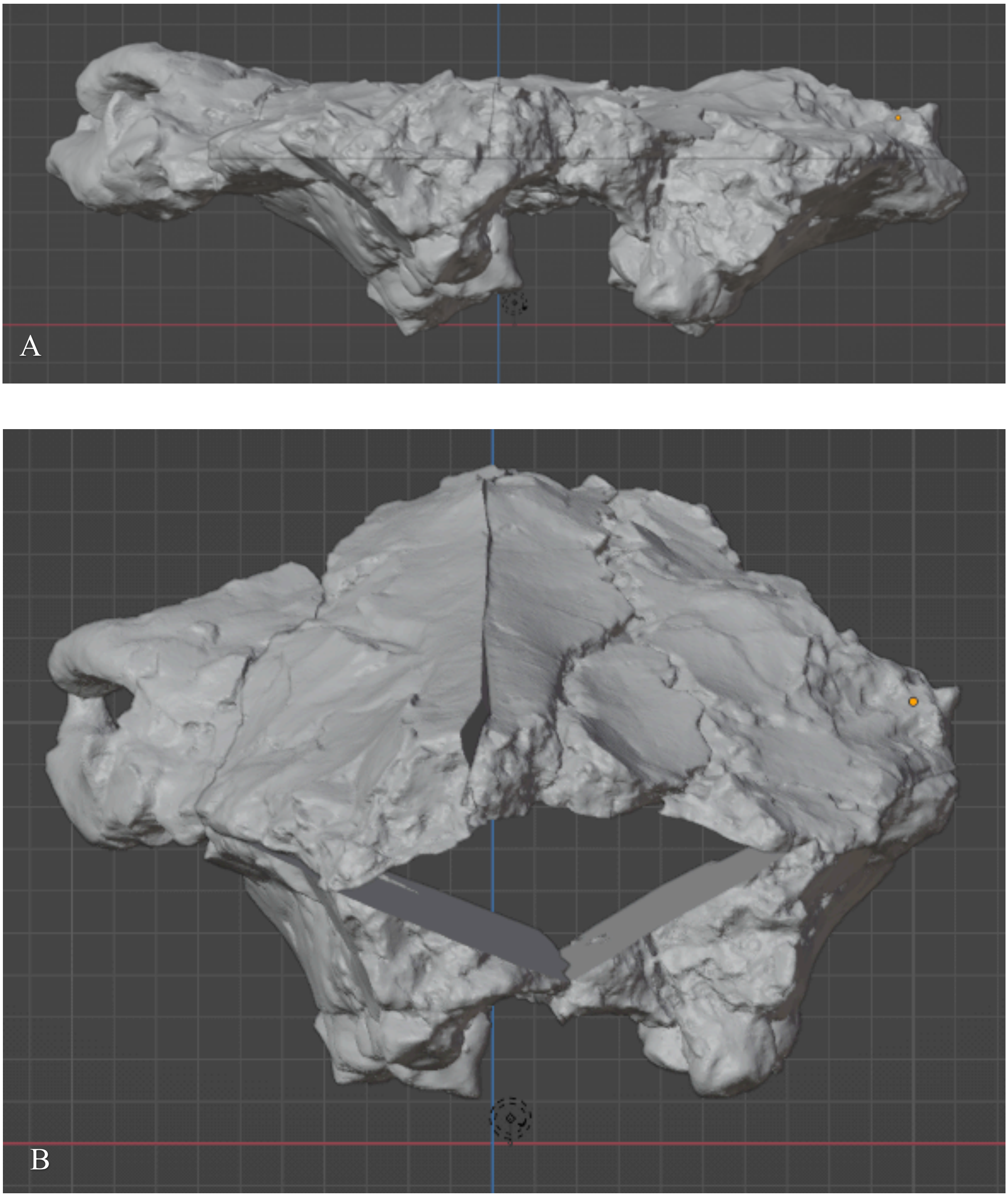

Figure 29. (A) Mesh of *H. creutzburgi* skull before and (B) after the retrodeformation in anterior view.

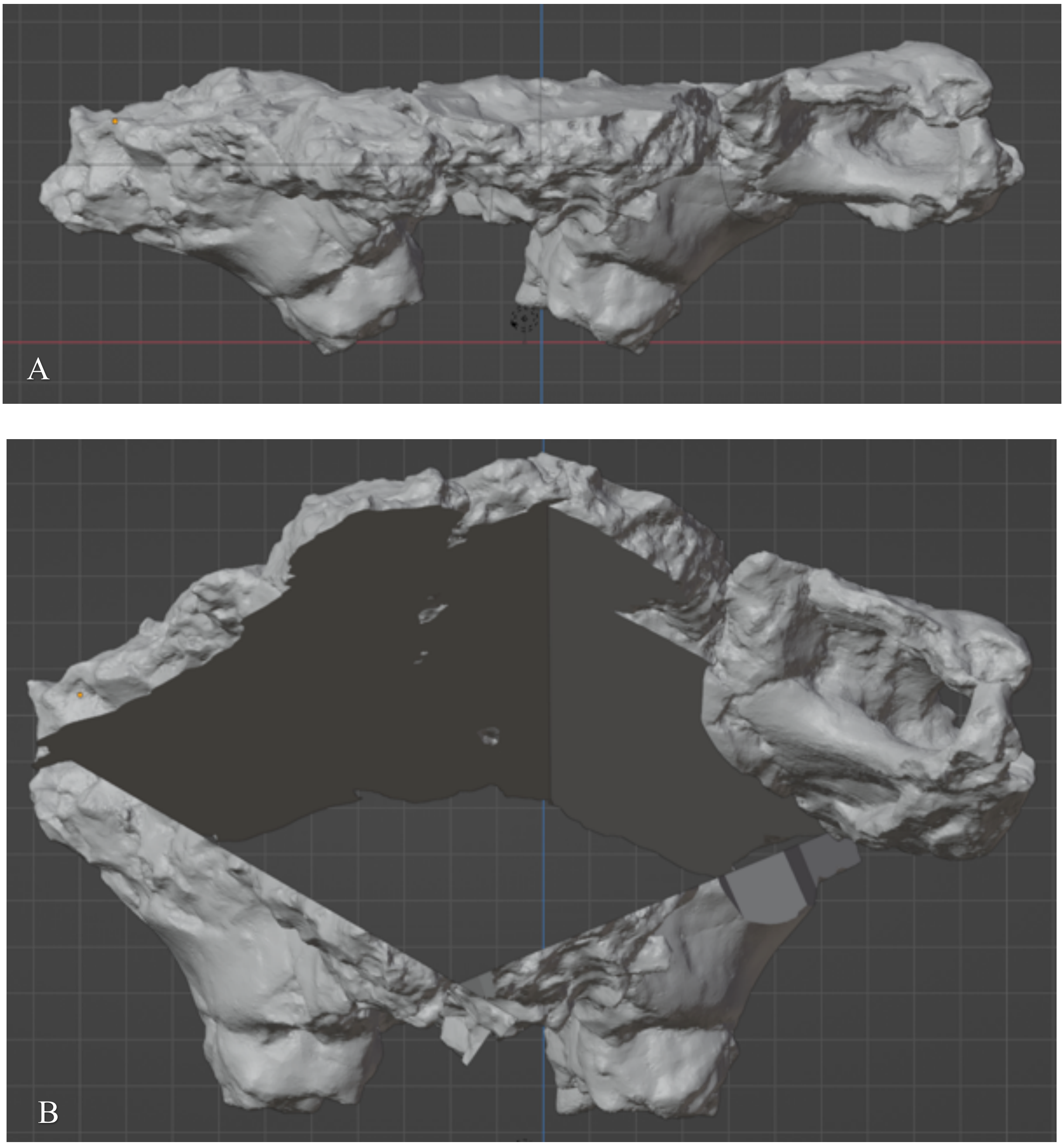

Figure 30. (A) Mesh of *H. creutzburgi* skull before and (B) after the retrodeformation in posterior view.

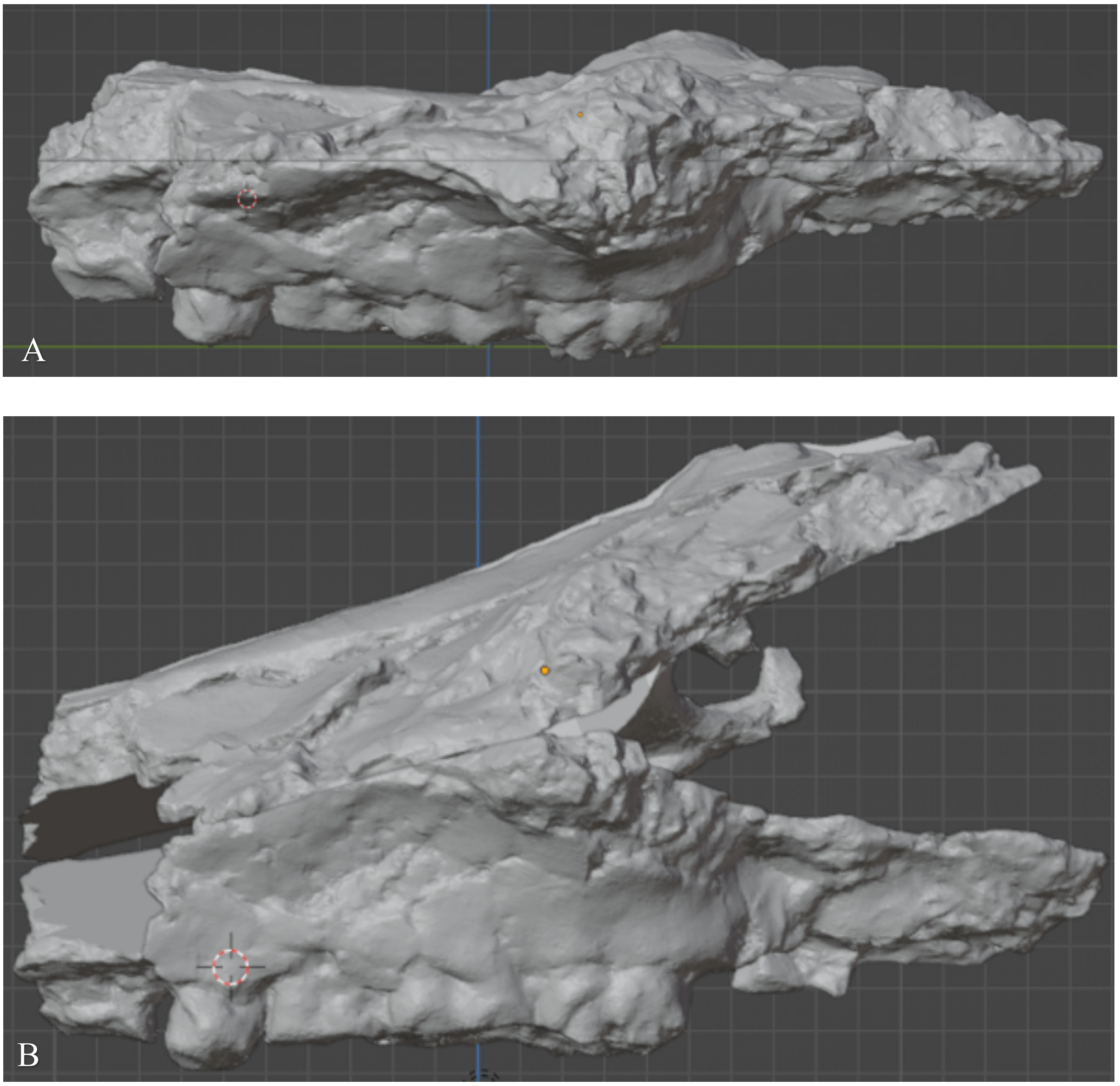

Figure 31. (A) Mesh of *H. creutzburgi* skull before and (B) after the retrodeformation in left lateral view.

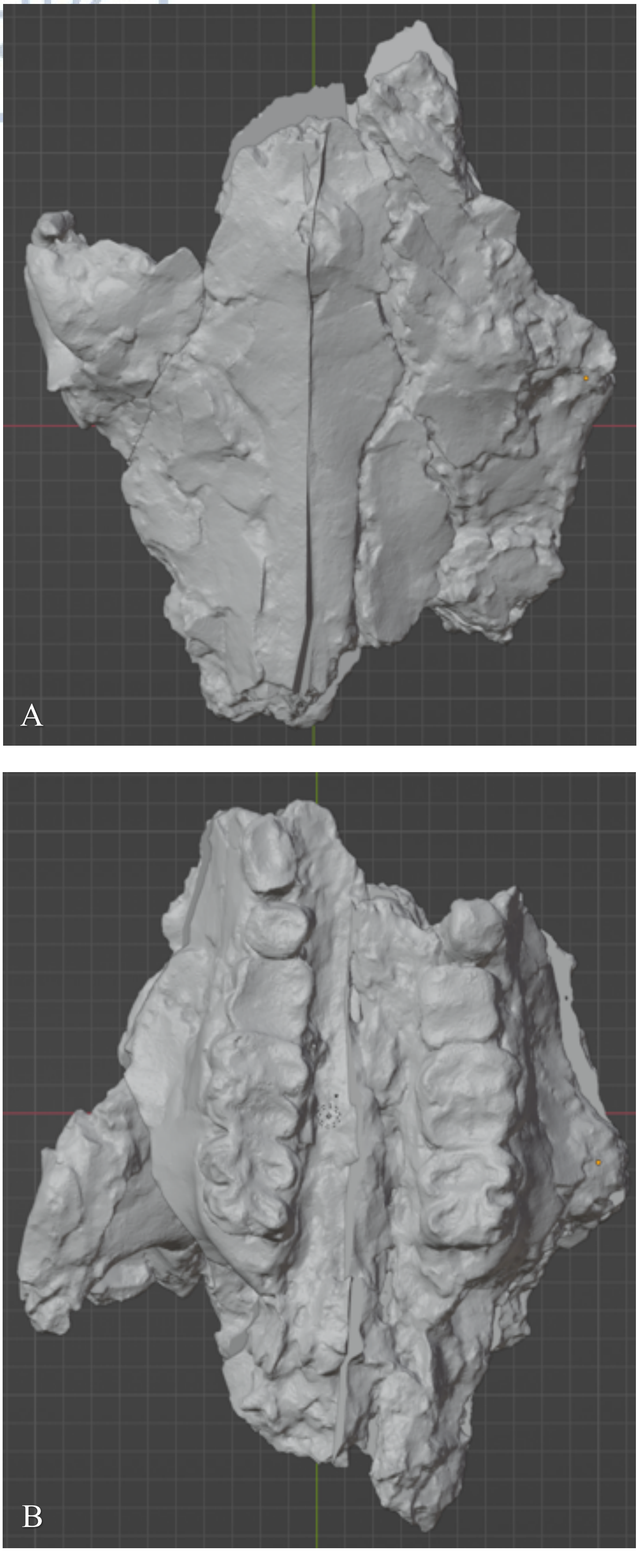

Figure 32. (A) Mesh of *H. creutzburgi* skull in (A) dorsal and (B) ventral views.

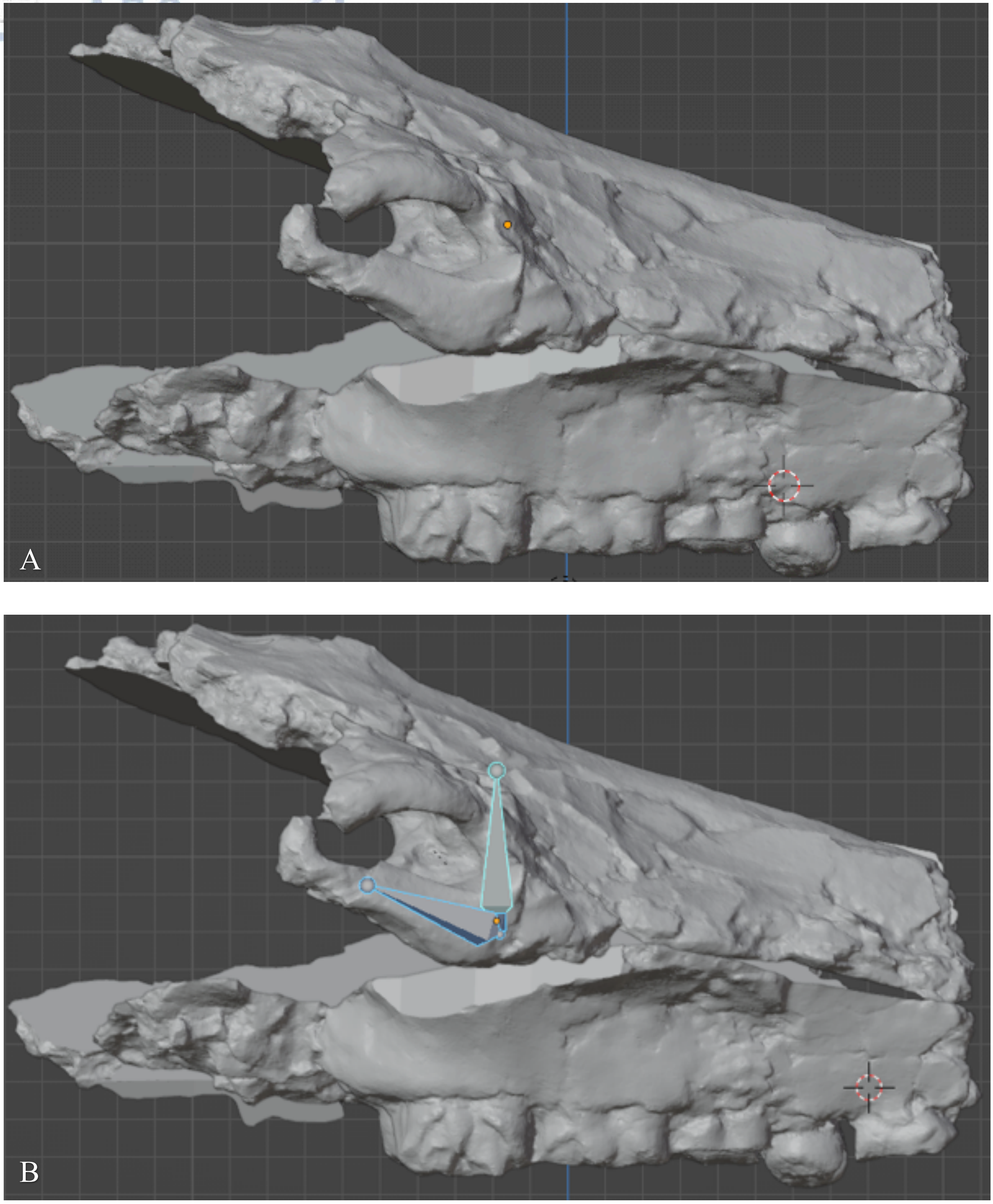

Figure 33. (A) Mesh of *H. creutzburgi* skull without and (B) with the armature on the eye before the retrodeformation in right lateral view.

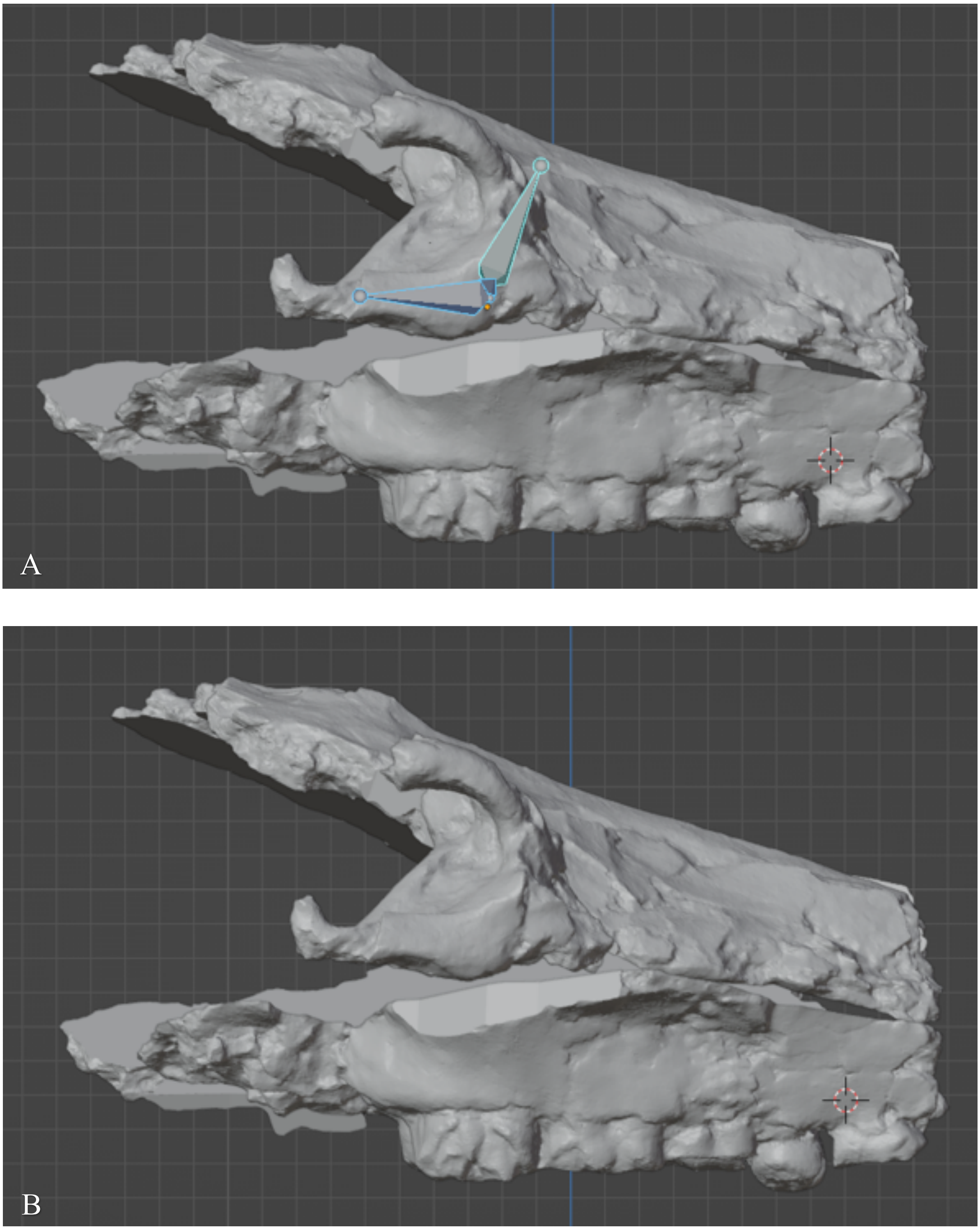

Figure 34. (A) Mesh of the skull of *H. creutzburgi* with the armature on the eye before and (B) after the retrodeformation without the armature in right lateral view.

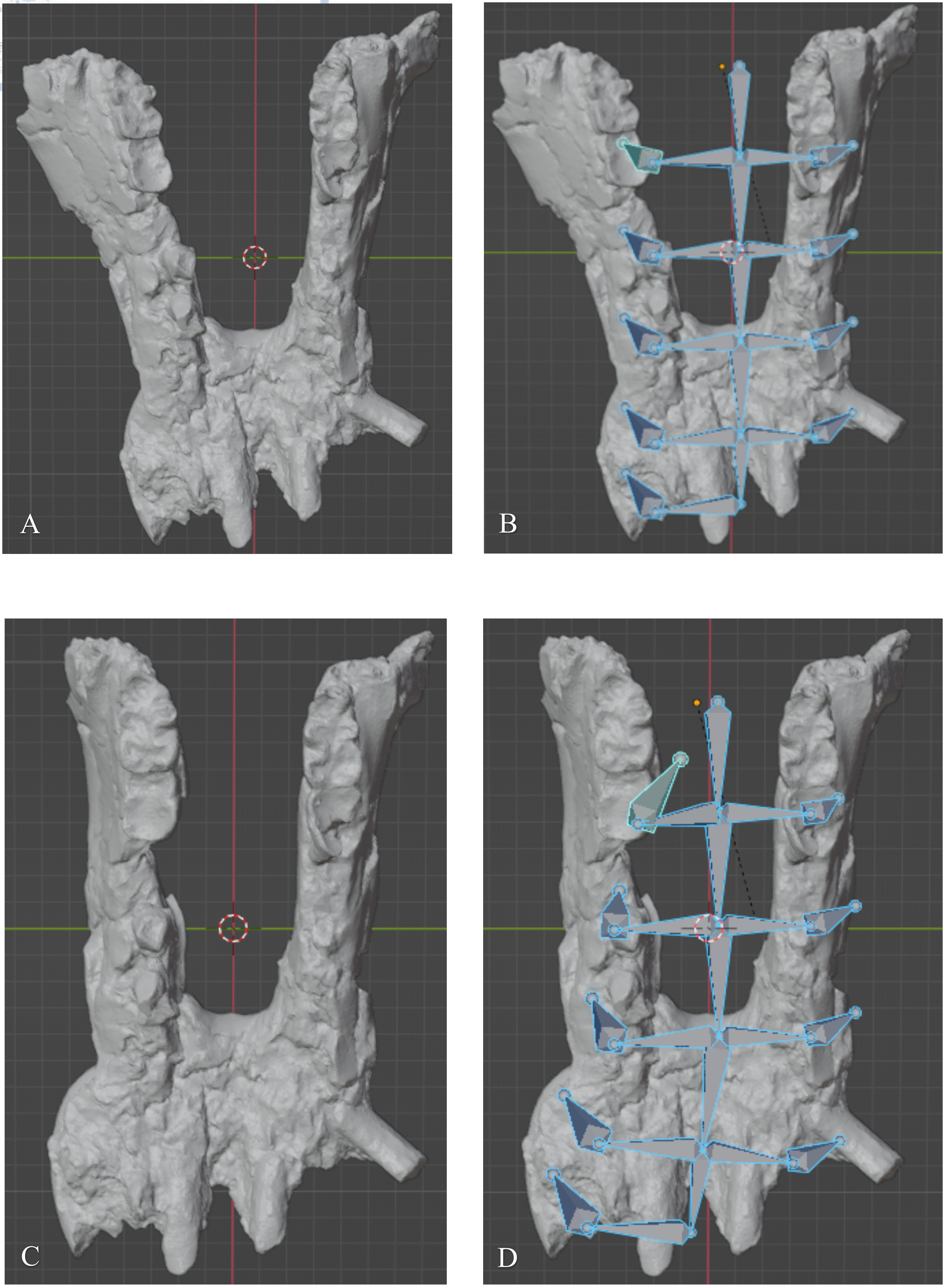

Figure 35. (A) Mesh of the mandible of *H. creutzburgi* without the armature before and (C) after the retrodeformation, (B) with the armature before and (D) after the retrodeformation.

2.2.7. Reconstruction

For the final model, we combined parts of four meshes. The partial skull (KA-A-109), the broken part with the canine eminence, and C, P2, P3, as well as the mandible (KA-A-106), were kept whole. From the second cranium (KA-A-105) we kept the lower part of the occipital bone with the foramen magnum. Our first move was to attach the broken part of the skull (KA-A-109) to its original position, which was on the left side. We duplicated this part and then mirrored it by Right click → Mirror → X Global. On the right side, P3 is preserved, though its position may be distorted compared to the left one. Still, we did not delete this right P3 from the skull. We attached the duplicated and mirrored part of the left side after P3 was removed from it.

The part of the occipital was cut at the transverse palatine suture and attached at the same place after removing the preserved part on the specimen KA-A-109. Afterward, we duplicated the part of the eye and placed it in reference to the part of the zygomatic bone preserved on the left side of the skull. To unite all the parts into one mesh we used the Boolean modifier in the Union Mode with the Exact Solver. Selecting a part every time, and then in the Object section inside the modifier picking the part we wanted to unite with, we ended up with one mesh. The mandible was positioned concerning the upper molars. The polygons of the whole model were transformed from triangles to quads before the sculpting process. We selected Filters → Polygonal and Quad Mesh → Tri to Quad by 4-8 Subdivision in Meshlab. Finally, we added some parts from a 3D model of *H. amphibius* that we modified to fit to the skull of *H. creutzburgi*.

2.2.8. Sculpting

For a more realistic and presentable result, we decided to use some of the sculpting tools in Blender to shape the parts of the *H. amphibius* to fit as well as possible into our reconstructed model. We mainly used the Smooth, the Grab and the Pinch tools. Of course, this model is a more subjective and artistic version of the cranium of *H. creutzburgi*.

2.3. Reliability check of the reconstructed model

We compared the skull of *H. creutzburgi* to other Hippopotaminae to check the fidelity of the reconstructed model we made regarding the height of the skull. We measured the length of the post-canine dental battery and the height from the palatinum to the middle of the posterior end of the nasal bone. Finally, we made two scatter plots, one with all the samples and another with only the adult individuals compared to *H. creutzburgi*. For the whole length of the skull, we compared our model with the specimen PCUP.14.77.

3. Results

3.1. Description of the specimens used for the reconstruction

Specimen KA-A-109 is a partial skull of an adult *H. creutzburgi* overall medium preserved, although is dorsally flattened along the dorsoventral axis, and its ventral side is bent along the anteroposterior axis. It has a brown-green colour with grey-blue shades. It is relatively heavy and brittle. The anterior side of the skull is a little twisted from the left to the right side, which can be seen from the nasal bone. The dorsoventral deformation was performed during the deposition because of the weight of sediment accumulation and before the fossilization process due to the lack of sediment in the interior of the skull.

From the dorsal view, a crack that splits the left maxilla bone from the nasal bone and a bigger one that splits the rest side of the skull in half, are well recognisable. These cracks were made post-depositionally. The occipital, the parietal, the left supraorbital ridge of the frontal, the zygomatic arches as well as the premaxilla are missing. The teeth of the left side are all well preserved except for P2, P3, and part of the C which are preserved but on another part. On the right side, P2 and C are missing, and all the incisors are missing, too. This skull belongs to group XVII of *H. amphibius* 20 age stages defined by Laws (1968), based on tooth replacement and wear. This group corresponds to an ontogenetic age of 35±4 years in the living *H. amphibius.*

Specimen KA-A-105 is an almost complete skull of an adult *H. creutzburgi* overall medium preserved, although dorsally flattened. Due to the deformation, the occipital bone is angled and not at the same level as the maxilla, and the teeth rows are not at the same level. The deformation was performed during the deposition because of the weight of sediment accumulation and before the fossilization process due to the lack of sediment in the interior of the skull. The supraorbital ridges of the frontal, the zygomatic arches as well as the premaxilla are missing. The teeth of the left side are all well preserved except for C, and a part of P2. On the right side, P3, P4 and C are missing. All the incisors are missing from both sides. This skull belongs to group XIII of *H. amphibius* 20 age stages defined by Laws (1968), based on tooth replacement and wear. This group corresponds to an ontogenetic age of 24±3 years in the living *H. amphibius.*

Specimen PCUP.14.77 is a fragmented, almost complete ventral side of a skull of *H. creutzburgi* in a plaster mold. The dorsal side of the specimen is flattened. Most of the teeth are preserved, left C, P2, P3 and M1-M3 and right P2, P3, M1-M4. Parts of the occipital and both zygomatic processes are preserved, but the left zygomatic arch has been reconstructed incorrectly. The teeth are distorted, and the right M1 and M2 are fragmented, too. This skull belongs to group XV of *H. amphibius* 20 age stages defined by Laws (1968), based on tooth replacement and wear. This group corresponds to an ontogenetic age of 30±4 years in the living *H. amphibius.*

Specimen KA-A-106 is an almost complete, medium preserved, and fragmented mandible of an adult *H. creutzburgi*. It has a light-brown colour, and it is light-weighted. It consists of two halves that are fused at the mandibular symphysis. The right half is dorsoventrally deformed, but the left is relatively undistorted. The third molar (m3) is missing from both sides as well as the second premolar (p2). Left canine (c) have been moved latero-posteriorly, and the right antero-posteriorly. From the left side, p3, p4, and i2 are missing. Processus coronoideus and processus condylaris are missing from both sides, although a part of the left ramus of the mandible is preserved. This mandible belongs to group XVII of *H. amphibius* 20 age stages defined by Laws (1968), based on tooth replacement and wear. This group corresponds to an ontogenetic age of 35±4 years in the living *H. amphibius*.

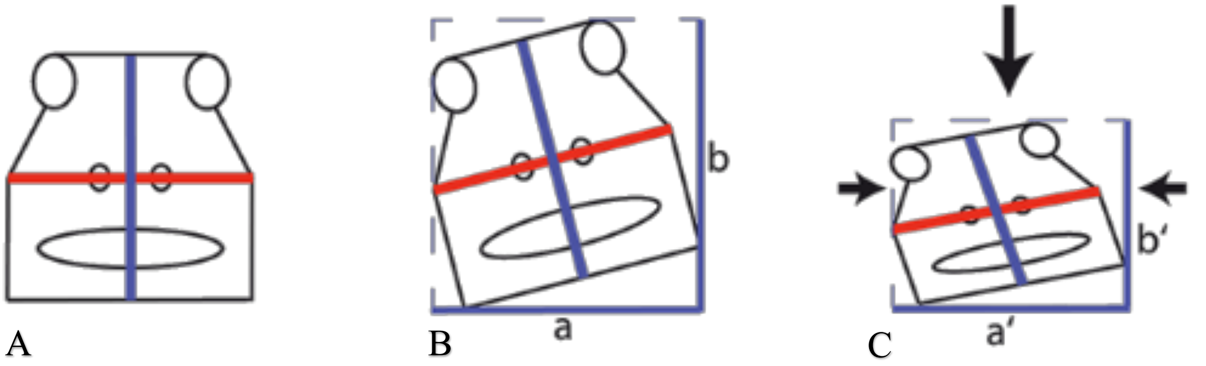

Original skull with bilateral symmetry

Non-orthogonal embedding in the sediment after death

Plastic deformation caused by over-laying rock

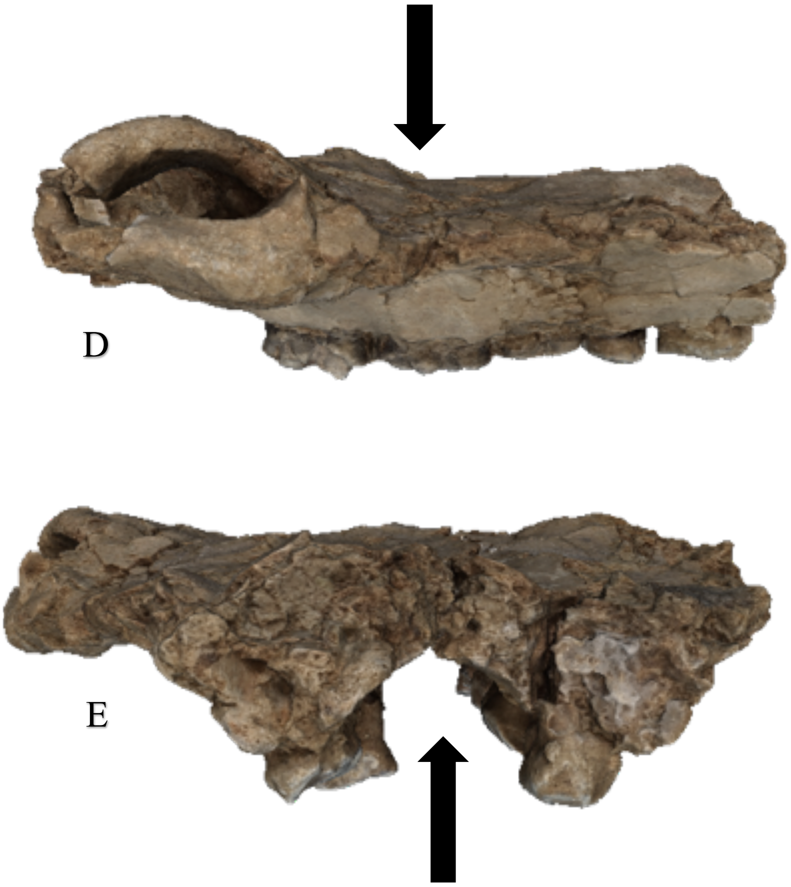

Figure 36. (A) The original bilateral symmetry of the skull, (B) the non-orthogonal embedding is resulting complex plastic deformation, (C) the main directions of diagenetic distortion were dorsoventrally caused by the over-laying sediments and horizontal due to tectonism. (D) The main directions of diagenetic distortion on specimen KA-A-109 in (D) lateral and (E) anterior views. Photo A, B, C modified from Nyakatura et al. (2015).

3.2. Reconstructed Model

Figure 37. The reconstructed 3D model of *H. creutzburgi* cranium in anterior view.

Figure 38. The reconstructed 3D model of *H. creutzburgi* cranium in posterior view.

Figure 39. The reconstructed 3D model of *H. creutzburgi* cranium in left lateral view.

Figure 40. The reconstructed 3D model of *H. creutzburgi* cranium in right lateral view.

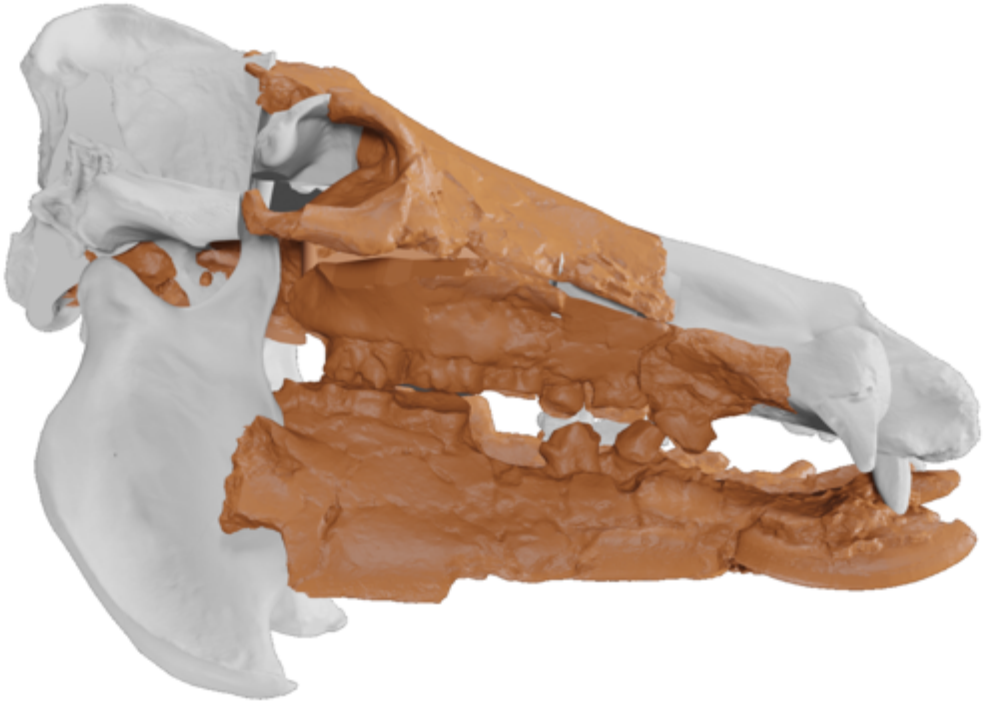

Figure 41. *H. creutzburgi reconstructed* cranium in right lateral view with the addition of subjective elements. Brown tone parts of *H. creutzburgi*, grey tone, are modified parts of *H. amphibius*.

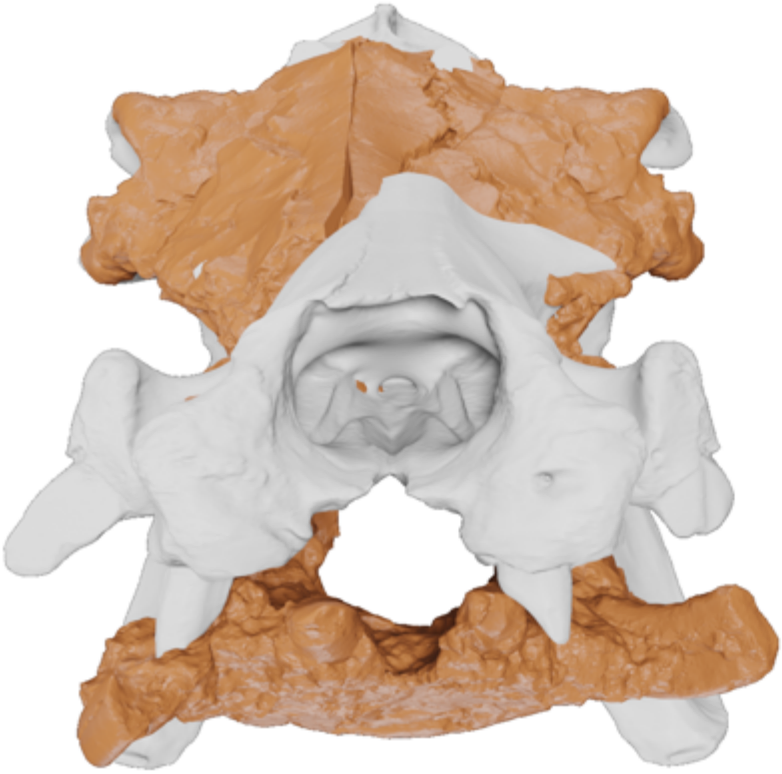

Figure 42. *H. creutzburgi reconstructed* cranium in frontal view with the addition of subjective elements. Brown tone are parts of *H. creutzburgi*, grey tone, are modified parts of *H. amphibius*.

Figure 43. *H. creutzburgi* reconstructed cranium in right lateral view with the additional subjective elements sculpted. Brown tone are parts of *H. creutzburgi*, grey tone, are modified parts of *H. amphibius*.

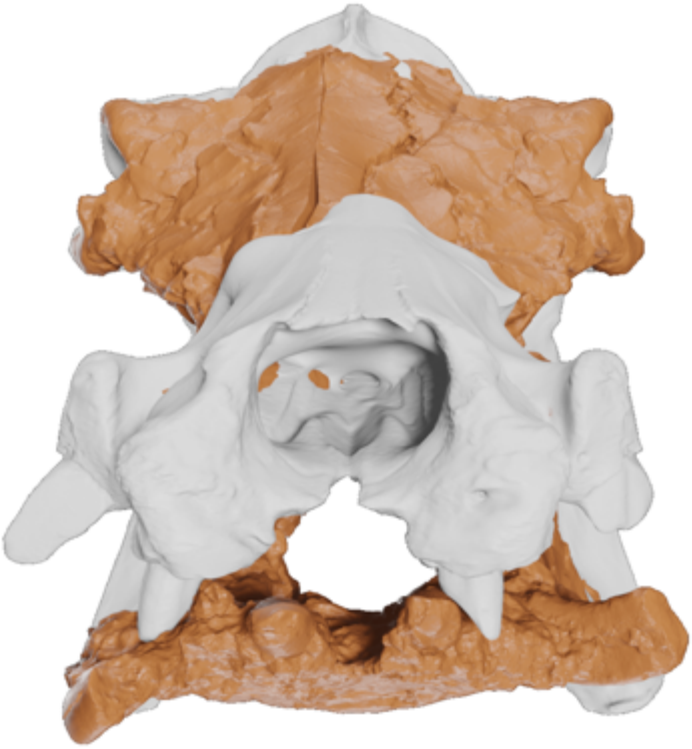

Figure 44. *H. creutzburgi* reconstructed cranium in frontal view with the additional subjective elements sculpted. Brown tone are parts of *H. creutzburgi*, grey tone, are modified parts of *H. amphibius*.

3.3. Reliability of the reconstructed model

From the scatter plots is clear that our reconstructed model of *H. creutzburgi* skull has the correct height for its size. It seems to be close to the general size of the Malagasy hippopotamuses and has about the same skull height with *Ch. liberiensis*. It is also near with the general size of a stage VII male juvenile *H. amphibius* as well as a stage VII juvenile *H. lemerlei*.

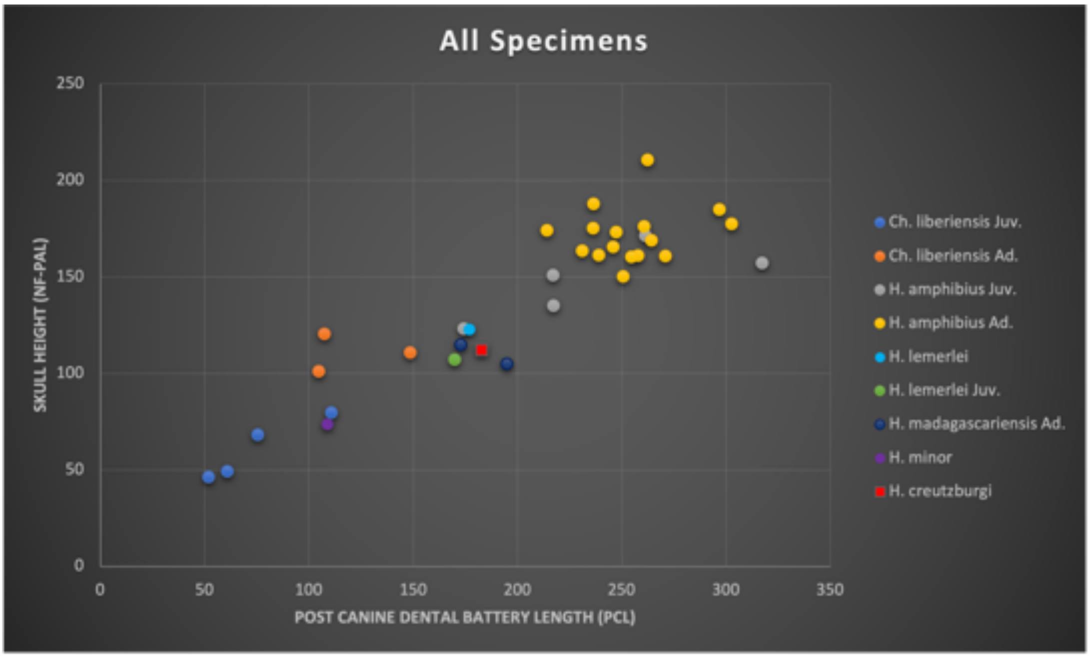

Figure 45. Scatter plot of skull height in relation to post canine dental battery length of all specimens.

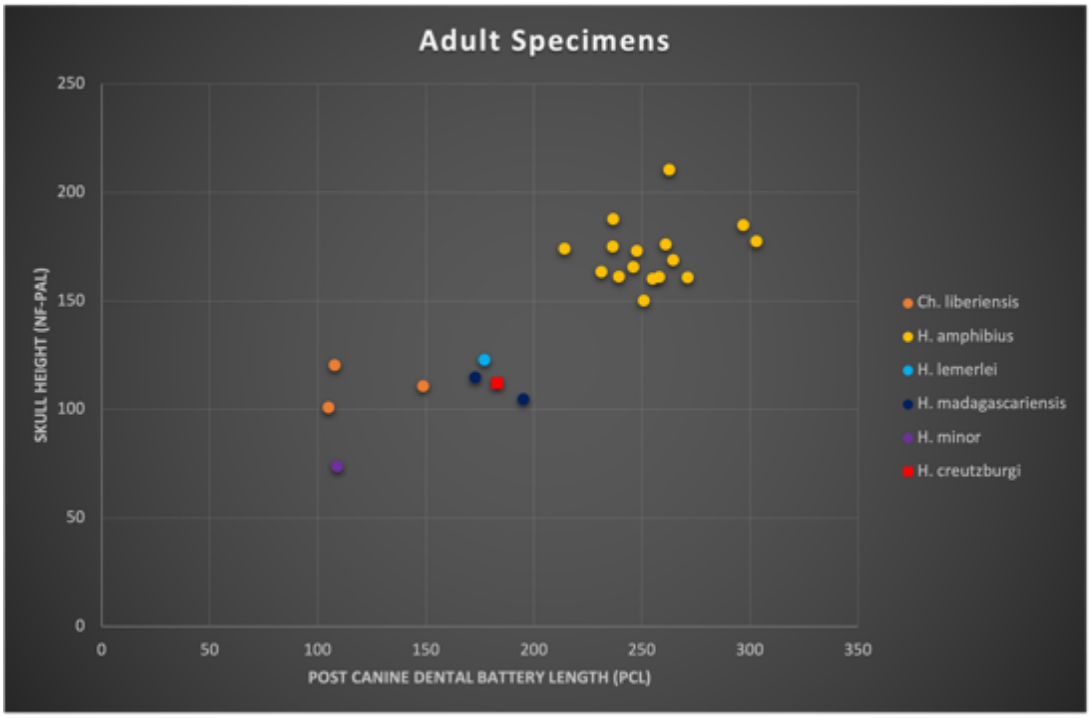

Figure 46. Scatter plot of skull height in relation to post canine dental battery length of adult specimens.

3.4. Anatomical description of *Hippopotamus creutzburgi*

3.4.1. Skull

The skull of *Hippopotamus creutzburgi* is tetraprotodont, relatively short and narrow muzzled with wide teeth (Fig. 47 B, Fig. 48 B). The zygomatic arch is formed by two bones: the zygomatic bone anteriorly and the temporal bone posteriorly. The zygomatic crest is relatively thin (Fig. 47 C, ii, Fig. 48 C, iv). The relative position of the anterior border of the orbit is above M3 (Fig. 47 C, iii and Fig. 48 C, v). The supraorbital margin is thick (Fig. 47 C, i, Fig. 48 C, i). The notch on the anterior border of the orbit is deep and narrow (Fig. 47 A, i, Fig. 48 A, ii). The nasal bones run from the level of the middle of the orbits to the front of the muzzle (Fig. 49 A). There is an incision at the median line that separates the two nasal bones. They are almost parallel and at the level of the anterior of the orbits diverge and then converge. Posteriorly, they create a small hollow that the anterior of the frontal bone fills (Fig. 49 A).

Ventrally, its teeth are big compared to the overall skull size, and the diastemas are either small or absent (Fig. 47 B, Fig. 48 B). The palatinum is narrower in the middle (M1-M2 area) and wider in the rostral and caudal portions (Fig. 48 B). There is a medial suture that runs from the anterior to the posterior part of the palatine process of the maxilla (Fig. 47 B). Compared to the lateral extension of the skull canine apophyses, it has a weak post-canine constriction of the muzzle (Fig. 48 B, iii). The morphology of the facial crest is consistently convex, gradually sloping posterolaterally from the zygomatic process of the frontal bone toward the maxilla (Fig. 47 B, i, Fig. 48 B, i). The outline of the glenoid articular area is enlarged with diffuse borders with an elongated shape. These anterior and posterior borders are not rectilinear and laterally converging (Fig. 47 D, i).

Based on our reconstructed model, we could describe some possible characteristics of this species, but as there is not an undistorted specimen, they remain just possible. In lateral view, the dorsal surface slopes from the anterior to the posterior of the skull while the ventral surface is horizontal (Fig. 48 C). The profile of the cranial roof is angulated with the angle located just anterior to the orbits (Fig. 48 C, i). The size of the orbits is large relative to the face (Fig. 47 C, Fig. 48 C). The orbits are slightly above the level of the cranial roof (Fig. 47 A, ii and Fig. 48 C). Premaxilla is not preserved, but the structure of canine eminence indicates that the inter-premaxillae suture is not complete, and there is a gap between the premaxillae (Fig. 48 B, ii).

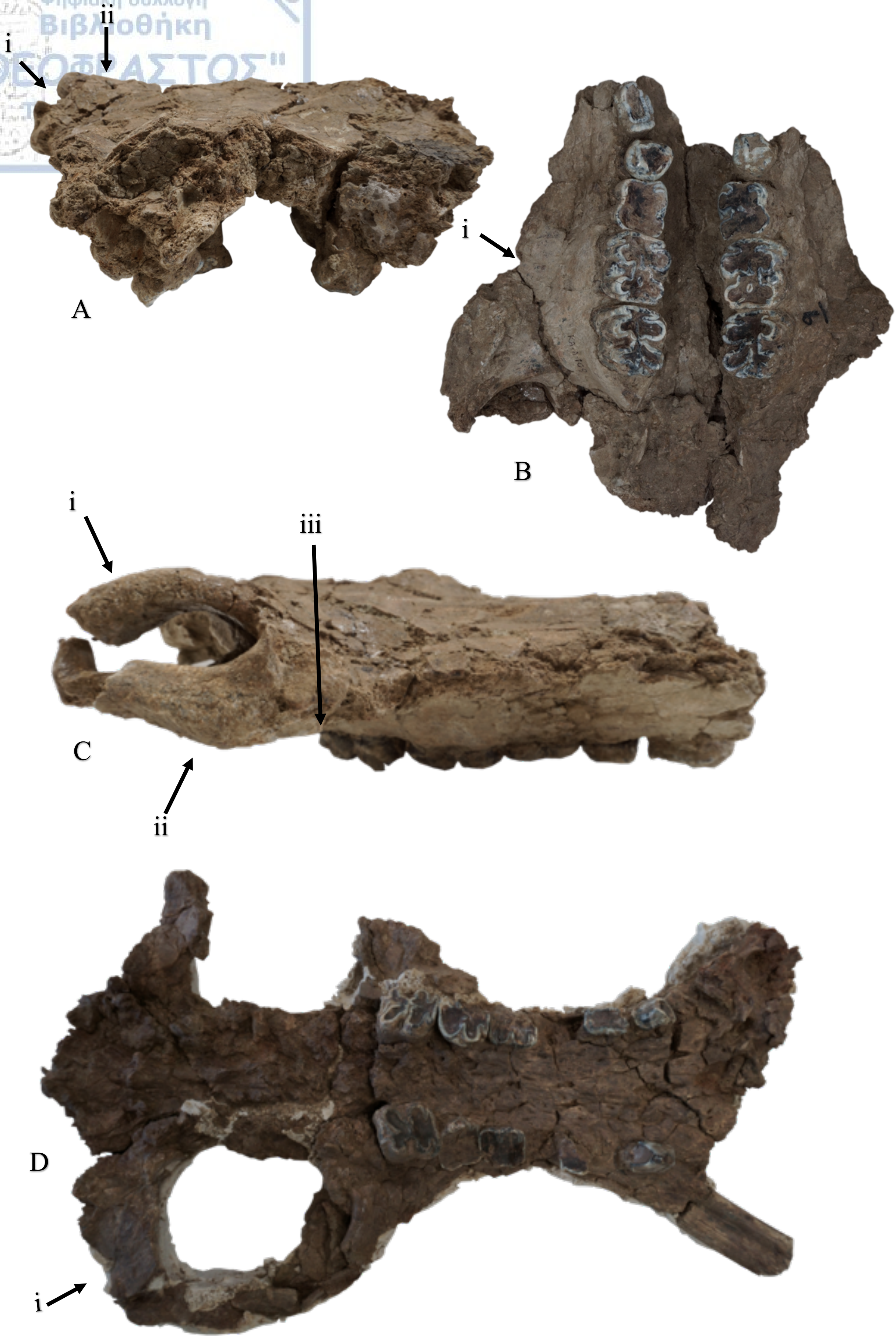

Figure 47. Specimen KA-A-109 in (A) frontal, (B) ventral, (C) right lateral views and (D) specimen PCUP.14.77 in ventral view. The arrows indicate discussed characters.

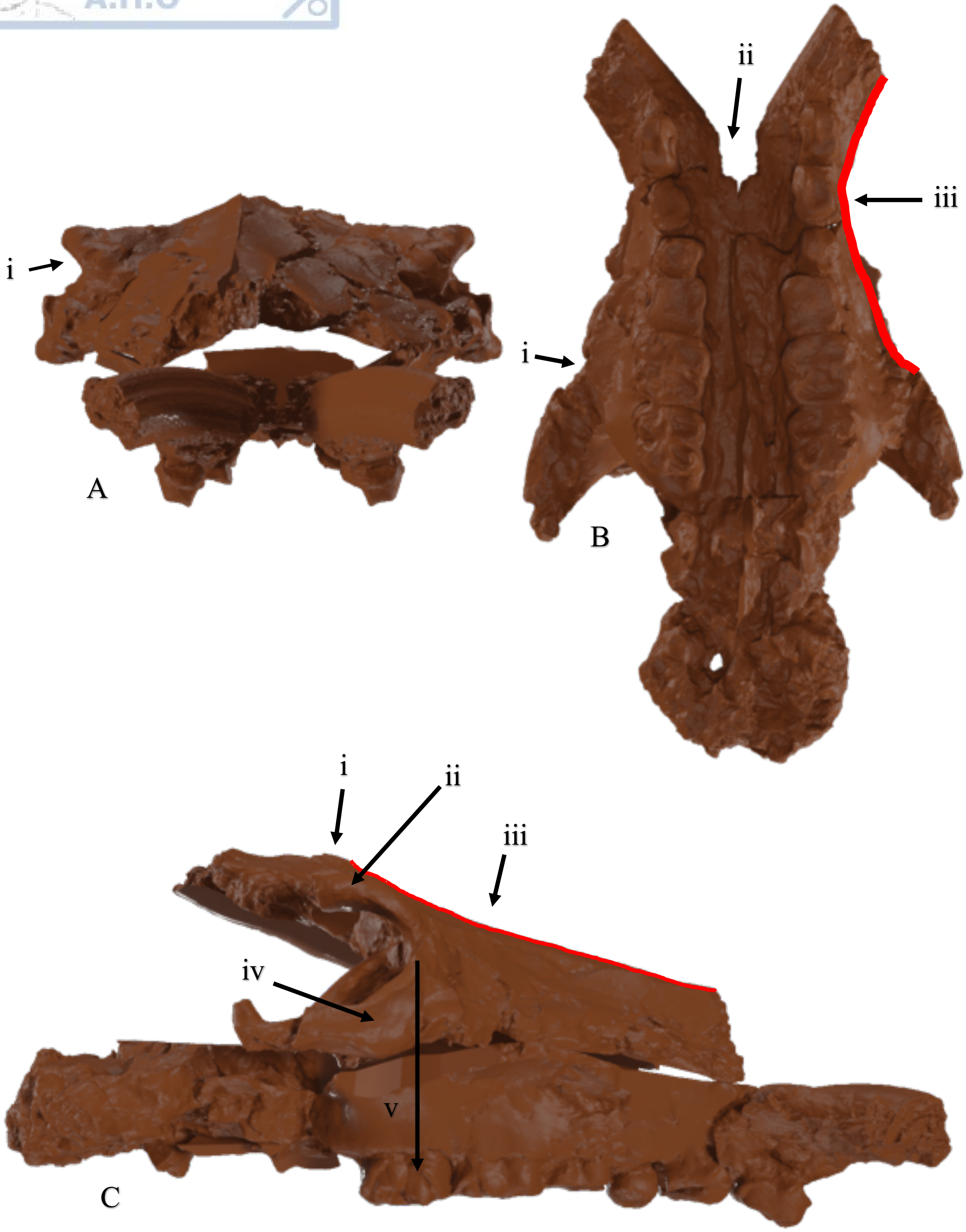

Figure 48. *H. creutzburgi* reconstructed skull in (A) frontal and (B) ventral and (C) right lateral views. The arrows indicate discussed characters.

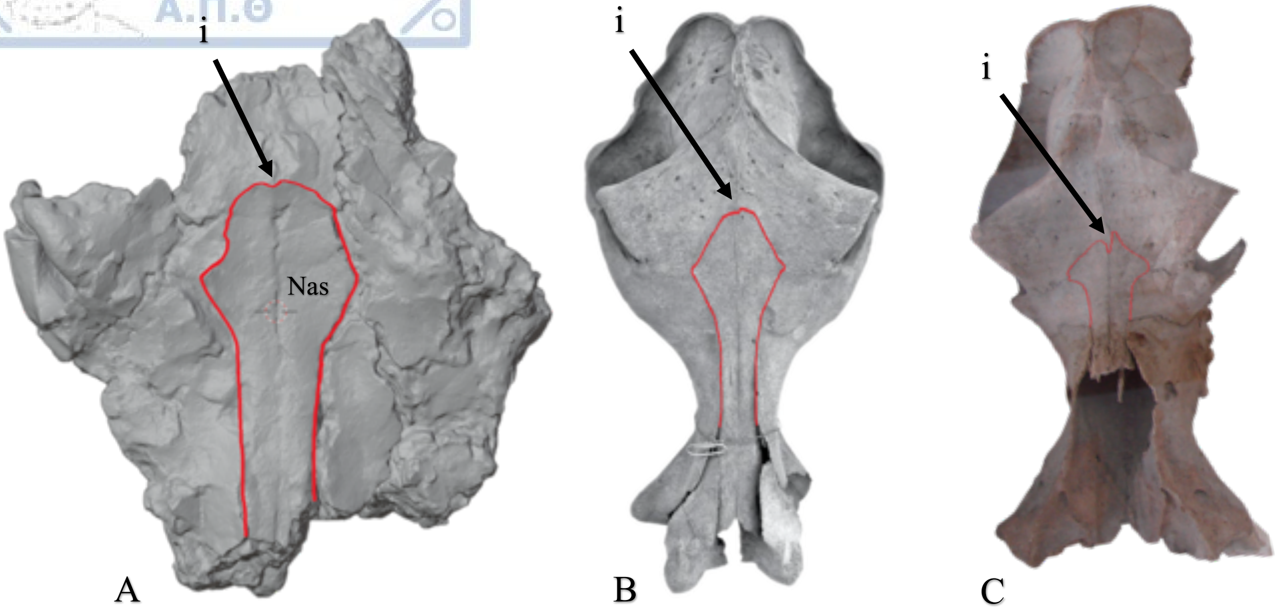

Figure 49. (A) Reconstructed skull of *H. creutzburgi* (specimen KA-A-109), (B) *H. lemerlei* and (C) *H. minor* in dorsal view. Nas=Nasal (Red). Photos: (B) Rakotovao et al. (2014), (C) Wikimedia commons, https://commons.wikimedia.org/wiki/File:Cypriot_pygmy_hippopotamus_skull_and_jaw.jpg

3.4.2. Maxillary dentition

The teeth of *H. creutzburgi* are bunodont with the well-known trefoil shaped molars due to the wear. Its dental formula is 2I, 1C, 3P, 3M with 18 teeth in total. The incisors (I1,I2) are missing, so a description is not possible. The canines (C) are oval-shaped and slightly curved. The characteristic groove found in the posterior region of *Hippopotamus* canines is distinct but shallow. Another narrow one is present on the medial side. Looking at its cross-section, the posterior groove is located on the lingual side of the tooth. The root of the canine starts above the P2. The second premolar (P2) is monocuspid, has a conical shape, and a well-developed cingulum is recognisable perimetrically of the tooth. The third premolar (P3) has one cusp and a well-developed cingulum on all sides except the buccal. The fourth (P4) has the most developed cingulum of the premolars. The cingulum appears on all sides but not on the mesial, and even though is monocuspid, it has two lobes. It also has two roots.

The first molar (M1) is the most worn of all teeth. Especially on the right side, protocone, paracone, metacone, and metaconule are usually completely fused. On the right one, the mesial cingulum ridge is well-developed and fused with the protocone and paracone lobes. The distant cingulum ridge is completely worn, and metacone and metaconule are connected. The second molar (M2) is bigger than the first and less worn-out. All cusps are usually fused with each other. The mesial cingulum ridge is fused with the protocone and paracone lobes. The cingulum is well developed and in the buccal area, there is a well-recognisable mesostyl. Lingually, there is a cingulum ridge at the same point but across the mesostyl. The third molar (M3) is smaller than the second and less worn. The lobes are more clearly distinct. The mesial cingulum ridge is fused with the protocone and paracone lobes. The distal ridge is well developed and smaller than the mesial one. On the lingual side, there is a cingulum ridge equivalent to the one of M2; on the buccal side, there is a mesostyl smaller than the one of M2. The metacone and metaconule are not connected and the metaconule has a well-recognisable teardrop shape.

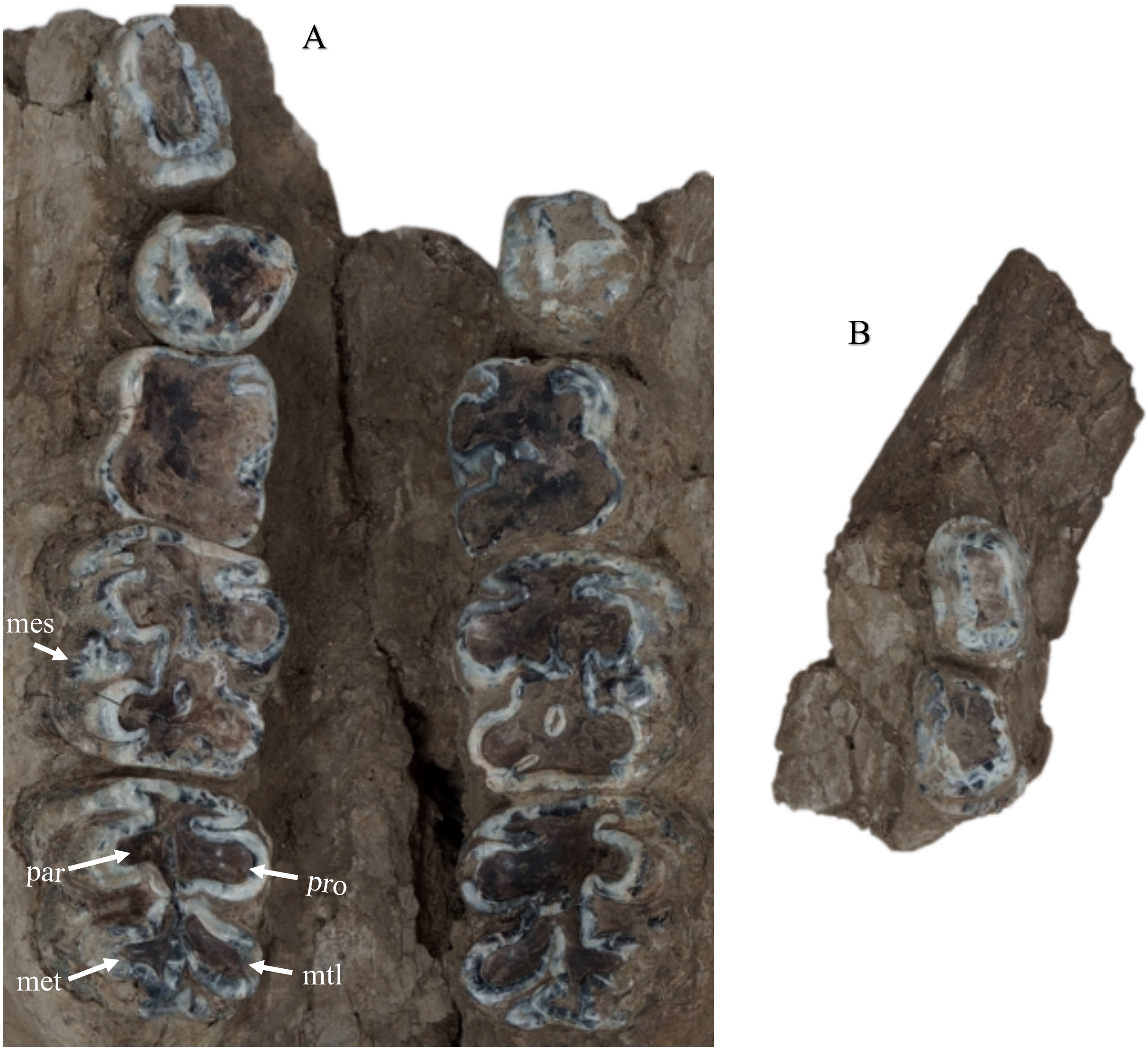

Figure 50. Post canine dental battery of *H. creutzburgi*. (A) Right P3-M3 and Left P4-M3. (B) Left P2 and P3. Legend: mes = mesostyl, par = paracone, prot = protocone, met = metacone, mtl = metaconule.

3.4.3. Mandible

The mandible of *Hippopotamus creutzburgi* is delicate. The i1-i1 diastema (22 mm) is longer than the mesiodistal diameter of the i1 (17.6 mm). In dorsal view, the position of the canine alveolus is at the same level or posterior relative to the incisor alveoli. The canine processes are developed. The mandibular symphysis extends posteriorly as far as the anterior of p3 (Fig. 51 A, i). In lateral view, the orientation of the symphysis plane is anterodorsally inclined (Fig.

51 B, i). The alveolar walls of the lower canines are relatively thick. With the creation of a sagittal cross section between the first incisors and laterally looking, the orientation of the symphysis plane is anterodorsally inclined (Fig. 52 i) and the transition between the frontal and ventral faces of the symphysis creates an abrupt angle (Fig. 52 ii). Viewing the same cross-section, the incisor alveolar process continues between the two canines forming an overhang relative to the frontal face of the symphysis (Fig. 52, iii). The gonial angle is well-developed and has a hook shape (Fig. 51 B, ii). The lateral expansion of the gonial angle is laterally warped away from the corpus direction (Fig. 51 B, ii).

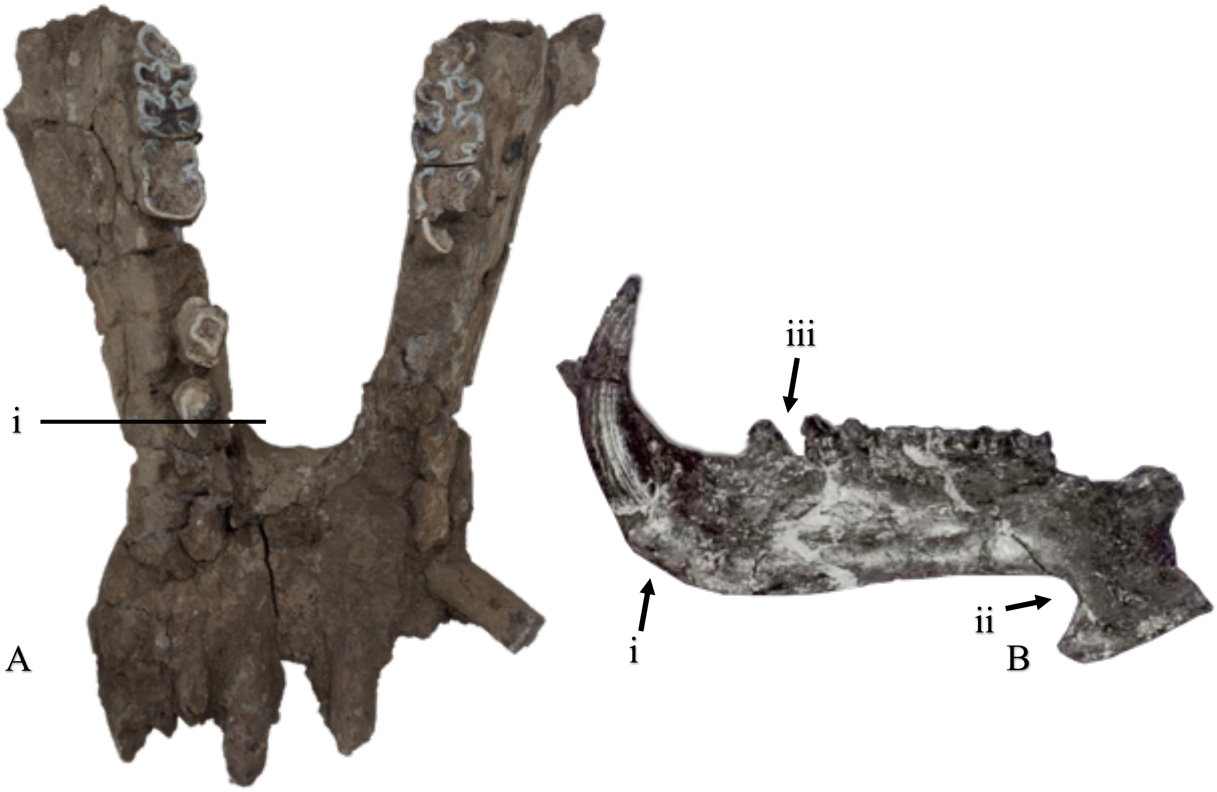

Figure 51. (A) *H. creutzburgi* mandible in dorsal view and (B) an almost complete hemi-mandible (specimen MPUR/ V2032) in left lateral view. Photo (B): Marra, 2005b. The arrows indicate discussed characters.

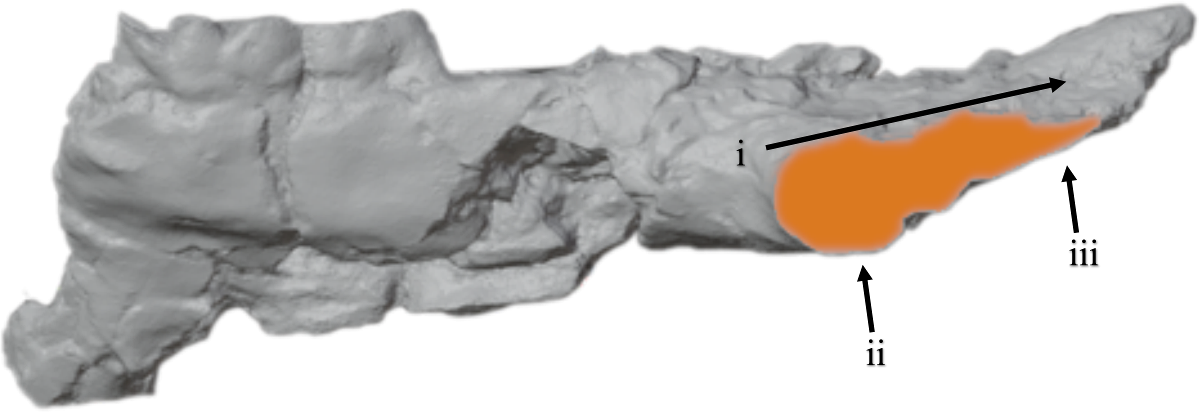

Figure 52. Cross-section of the mandibular symphysis of *H. creutzburgi* made in Blender. The arrows indicate discussed characters.

3.4.4. Mandibular dentition

The mandible is tetraprotodont and its dental formula is $2i, 1c, 3p, 3m$ with 18 teeth in total. Its teeth are bunodont with the well-known trefoil shaped molars due to the wear. Both lower incisors (i1,i2) are rectilinear and has a generally cylindrical shape that becomes pointed anteriorly. The first incisor (i1) is bigger, widder, and looks more robust than the second one (i2). The i2 is positioned more dorsally than the i1. The canine is curved upwards, and its section is oval-shaped. There is a shallow groove throughout the lingual side of the tooth. The premolars are inclined forward. The second (p2) and the third premolars (p3) have a conical shape and are monocuspid with a short cingulum on the buccal side. There is a small diastema between these two teeth. Viewing buccally, the fourth premolar (p4) has a triangular shape and is mesiodistally wider. It has a well-developed cingulum on all sides except for the buccal. It is bigger than p3, more worn and occlusally has a rhomboid shape. The first and the second molar (m1, m2) is similar with the corresponding upper molars. The third molar (m3) has a smaller extra cusp distally of the hypoconid, the hypoconulid. There is no cingulum on any lower molar.

4. Discussion

4.1. Comparison to other Hippopotaminae

4.1.1. General discussion

Hippopotamus creutzburgi was one of the smallest hippos ever existed. It weighed about 400 kg which is 12% of that of its mainland relative *H. antiquus* (Lomolino et al., 2013). The extant *H. amphibius* weighs approximately 1,500-3,000 kg (Eltringham, 1999), and all the other Pleistocene hippos from the Mediterranean islands were bigger than the dwarf hippo from Crete with one exception. The biggest one was *H. pentlandi* from the early Late Pleistocene of Sicily, which weighed approximately 1,100 kg (Lomolino et al., 2013). *Hippopotamus melitensis* from the late Middle Pleistocene of Malta was a medium-sized hippo that weighed about 900 kg (Lomolino et al., 2013). The only exception was *H. minor* from the Pleistocene of Cyprus which is the smallest hippo ever recorded and its weight was about 130 kg (Lomolino et al., 2013). The extant pygmy hippo, *Choeropsis liberiensis*, is also smaller than *H. creutzburgi*, with a typical weight of 160-275 kg. The hippopotamuses from Madagascar were around the same size as *H. creutzburgi*. In 2009, Eleanor Weston and Adrian Lister estimated the body mass of *H. lemerlei* at 374 kg and that of *H. madagascariensis* at 393 kg.

Hippopotamus creutzburgi is well-known for its meta-cranial features, such as its limb bones adapted to a terrestrial environment that evolved by living in the rocky environment of the Katharó plateau (Boekschoten and Sondaar, 1966). In the cranial skeleton, the lower orbits, are terrestrial characters similar to *Hippopotamus minor*, *Hippopotamus madagascariensis*, and *Choeropsis liberiensis* (Stuenes, 1989). The orbit area is larger in the dwarf hippos compared to that of *H. amphibius*, and the general morphology of the skull and mandible is similar to young *H. amphibius* individuals (van der Geer et al., 2018), and more primitive hippos such as *Hexaprotodon*.

4.1.2. Skull and maxillary dentition

Comparing the cranium of *Hippopotamus creutzburgi* with *H. amphibius, H. antiquus, H. minor, H. pentlandi, H. madagascariensis, H. lemerlei*, and *Choeropsis liberiensis* we detected the following similarities and differences:

The skull of *Hippopotamus creutzburgi* has a narrower palatum (Caloi and Palombo, 1996; Marra, 2005) and ≈8.9 % shorter muzzle than that of *H. amphibius* (see Appendix III). It is less outwardly projected in a similar way to the other hippos. Ventrally, it has a similar outline to juvenile *H. antiquus* (Fig. 56 E), which is weakly constricted in the area of P3. This constriction in *H. amphibius* is deeper than *H. creutzburgi* and located in the area of P2 (Fig. 53 A, i). *H. minor* is the only of the above with a similarly shaped constriction (Fig. 56 C). All these hippos have the same gap at the inter-premaxillae suture except *Choeropsis liberiensis* (Boisserie, 2005, and Fig. 53). The gradual postero-lateral sloping of the facial crest morphology is similar to *H. minor* and juvenile *H. antiquus* (Fig. 53, Fig. 56 C, E). It has a large with diffuse borders outline of the glenoid articular area that is not rectilinear, like the other hippos except for *Ch. liberiensis* (Fig. 47 D, i, Fig. 53, Fig. 56).

Laterally, *H. creutzburgi* has an angulated profile of the cranial roof like the one of *H. madagascariensis* and *H. amphibius* (Fig. 54 C, ii, Fig. 55 A, D). It has relatively thin zygomatic crest like *H. madagascariensis, H. lemerlei, H. pentlandi, H. minor and Ch. liberiensis* (Fig. 55). The supraorbital margin is thick like in *H. pentlandi* and *H. lemerlei* (Fig. 55 C, E). The size of the orbits (Fig. 54 A, B, iii) relative to the face is ≈10% larger (see Appendix III) than in *H. amphibius* (≈24%). The orbit of *H. creutzburgi* is more frontally oriented, like in *H. minor* (Fig. 57). In all those hippos, the relative position of the anterior border of the orbit is at the level of the middle of M2, but in *H. creutzburgi and H. lemerlei* is at the level of M3 (Fig. 54 A, B, iv, Fig. 55). The height of the orbits in *H. creutzburgi* is slightly above the cranial roof, which is observed in more primitive hippo species (van der Made et al., 2017; Fig. 54 A, B, C, i). Dorsally, the nasal bone creates a small hollow that the anterior of the frontal bone fills a similar feature to *H. minor* and *H. lemerlei* (Fig. 49).

The teeth of *H. creutzburgi* are large relative to its skull size compared with *H. amphibius* or *H. antiquus*. Differences in teeth size are also observed in *H. floresiensis*, whose teeth are large for its size, relative to *H. sapiens* and *H. erectus* (Brown et al. 2004). Its upper canine has a long alveolar margin like *H. lemerlei* (Stuenes, 1989; Fig. 58). Looking at the cross-section of the upper canine, the posterior groove is distinct and more similar to *H. amphibius* than *H. antiquus* (Fig. 59, C). Upper cheek teeth rows are generally parallel (Caloi and Palombo, 1996) similar to *H. antiquus* (Marra, 2005b) and *H. lemerlei* (Stuenes, 1989). Marra (2005b) described the metaconule of the second and third molar with a distinct shape of a comma or a teardrop, a common character among the hippopotamuses of Europe from the Pleistocene (Marra, 2005b). In our specimens, only the metaconule of M3 has that shape.

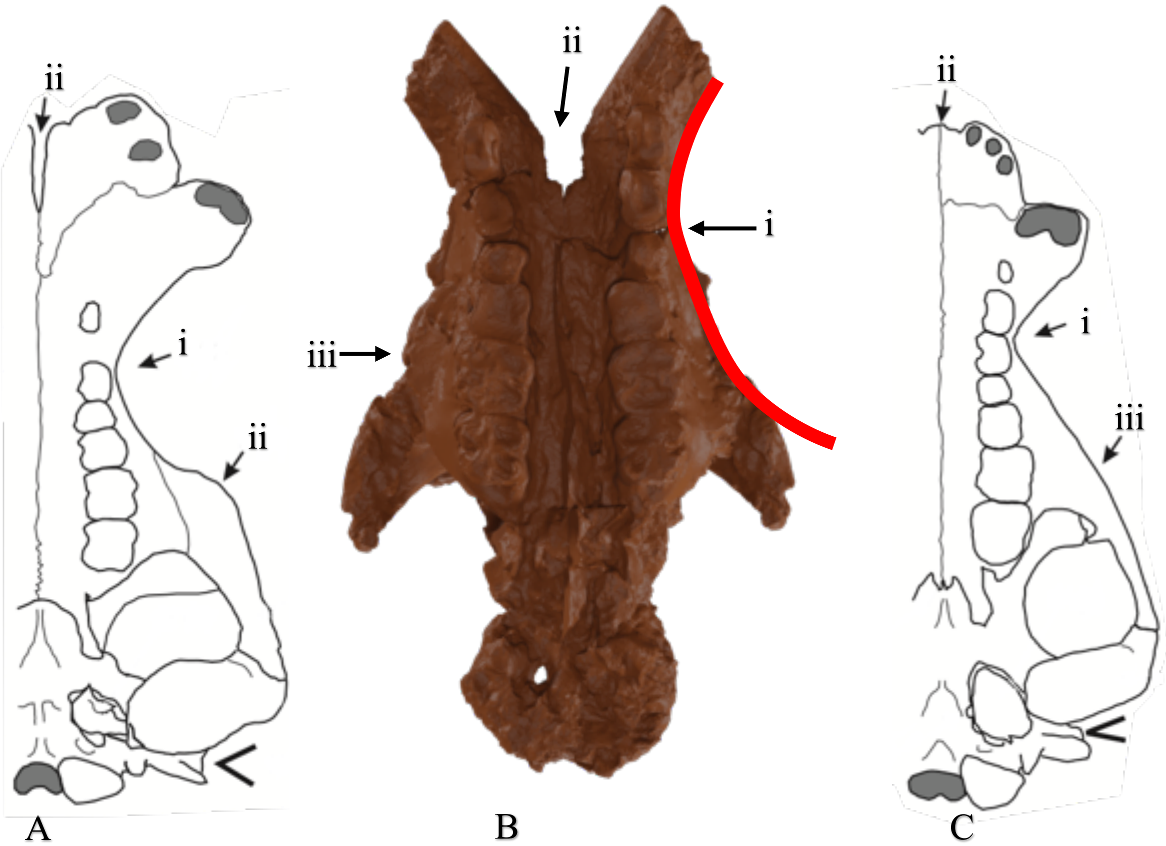

Figure 53. Skulls of (A) *H. amphibius* sketch, (B) reconstructed skull of *H. creutzburgi* and (C) *Ch. liberiensis* sketch in ventral view with their differences marked. Modified from Boisserie, 2005 (Fig. 2.). The arrows indicate discussed characters.

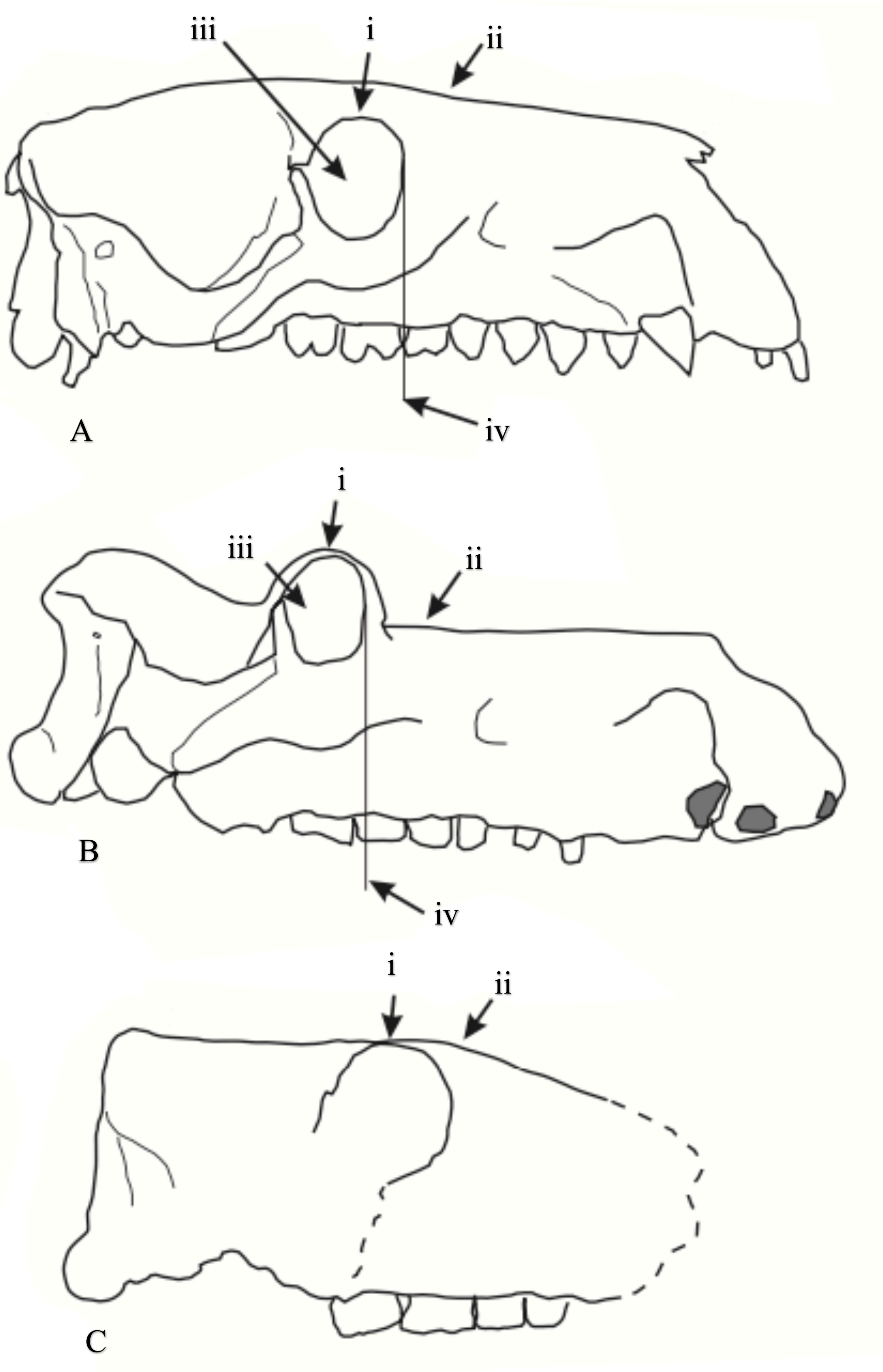

Figure 54. Skulls of (A) *Ch. liberiensis*, (B) *H. amphibius* and (C) *Hex. mingoz* in lateral view. Modified from Boisserie, 2005 (Fig 3.). The arrows indicate discussed characters.

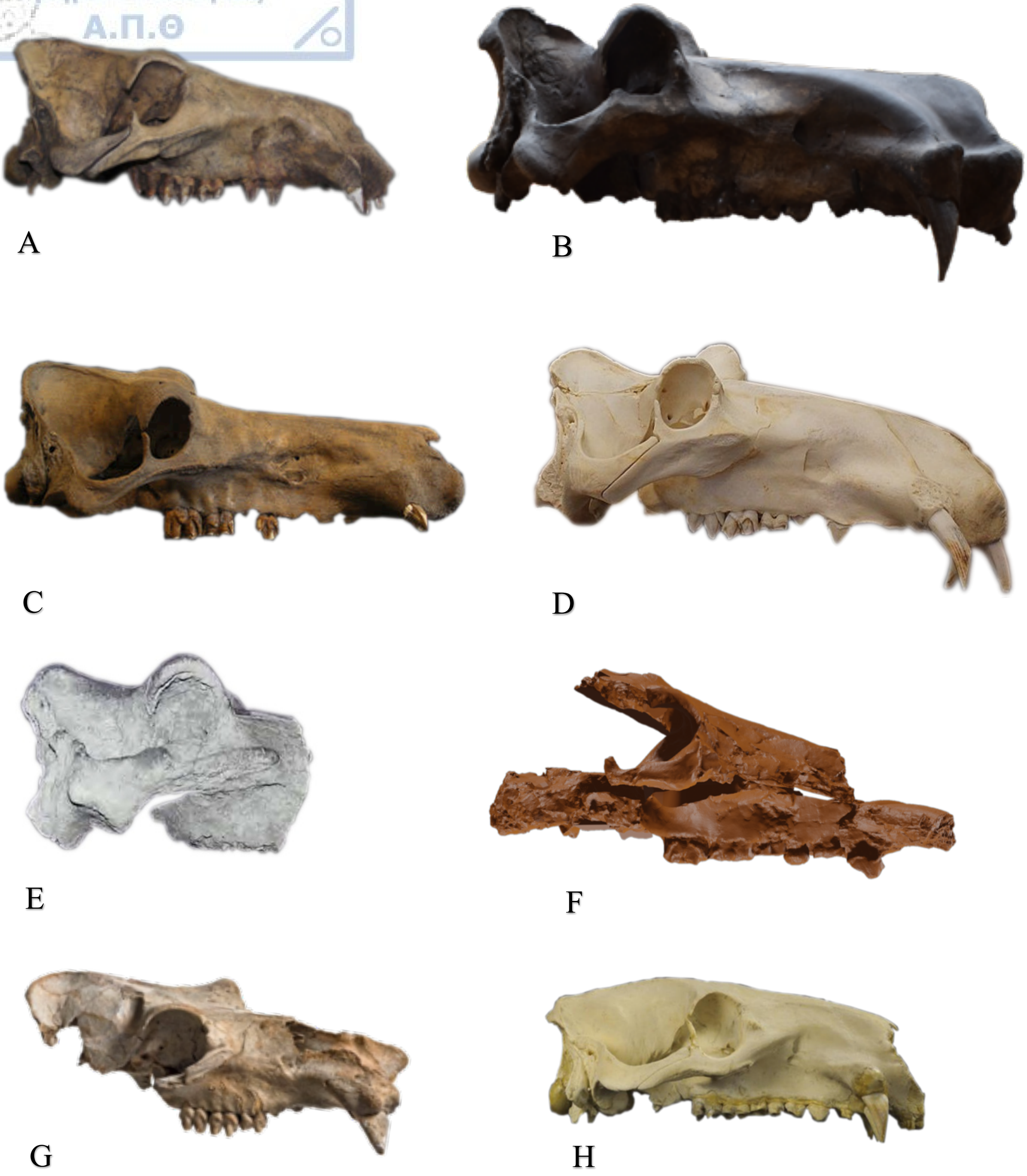

Figure 55. Different skulls of fossil and extant Hippopotaminae in lateral view. (A) *H. madagascariensis* (NHM M7093), (B) *H. antiquus,* (C) *H. lemerlei* (NHM M82190), (D) *H. amphibius*, (E) *H. pentlandi*, (F) *H. creutzburgi*, (G) *H. minor*, (H) *Ch. liberiensis.* Photos: (A) , (C) Yves Lignereux and Marius Rakotovao, (B) George Lyras from MNHN (France), (D) https://commons.wikimedia.org/, (E) Antonella C. Marra, (F) 3D reconstructed model, (G) Smithsonian Magazine (rotated), (H) Gabriella L. Flacke and Jan Decher (2019).

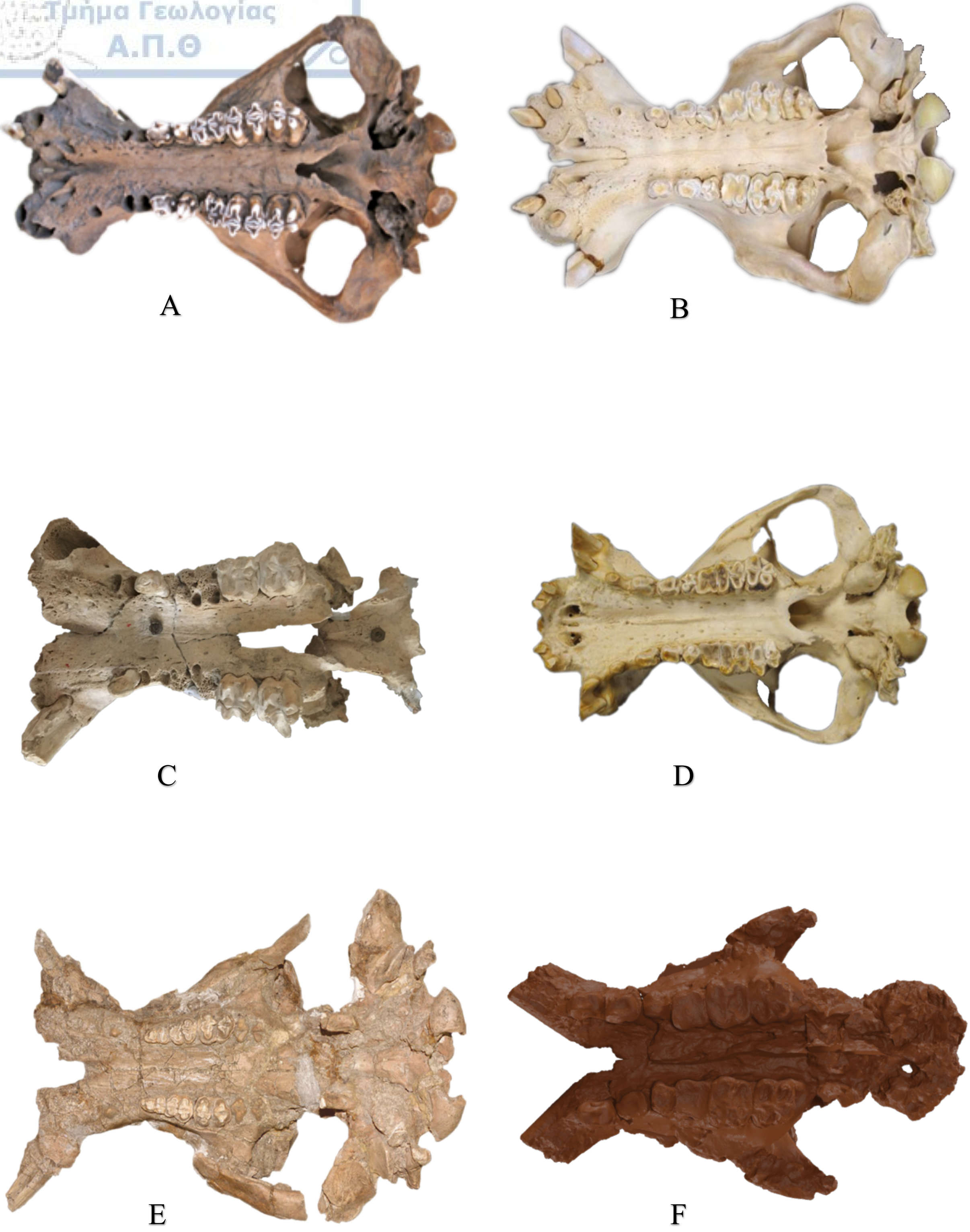

Figure 56. Different skulls fossil and extant Hippopotaminae in ventral view. (A) *H. lemerlei***,** (B) *H. amphibius*, (C) *H. minor*, (D) *Ch. liberiensis*, (E) *H. antiquus* juvenile skull RVL-88, (F) *H. creutzburgi*. Photos: (A) Yves Lignereux and Marius Rakotovao**,** (B) https://lafeber.com/vet/the-wild-side-of-dental-care/, (C) Nikolaos Gerakakis, (D) Gabriella L. Flacke and Jan Decher (2019), (E) Dimitrios Kostopoulos, (F) 3D reconstructed model.

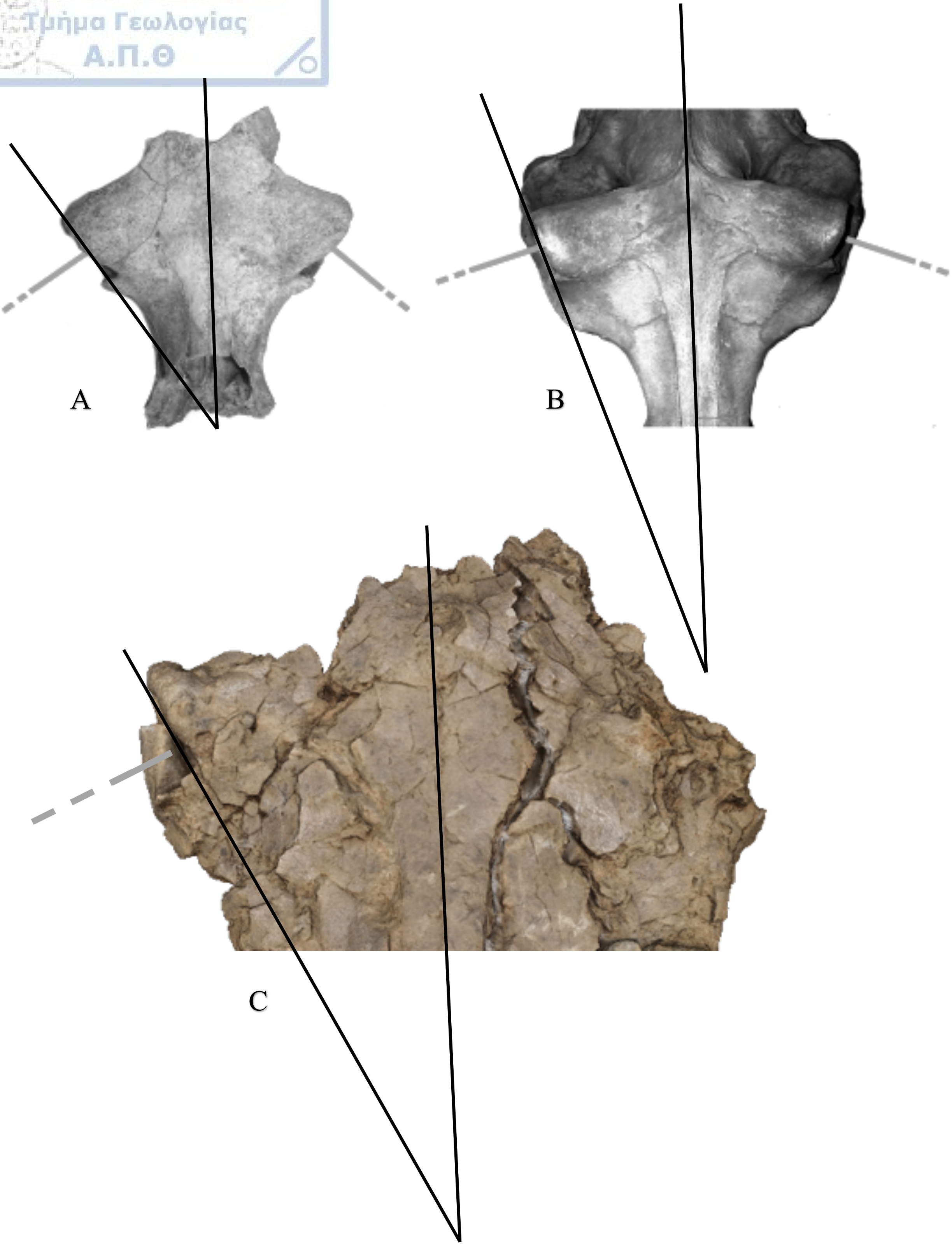

Figure 57. Skull of (A) *H. minor,* (B) *H. amphibius* and (C) *H. creutzburgi* showing a more frontal view of both insular dwarfs in comparison to the mainland extant Hippopotamus. Modified from van der Geer, 2014.

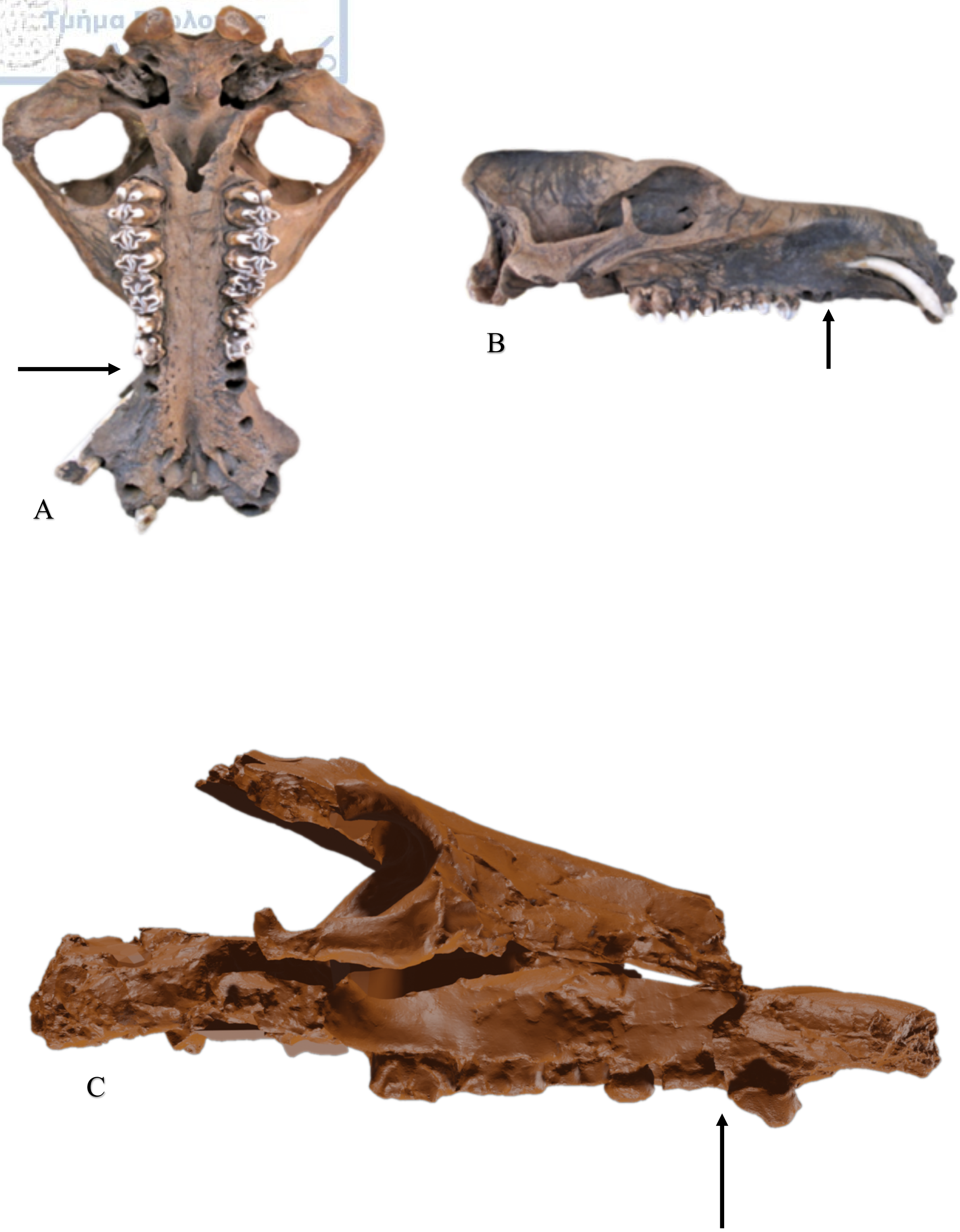

Figure 58. (A) *H. lemerlei* in ventral view, (B) *H. madagascariensis and* (C) reconstructed model of *H. creutzburgi* in lateral view. Photos: (A) and (B) Yves Lignereux and Marius Rakotovao.

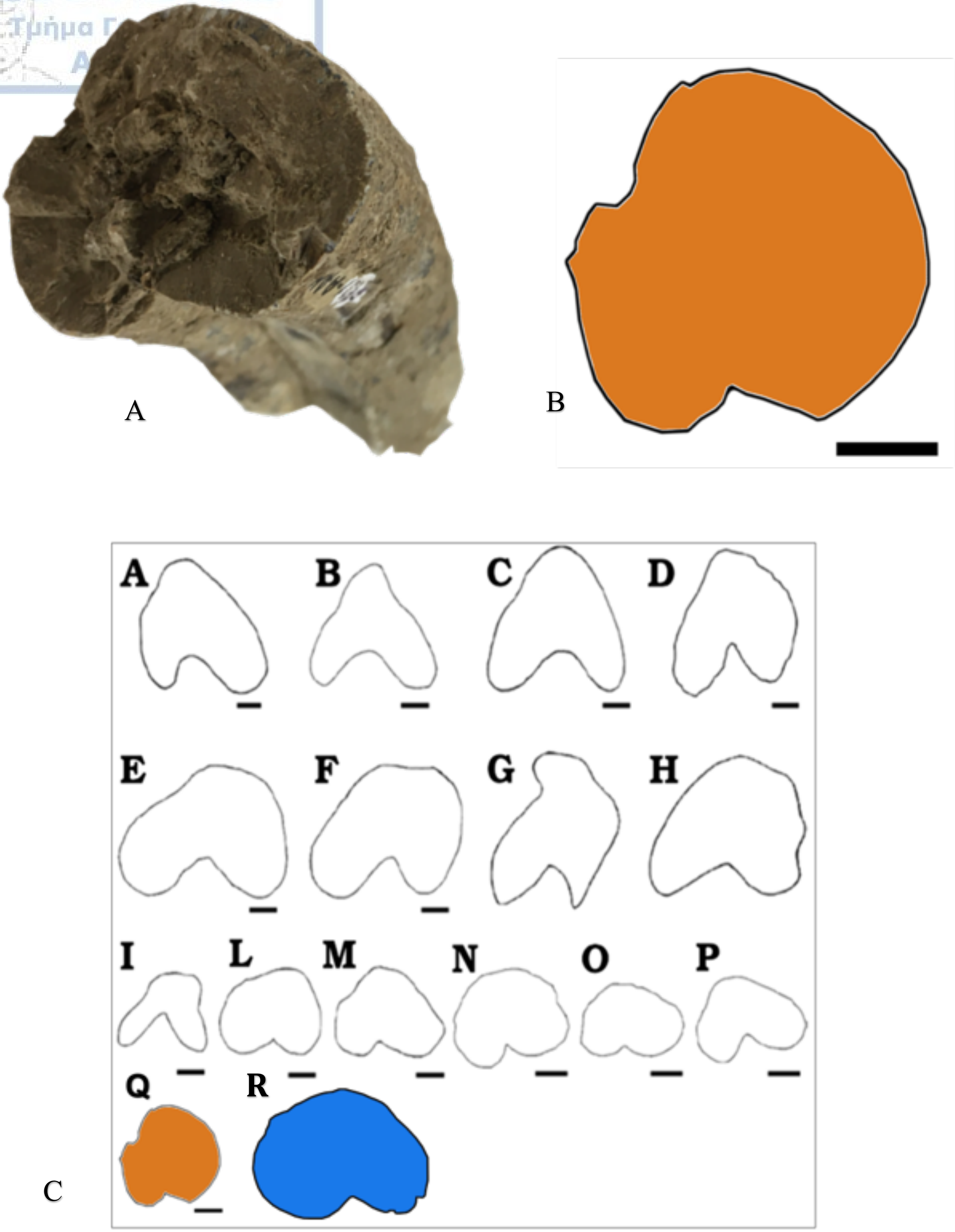

Figure 59. (A) *H. creutzburgi* upper canine cross-section (specimen KA-A-1098, rotated), (B) outline of the cross-section and (C) upper canine of various hippopotamids in cross-section (A-P modified from Martino et al., 2021, R modified from Konidaris et al., 2023). (A) *Archaeopotamus crusafonti*, (B) and (C) *Hexaprotodon*? *siculus,* (D**)** *Hexaprotodon garyam*, (E) and (F) *Hexaprotodon sivalensis*, (G) Subadult *Archaeopotamus harvardi*, (H) Adult *Archaeopotamus harvardi*, (I) *Choeropsis liberiensis*, (L) *Hexaprotodon*? *protamphibius andrewsi*, (M) *Hippopotamus amphibius*, (N–P) Subadult *Hippopotamus amphibius* and (Q) *Hippopotamus creutzburgi,* (R) *Hippopotamus antiquus* (Modified from Konidaris et al., 2023). Scale = 1 cm.

4.1.3. Mandible and mandibular dentition

The first observation about the mandible comparing it to the mandible of the extant *H. amphibius* is how slender it is (Boekschoten and Sondaar, 1966). This feature is common between *H. minor, Ch. liberiensis*, and *H. lemerlei* (Boekschoten and Sondaar, 1966). The position of the canine alveolus is at the same level or posterior relative to the incisor alveoli like in *H. amphibius* (Fig. 60, i). The canine processes are developed like in the other hippos (Fig. 60 B, iv, Fig. 61). The mandibular symphysis is shortened in comparison with the other hippos, and it starts at the level of the distal side of p2 or the mesial side of p3 (Fig. 60 D, ii). The union of the mandible symphysis has an oval outline like in *H. amphibius* but is less projected. The anterior basal region of the symphysis bends upwards like in *H. madagascariensis* (Fig. 61 A, F). The section outline of the symphysis is closer to *Hexaprotodon sivalensis*, *Archaeopotamus qeshta* nov. sp. (AUH 481) and *Archaeopotamus harvardi* (Fig. 62). The cheek toothrows are subparallel, like in *H. pentlandi*, *H. minor*, and *H. antiquus* (Marra, 2005b; Fig. 60). The mandibular angle is similar to *H. madagascariensis* and *H. amphibius* (Fig. 60 E, Fig. 61 A, B, F), which are well developed and hooked shaped (Fig. 60 E). The expansion of the gonial angle is laterally warped away from the corpus like in *H. amphibius* (Fig. 60, v). Generally, *H. creutzburgi* has a similar mandible to *H. madagascariensis* (Boekschoten and Sondaar, 1966; Capasso Barbato et al., 1982).

It has two lower incisors (Fig. 60, iii). The i1-i1 diastema (22 mm) is longer than the mesiodistal diameter of the i1 (17.6 mm) which differs with *H. amphibius* (Fig. 60, ii). A diastema is present between p2 and p3 (Fig. 61), like in the Malagasy hippos, *H. amphibius* and *H. antiquus* contrary to the decrease of the mandible (Marra, 2005b). There is no diastema between p3 and p4, and in the specimen KA-A-106 the gap is caused by the deformation contrary to the observation of Boekschoten and Sondaar (1966), which is a similar character to the other hippos. *Hippopotamus creutzburgi* has an intermediate hypsodonty like *H. melitensis* (Bethune et al., 2019). Comparing its dentition with the others, *H. amphibius* and *H. pentlandi* are the most hypsodont and have the lowest occlusal relief, while *H. minor* is brachyodont and has the highest occlusal relief (Bethune et al., 2019). The enamel surface texture of *H. creutzburgi* is closer to that of *H. amphibius* (Bethune et al., 2019), but it has a simpler enamel pattern. Although, the enamel pattern of *H. creutzburgi* is more complicated than those of *H. minor* and *Ch. liberien*sis (Boekschoten and Sondaar, 1966). The lower canines of *H. creutzburgi* are less curved than those of *H. amphibius* (Fig. 61 D, F). Marra (2005b) described the entoconid of the second and third molar as having a distinct shape of a comma or a teardrop, which is a common character among the hippopotamuses of Europe from the Pleistocene, but the entoconid of the specimen KA-A-106 does not have this shape. This feature is also observed in the lower third molar of *H. lemerlei*, frequently in fossils of *H. amphibius*, occasionally in the living, and is common in *H. antiquus* (Mazza, 1995).

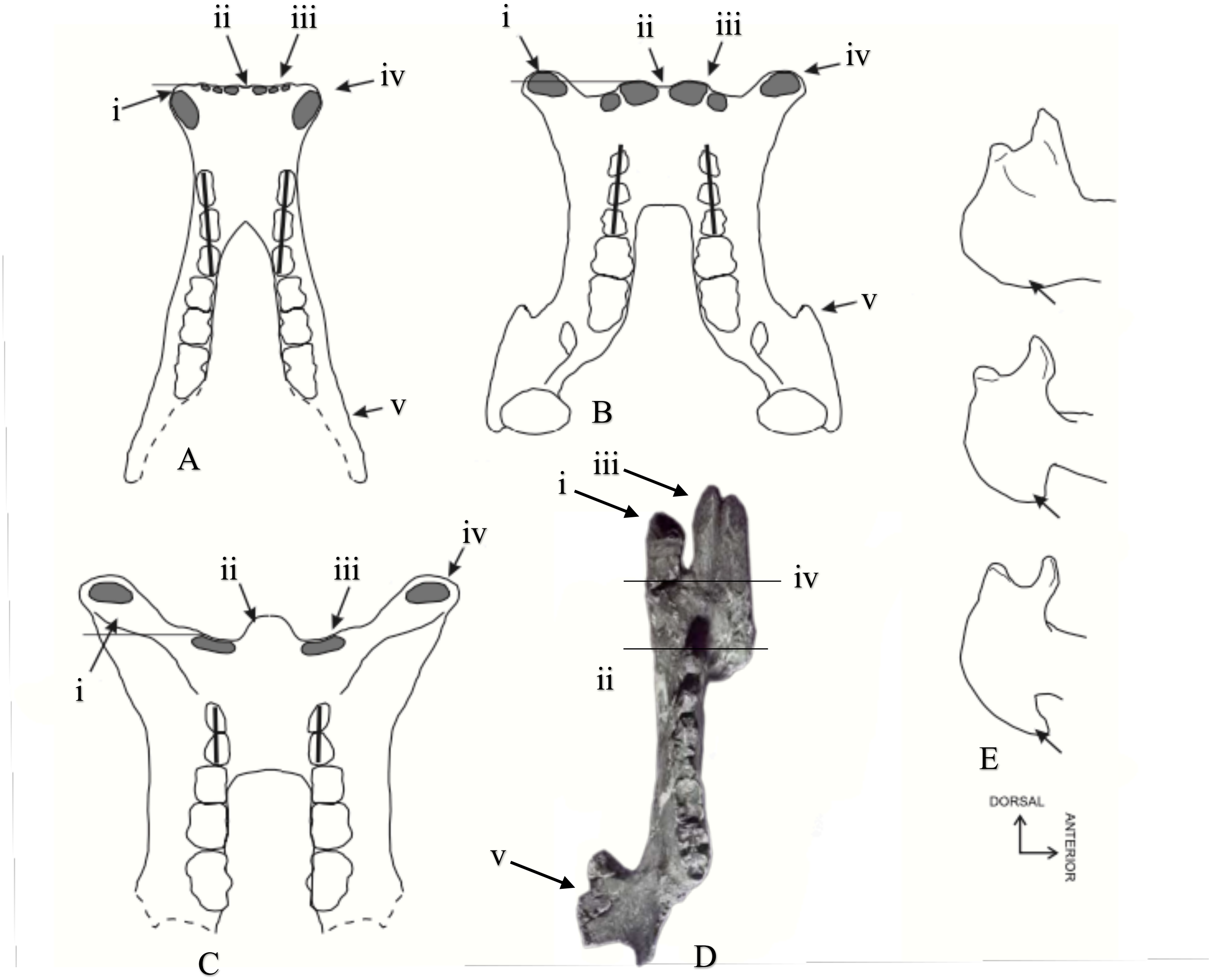

Figure 60. Different mandibular characters. (A) *Hex. aff. sahabiensis*, (B) *H. amphibius*, (C) *Hex. karumensis*, (D) Hemi-mandible of *H. creutzburgi* ((MPUR/V2032) in dorsal view and (E) lateral view of the vertical ramus (from top to bottom: *Anthracokeryx ulnifer*, *Hex, sivalensis*, *H. amphibius*). Modified from Boisserie, 2005; Marra, 2005b.

Figure 61. Different mandibles of fossil and extant hippos in lateral view. (A) *H. madagascariensis*, (B) *H. antiquus,* (C) *H. lemerlei*, (D) *H. amphibius*, (E) *H. pentlandi*, (F) *H. creutzburgi* (MPUR/V 2032), (G) *H. minor*, (H) *Ch. liberiensis.* Photos: (A) https://mineralartgallery.com/, (B) George Lyras from MNHN (France), (C) https://mineralartgallery.com/ (D) https://commons.wikimedia.org/, (E) Antonella C. Marra, (F) Antonella C. Marra (rotated), (G) Alan H. Simmons (rotated), (H) Gabriella L. Flacke and Jan Decher (2019).

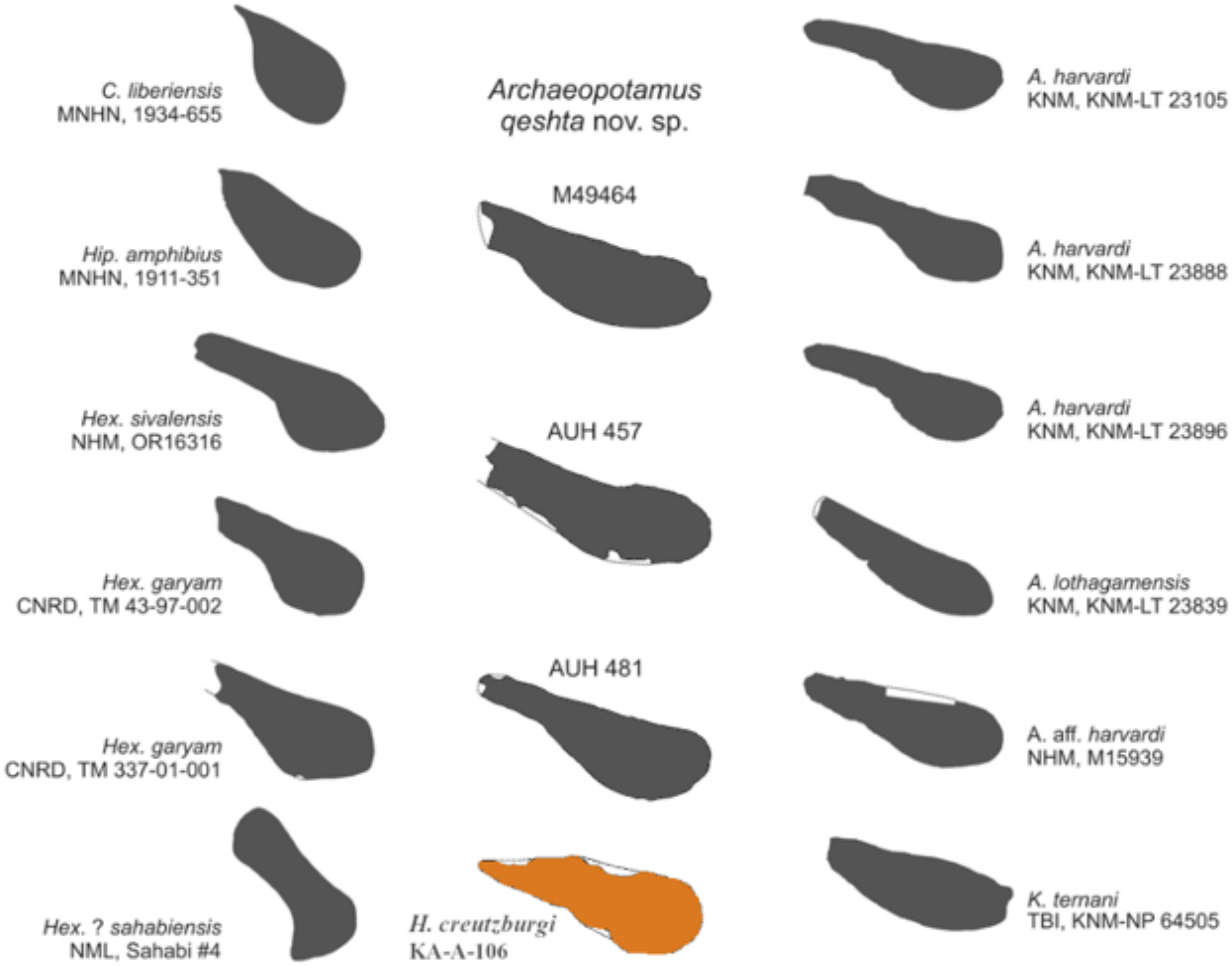

Figure 62. Cross-sections of mandibular symphyses of several Hippopotamidae (modified from Boisserie et al., 2017). All sections are observations of Boisserie et al., 2017, except *Hexaprotodon? sahabiensis* (Pavlakis, 2008: fig. 3) and *H. creutzburgi* which is a direct observation. Orange tone, *H. creutzburgi* and grey tone, other Hippopotamidae.

4.2. Sexual dimorphism

In *Hippopotamus amphibius*, the two sexes are distinguishable by size. Males weigh 506 to 3200 kg and females 655 to 2344 kg (Kingdon, 1979). The lower jaw is where sexual dimorphism is clearly expressed. Males have more developed tusks and incisors, but the molars are the same size in both sexes (Weston, 1998). They have more robust clades, a larger angle between coronoid and condylar processes, and a more robust hooked-shaped mandibular ramus that creates a smaller angle with mandibular corpus. In *Hexaprotodon liberiensis* sexual dimorphism is not expressed with differences in size (Weston, 1998). Both sexes have a similar body mass that ranges from 200 to 270 kg. The dimorphism of the lower incisors is more acute in this species though in canines is less pronounced (Weston, 1998). We detected a significant difference in size among some specimens that we interpreted as a possible sexual dimorphism of *Hippopotamus creutzburgi* expressed in the mandible. Males of the genus *H. creutzburgi* have more developed canine alveolus (Fig. 64), thicker, more developed lower canines and incisors (Fig. 63, Fig. 65) than females, more robust mandibles with thick clades (Fig. 66, Fig. 67), and a similar mandibular angle. However, the molars have relatively the same size. Although our sample is limited, the expression of the sexual dimorphism in *H. creutzburgi* seems similar to *H. amphibius.*

Figure 63. (A) The almost complete mandible of a female *H. creutzburgi* compared with (B) a right lower canine of a male individual. Scale = 5 cm.

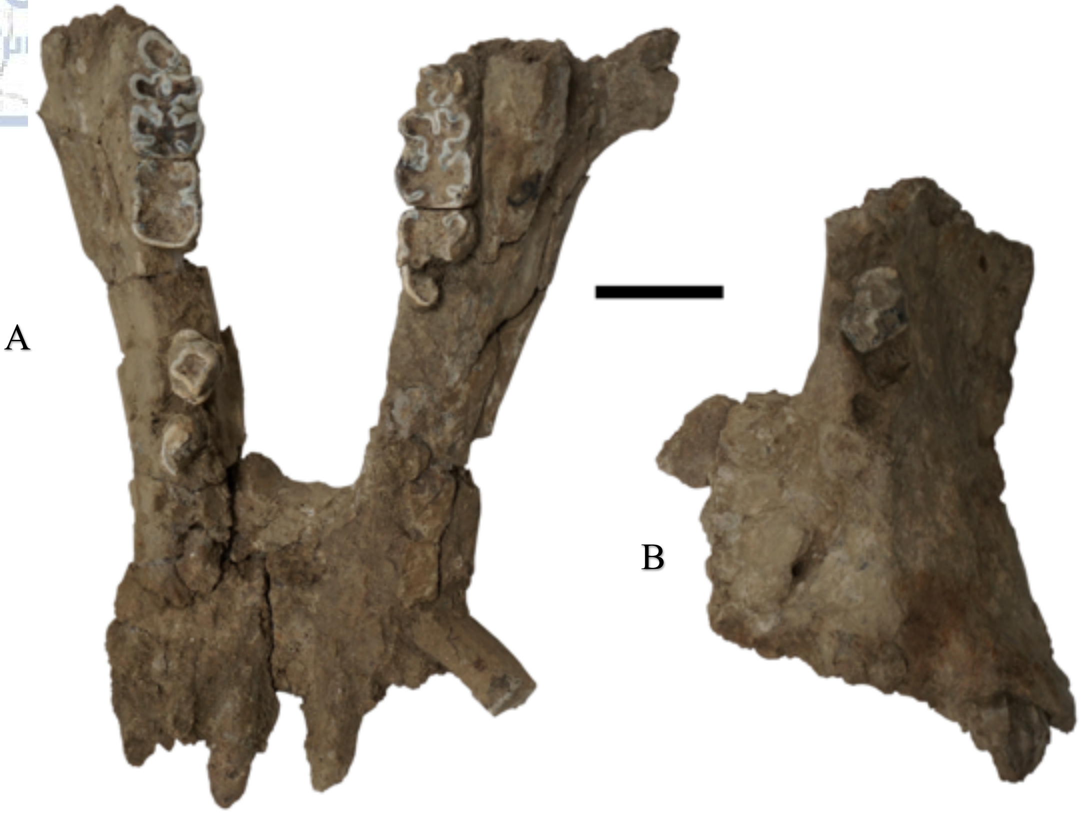

Figure 64. (A) The almost complete mandible of a female *H. creutzburgi* compared with (B) a left anterior mandibular fragment of a male individual. Scale = 5 cm.

Figure 65. (A) The almost complete mandible of a female *H. creutzburgi* compared with (B) the lower first incisors of a male individual. Scale = 5 cm.

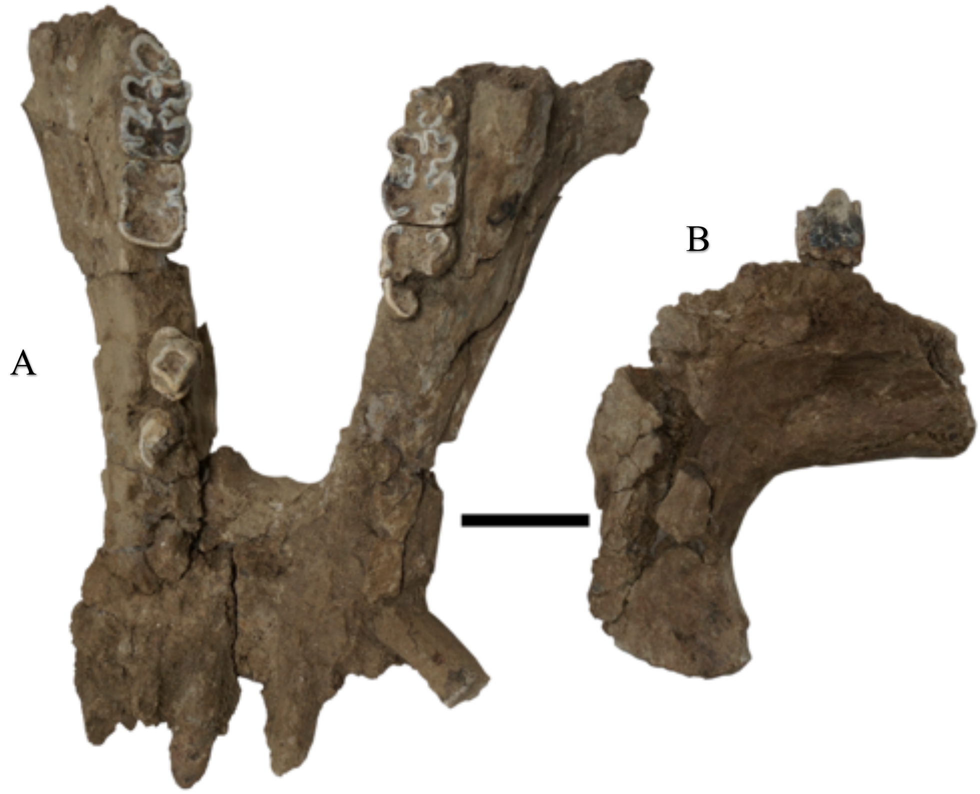

Figure 66. (A) The almost complete mandible of a female *H. creutzburgi* compared with (B) a right posterior mandibular fragment of a male individual. Scale = 5 cm.

Figure 67. (A) The almost complete mandible of a female *H. creutzburgi* compared with (B) a left posterior mandibular fragment of a male individual. Scale = 5 cm.

Figure 68. The almost complete mandible of a female *H. creutzburgi* compared with all the different mandibular fragments of male individuals. Scale = 10 cm.

5. Conclusions

We reconstructed almost the whole cranium of *H. creutzburgi* and produced a complete, though subjective version to better understand its morphology. The missing parts were completed with parts of *H. amphibius*. Based on our reliability test comparing our reconstructed model with other Hippopotaminae, the retrodeformation of the flattened skull was successful concerning its height. However, there is neither an undistorted nor a complete skull to compare it.

We detected some new morphological characteristics on the skull and the mandible of this species. On the skull, the relative position of the anterior border of the orbit is at the level of M3. The supraorbital crest is thick and the notch on the anterior border of the orbit deep and narrow. The nasal bones run from the middle level of the orbits to the front of the muzzle. They are almost parallel and at the level of the anterior of the orbits diverge and then converge. Posteriorly, they create a hollow that the anterior part of the frontal bone fills. The morphology of the facial crest is consistently convex, gradually sloping postero-laterally from the zygomatic process of the frontal bone toward the maxilla. The outline of the glenoid articular area is enlarged with diffuse borders with an elongated shape. These anterior and posterior borders are not rectilinear and laterally converging. The upper canines have a long alveolar margin.

On the mandible, the i1-i1 diastema is longer than the mesiodistal diameter of the i1. The position of the canine alveolus is at the same level or posterior relative to the incisor alveoli. The canine processes are developed. The mandibular symphysis extends posteriorly as far as the anterior of p3. The orientation of the symphysis plane is anterodorsally inclined. The alveolar walls of the lower canines are relatively thick. The gonial angle is well-developed and has a hook shape. The lateral expansion of the gonial angle is laterally warped away from the corpus direction.

Based on our reconstruction, we consider that it has more frontally oriented orbits that are slightly above the cranial roof and the skull has a weak post-canine constriction of the muzzle located in the area of P3. The palatinum is narrower at the middle (M1-M2 area) and wider at the rostral and caudal portions. The inter-premaxillae suture is not complete, and there is a gap between the premaxillae. The angulated profile of the cranial roof with the angle starting anteriorly of the orbits.

We detected a possible sexual dimorphism of this species expressed in the mandible due to the size differences among some specimens. We suggest that males have bigger, more robust mandibles with thick clades, more developed canine alveolus, and longer, more robust lower canines and incisors than females. However, molars have relatively the same size.

Acknowledgments

I would like to thank the members of the examining board, Dr G. Lyras for his supervision, Dr D. Makris, who introduced me to photogrammetry, and Dr S. Roussiakis for his help in the lab during the photography sessions and our conversations. I am also thankful to Dr G. Iliopoulos for giving me access to the skull of *H. creutzburgi* from the Palaeontological Collection of the University of Patras. Thanks to N. Karydas for answering my first questions on Blender and M. Georgitsis for helping me in the lab and suggesting helpful papers. Many thanks to Dr D. Kostopoulos for his support and leadership during the first year of the postgraduate program in Thessaloniki and to all the other professors and researchers that took part in the courses of this program. Lastly, I would like to thank my family for their support, especially during my staying in Thessaloniki.

Bibliography

Abel, R.L., Laurini, C.R. & Richter, M., 2012. A palaeobiologist's guide to 'virtual' micro-CT preparation. Palaeontologia Electronica 15, 2, 6T.

Agenbroad, L.D., Lister, A.M., Mol, D., Roth, V.L., 1994. *Mammuthus primigenius* remains from the mammoth site of Hot Springs, South Dakota. In: Agenbroad, L.D., Mead, J.I. (Eds.), The Hot Springs Mammoth Site: a Decade of Field and Laboratory Research in Paleontology, Geology, and Paleoecology. Mammoth Site, Hot Springs, SD, pp. 269–281.

Alcover, J.A., Moyà-Solà S., Pons-Moyà J., 1981. Les Quimeres dels Passat. Els Vertebrats fòssils del Plio-Quaternari de les Balears i Pitiüses. Monografíes Científiques 1, 1–260.

Athanassiou, A., van der Geer, A.A., Lyras, G.A., 2019. Pleistocene insular Proboscidea of the Eastern Mediterranean: a review and update. Quaternary Science Reviews 218, 306–321.

Bate, D.M.A., 1905. Four and a half months in Crete in search of Pleistocene mammalian remains. Geological Magazine 2, 5, 193–202.

Bates, K.T., Rarity, F., Manning, P.L., Hodgetts, D., Vial, B., Oms, O., Galobart, A., and Gawthorpe, R.L., 2008. High-resolution LiDAR and photogrammetric survey of the Fumanya dinosaur tracksites (Catalonia): Implications for the conservation and interpretation of geological heritage sites: Journal of the Geological Society of London 165, 115–127.

Bethune, E., Kaiser, T. M., Schulz-Kornas, E. & Winkler, D. E., 2019. Multi proxy dietary trait reconstruction in PleistoceneHippopotamidae from the Mediterranean Islands. Palaeogeography, Palaeoclimatology, Palaeoecology 553, 109210.

Boekschoten, G.J., Sondaar, P.Y., 1966. The Pleistocene of the Katharo Basin (Crete) and its Hippopotamus. Bijdr Dierk 36, 8, 17–44.

Boekschoten, G.J., Sondaar, P.Y., 1972. On the fossil Mammalia of Cyprus. Proceedings of the Koninklijke Nederlandse Akademie van Wetenschappen 75, 4, 306–338.

Boisserie,J.R., 2005. The phylogeny and taxonomy of Hippopotamidae (Mammalia: Artiodactyla): a review based on morphology and cladistic analysis. Zoological Journal of the Linnean Society 143, 1, 1–26.

Boisserie, J.R., Fisher, R.E., Lihoreau, F., Weston, E.M., 2011. Evolving between land and water: key questions on the emergence and history of the hippopotamidae (hippopotamoidea, cetancodonta, cetartiodactyla). Biological Reviews 86, 3, 601–625.

Briggs, D.E.G., Siveter, David J., Siveter, Derek J., and Sutton, M.D., 2008. Virtual fossils from a 425 million- year-old volcanic ash: American Scientist 96, 474–481.

Brown P., Sutikna T., Morwood M.J., Soejono, R. P., Jatmiko, Wayhu Saptomo, E., Awe Due, R., 2004. A new small-bodied hominin from the Late Pleistocene of Flores, Indonesia. Nature 403, 1055–61.

Caloi, L., Palombo, M.R., 1985. Osservazioni sugli ippopotami nani delle isole del Mediterraneo. Geologica Romana 22, 45–83.

Caloi, L., Palombo, M.R., 1996. Functional aspect and ecological implications in Pleistocene endemic herbivores of Mediterranean islands. Historical Biology 8, 151–172.

Capasso Barbato, L., Kotsakis, T., Petronio, C., 1982. Nuovi resti e osservazioni filogenetiche su *Hippopotamus creutzburgi* Boekschoten & Sondaar (Hippopotamidae, Mammalia) del Pleistocene di Creta (Grecia). Geologica Romana 21, 61-77.

Cunningham, J.A., Rahman, I.A., Lautenschlager, S., Rayfield, E.J., Donoghue, P.C., 2014. A virtual world of paleontology. Trends in Ecology and Evolution 29, 347–357.

Depéret C., 1921. La phylogénie des Hippopotames. Bulletin de la Société géologique de France 21, 163–165.

Dermitzakis, M., Pavlakis, P., Drinia., H., 2005. The Pleistocene hippopotamids of the Katharo Plateau, Lasithi, Crete. Preliminary Report. Proceedings of the 2nd Cretan Speleological Symposium in memoriam of Eleftherios Platakis, May 29, Irakleion, Crete, Greece.

Desmarest, A.G., 1822. Mammalogie, ou description des espèces de mammifères. Agasse, Paris.

De Vos J., 1979. The endemic Pleistocene deer of Crete. Proceedings of the Koninklijke Akademie van Wetenschappen (Series B) 82, 59–90.

De Vos, J., Dermitzakis, M.D., 1986. Models of the development of Pleistocene deer on Crete (Greece). Modern Geology 10, 243–248.

DeVries, R.P., Sereno, P.C., Vidal, D., Baumgart, S.L., 2022. Reproducible digital restoration of fossils using Blender. Frontal of Earth Science 10, 138.

Díez Díaz, V., Mallison, H., Asbach, P., Schwarz, D., Blanco, A., 2021. Comparing surface digitization techniques in palaeontology using visual perceptual metrics and distance computations between 3D meshes. Palaeontology 64, 179–202.

Dryden, I. L., & Mardia, K. M. (2008). Statistical shape analysis. Chicester, Wiley.

Emerson, S.B., Bramble, D.M., 1993. Scaling, allometry and skull design. In: Hanken J., Hall, B.K., eds. The skull, Vol. 3. Chicago: University of Chicago Press, pp. 384–421.

Falconer, H., 1868. On the fossil remains of *Elephas melitensis*, an extinct pygmy species of elephant; and other Mammalia, & c. from the ossiferous caves of Malta. In: Murchison C. (ed) Palæontolgical memoires and notes of the late Hugh Falconer, A.M., M.D., with a biographical sketch of the author 2, pp. 292–307.

Falkingham, P.L., 2012, Acquisition of high resolution 3D models using free, open-source, photogrammetric software: Palaeontologia Electronica 15, 1–15.

Green, D.J., and Alemseged, Z., 2012. Australopithecus afarensis scapular ontogeny, function, and the role of climbing in human evolution. Science 338, 514–517.

Gregory, W.K., 1951. Evolution emerging, MacMillan Press, US, New York.

Haring, A., Exner, U., and Harzhauser, M., 2009. Surveying a fossil oyster reef using terrestrial laser scanning. Geophysical Research Abstracts 11, 10714.

Hooijer, D.A., 1946. Notes on some Pontian mammals from Sicily figured by Seguenza. Archives néerlandaises de Zoologie 7, 301–333.

Houtekamer, J.L. and Sondaar, P.Y., 1979. Osteology of the fore limb of the Pleistocene dwarf hippopotamus from Cyprus with special references to phylogeny and function. I—II. Proceedings of the Kominklijke Nederlands Akademie van Wetenschappen (Series B) 82, 411–468.

Iliopoulos, G., Eikamp, H., Fassouls, Ch., 2010. A new Pleistocene mammal locality from Western Crete. Bulletin of the Geological Society of Greece 5, 918–925.

Kaifu, Y., Baba H., Sutikna, T., Morwood, J., Kubo, D., Saptomo, E. W., Jatmiko, Y. D., Due Awe, R., Djubiantono., T., 2011. Craniofacial 34 morphology of *Homo floresiensis*: description, taxonomic affinities, and evolutionary implication. Journal of Human Evolution 61, 644–82.

Kingdon, J., 1979. Hippopotamids. In: Kingdon, J. (Ed.), East African mammals, 3B, Academic Press, London, pp. 250–277.

Kingsland, K., 2020. Comparative analysis of digital photogrammetry software for cultural heritage. Digital Applications in Archaeological and Cultural Heritage, 18, e00157.

Konidaris, G., Tourloukis, V., Boni, G., Athanassiou, A., Giusti., D., Thompson., N. C., Syrides, G., Panagopoulou, E., Karkanas, P., Harvati, K., 2023. Marathousa 2: A new Middle Pleistocene locality in the Megalopolis Basin (Greece) with evidence of hominin exploitation of megafauna (Hippopotamus).

Kuss, S.E., 1975a. *Hippopotamus creutzburgi parvus* n. spp., ein pleistozänes Zwergflußpferd von der Insel Kreta. Berichte der naturforschenden Gesellschaft zu Freiburg im Breisgau 65, 1-2, 5–23.

Lax, E., 1996. A gazetteer of Cretan paleontological localities. In Reece, D. (Ed.) Pleistocene and Holocene Fauna of Crete and its first Settlers. Monographs in World Archaeology, Prehistory Press 28, pp. 1–32.

Jarvik, E., 1954. On the Visceral Skeleton in Eusthenopteron with a Discussion of the Parasphenoid and Palatoquadrate in Fishes, Almqvist and Wiksell.

Johnson, D.L., 1980. Problems in the land vertebrate zoogeography of certain islands and the swimming powers of elephants. Journal of Biogeography 7, 383–398.

Laws, R.M., 1968. Dentition and ageing of the hippopotamus. African Journal of Ecology 6, 19–52.

Lomolino, M. V., 2000. Ecology's most general, yet protean pattern: the species-area relationship. Journal of Biogeography 27, 17–26.

Lomolino, M.V., van der Geer, A.A.E., Lyras G.A., Palombo, M. R., Sax, D. F., Rozzi, R., 2013. Of mice and mammoths: generality and antiquity of the island rule. Journal of Biogeography 40, 1427–1439.

Lyras, G.A., 2018. Brain changes during phyletic dwarfing in elephants and hippos. Brain, Behavior and Evolution 92, 167–181.

Lyras, G.A., Dermitzakis, M.D., van der Geer, A.A.E., van der Geer, S.B., de Vos, J., 2009. The origin of *Homo floresiensis* and its relation to evolutionary processes under isolation. Anthropological Science 117, 33–43.

Lyras, G.A., Athanassiou A., van der Geer, A.A.E., 2021. The fossil record of insular endemic mammals from Greece. In: Vlachos E., ed., Fossil vertebrates of Greece, Vol. 2, Laurasiatherians, artiodactyls, perissodactyls, carnivorans, and island endemics. Cham: Springer Nature, Switzerland, pp. 661–701.

Mallison, H., Hohloch, A., and Pfretzschner, H., 2009. Mechanical digitizing for paleontology—New and improved techniques: Palaeontologia Electronica 12, 2, 41.

Martino, R., Pignatti, J., Rook, L., and Pandolfi, L., 2021. Hippopotamid dispersal across the Mediterranean in the latest Miocene: a re-evaluation of the Gravitelli record from Sicily, Italy. Acta Palaeontologica Polonica 66.

Makris, D., Skaltsas, I., Fotiou, S., Karampinis, L., Vlachou, M.A., 2018. Digitization of Athens School of Fine Arts Artworks Based on Optical 3-D Scanning and Photogrammetry. In Proceedings of the 9th International Conference on Information, Intelligence, Systems and Applications (IISA), Zakynthos, pp. 1–7.

Makris, D., Sakellariou, C., Karampinis, L., 2021. Emerging materiality through dynamic digital conservation. Digital Applications in Archaeology and Cultural Heritage 23, 2, e00198.

Marra, A. C., 2005b. Pleistocene Hippopotamuses of Mediterranean islands: looking for ancestors. In *Alconer*, J. A. and Bover, P. (Eds.): Proceedings of the International Symposium "Insular Vertebrate Evolution: the Palaeontological Approach": Monografies de la Societat d'Història Natural de les Balears 12, pp. 193–204.

Mazza, P., 1995. New evidence on the Pleistocene hippopotamuses of Western Europe. Geologica Romana 31, 61–241.

Melentis, J. K., 1965. Über *Hippopotamus antiquus* Desmarest aus dem Mittelpleistozän des Beckens von Megalopolis in Peloponnes (Griechenland). Annales Geologique des Pays Hellenic 16, 403–435.

Mol, D., de Vos, J., van den Bergh, G.D., Sondaar, P.Y., 1996. The taxonomy and ancestry of the fossil elephants of Crete. Faunal turnover and comparison with Proboscidean faunas of Indonesian islands. In: Reese D.S. (ed.), Pleistocene and Holocene fauna of Crete and its first settlers. Monographs in World Archaeology 28. Prehistory Press, Madison, pp. 1–32.

Nyakatura, J.A., Allen, V.R., Lauströer, J., Andikfar, A., Danczak, M., Ullrich, H. J., Hufenbach, W., Martens., T., Fischer, M., S., 2015. A Three-Dimensional Skeletal Reconstruction of the Stem Amniote *Orobates pabsti* (Diadectidae): Analyses of Body Mass, Centre of Mass Position, and Joint Mobility. PLOS ONE 10, 9, e0137284.

Osborn, H. F., 1907. Evolution of mammalian molar teeth. Biological Studies and Addresses 1. The Macmillan Company, London.

Palombo, M. R., Moncunill-Solé, B., 2023. Dwarfing and gigantism in quaternary vertebrates, Reference Module in Earth Systems and Environmental Sciences.

Psarianos P., 1961. Karstphanomenen Griechenlands. II. Die Polje von Lassithi (Kreta). Annales Geologiques des Pays Helleniques 12, 105–121.

Psonis N., Vassou D., Nicolaou L., Roussiakis S., Iliopoulos G., Poulakakis N., Sfenthourakis S., 2021. Mitochondrial sequences of the extinct Cypriot pygmy hippopotamus confirm its phylogenetic placement. Zoological Journal of the Linnean Society 196, 979–989.

Poulakakis, N., Mylonas, M., Lymberakis, P., Fassoulas, C., 2002. Origin and taxonomy of the fossil elephants of the island of Crete (Greece): problems and perspectives. Palaeogeography Palaeoclimatology Palaeoecology 186, 163–183.

Rakotovao, M., Lignereux, Y., Orliac, M.J., Duranthon, F., Antoine, P.O., 2014. Hippopotamus lemerlei Grandidier, 1868 et Hippopotamus madagascariensis Guldberg, 1883 (Mammalia, Hippopotamidae): Anatomie crânio-dentaire et révision systématique. Geodiversitas 36, 1, 117–161.

Raulin, F.V., 1869. Description physique de l'île de Crète. Bertrand, Paris.

Simmons A.H. 1988. Extinct pygmy hippopotamus and early man in Cyprus. Nature 333, 554–557.

Ravosa, M.J., 1991. The ontogeny of cranial sexual dimorphism in two Old World monkeys: *Macaca fascicularis* (Cerocopithecinae) and *Nasalis larvatus* (Colobinae). International Journal of Primatology 12, 403–426.

Reese, D.S., 1974. New Sites and Finds from the Pleistocene in Cyprus. Manuscript on file, Cyprus American Archaeological Research Institute, Nicosia.

Reese, D.S., Belluomini, G., Ikeya M., 1996. Absolute Dates for the Pleistocene Fauna of Crete. In: Reese D.S. (ed.), Pleistocene and Holocene fauna of Crete and its first settlers. Monographs in world Archaeology 28, 47–52. Prehistory Press, Madison.

Sollas, W.J., 1903. A method for the investigation of fossils by serial sections: Philosophical Transactions of the Royal Society of London (Series B) 196, 259–265.

Spaan, A., 1996. Hippopotamus creutzburgi: the case of the Cretan Hippopotamus. In: Reese D.S. (ed.), Pleistocene and Holocene Fauna of Crete and its First Settlers. Monographs in World Archaeology, 28. Madison, Wisconsin: Prehistory Press, pp. 99–111.

Spratt, T.A.B., 1865. Travels and researches in Crete. John van Voorst, London.

Stuenes, S., 1989. Taxonomy, habits, and relationships of the subfossil Madagascan hippopoptami *Hippopotamus lemerlei* and *H. madagascariensis*. Journal of Vertabrate Paleontology 9, 241–268.

Sutton, M.D., 2008. Tomographic techniques for the study of exceptionally preserved fossils: Proceedings of the Royal Society, Series B, 275, 1587–1593.

Sutton, M.D., Rahman, I.A., and Garwood, R.J., 2014. Techniques for Virtual Palaeontology: Oxford, UK, Wiley-Blackwell, 208.

Symeonides, N.K., Sondaar P.Y., 1975. A new otter from the Pleistocene of Crete. Annales Géologiques des Pays Helléniques 27, 11–24.

Thenius, E., Hoffer H., 1960. Stammesgeschichte der Säugetiere. Springer-Verlag, Berlin.

von Zittel, K.A., 1925. Text book of paleontology. III Mammalia. MacMillan, London.

van der Geer, A.A.E., Lyras, G.A., de Vos, J., Dermitzakis, M., 2010. Evolution of Island Mammals: Adaptation and Extinction of Placental Mammals on Islands. Hoboken N.J., John Wiley & Sons.

van der Geer, A.A.E., Lyras, G.A., 2011. Field Trip Guidebook. 9th Annual Meeting of the European Association of Vertebrate Palaeontologists, Heraklion, Crete, 14-19 June 2011.

van der Geer, A.A.E., Lyras, G.A., van den Hoek Ostende, L.W., de Vos, J., Drinia, H., 2014. A dwarf elephant and a rock mouse on Naxos (Cyclades, Greece) with a revision of the palaeozoogeography of the Cycladic Islands (Greece) during the Pleistocene. Palaeogeography, Palaeoclimatology, Palaeoecology 404, 133–144.

van der Geer, A.A.E., 2014. Parallel patterns and trends in functional structures in extinct island mammals. Integrative Zoology 9, 167–182.

van der Geer, A.A.E., Lyras, G.A., Mitteroecker, P., MacPhee, R.D.E., 2018. From Jumbo to Dumbo: cranial shape changes in elephants and hippos during phyletic dwarfing. Evolutionary Biology 45, 303–317.

van der Geer, A.A.E., Lyras, G.A., Vos, J. de, Dermitzakis, M., 2021.Evolution of Island Mammals. Adaptation and Extinction of Placental Mammals on Islands, Second Edition, Hoboken NJ, John Wiley & Sons, pp. 57–81.

van der Geer, A.A.E., van den Bergh, G.D., Lyras, G.A., Prasetyo, U.W., Due, R.A., Setiyabudi, E., Drinia, H., 2016. The effect of area and isolation on insular dwarf proboscideans. Journal of Biogeography 43, 1656–1666.

van der Made J., Sahnouni M., Boulaghraief K., 2017. Hippopotamus gorgops from El Kherba (Algeria) and the context of its biogeography. In: Sahnouni M., Semaw S., Garaizar J.R., editors. Proceedings of the II Meeting of African History (Burgos15-16 April 2015), Centro Nacional de Investigación sobre la Evolución Humana, Consorcio CENIEH. Burgos: Gráficas Eujos, 137–68.

Van Valen, L.M., 1973. Pattern and the balance of nature. Evolutionary Theory 1, 31–49.

Weston, E. M., 1998. A biometrical analysis of evolutionary change within the Hippopotamidae. PhD thesis, University of Cambridge, England.

Weston, E.M., 2003. Evolution of ontogeny in the hippopotamus skull: using allometry to dissect developmental change. Biological Journal of the Linnean Society 80, 625–638.

Weston, E. M. and Lister, A.M., 2009. Insular dwarfism in hippos and a model for brain size reduction *Homo floresiensis*. Nature 459, 85–88.

Appendix I

Species	Specimen	Locality	Developmental Stage	Gender
Ch. liberiensis	AMNH (M) 146849		Adult (Stage XVI)	Female
Ch. liberiensis	AMNH (M) 148452		Adult (Stage XVI)	Male
Ch. liberiensis	AMNH (M) 185383		Juvenile (Stage II)	Female
Ch. liberiensis	AMNH (M) 2423		Juvenile (Stage IV)	
Ch. liberiensis	FMNH 122614		Juvenile (Stage I)	
Ch. liberiensis	FMNH 174408		Adult (Stage XVII)	Male
Ch. liberiensis	MFN ZMB 46517		Juvenile (Stage I)	
H. amphibius	AMNH (M) 24282		Adult (Stage N/A)	Male
H. amphibius	AMNH (M) 466		Adult (Stage N/A)	
H. amphibius	AMNH (M) 54248		Juvenile (Stage IX)	Male
H. amphibius	AMNH (M) 54249		Juvenile (Stage VII)	Male
H. amphibius	AMNH (M) 80813		Juvenile (Stage IX)	
H. amphibius	AMNH (M) 81858		Adult (Stage N/A)	Male
H. amphibius	AMNH (M) 90230		Juvenile (Stage VII)	Female
H. amphibius	AMNH (M) 99637		Adult (Stage N/A)	
H. amphibius	AMPG teaching coll. H.a.1		Adult (Stage N/A)	
H. amphibius	AMPG teaching coll. H.a.2		Adult (Stage XIV)	
H. amphibius	FMNH 22367		Adult (Stage XVII)	
H. amphibius	FMNH 34927		Adult (Stage XVIII)	
H. amphibius	RMNH 1000		Adult (Stage XIII)	
H. amphibius	RMNH 11758		Adult (Stage N/A)	Male
H. amphibius	RMNH cat ost. ad		Adult (Stage N/A)	
H. amphibius	RMNH cat ost. b		Juvenile (Stage X)	
H. amphibius	USNM 123387		Adult (Stage XIII)	Male
H. amphibius	USNM 162977		Adult (Stage XI)	Female
H. amphibius	USNM 162980		Adult (Stage XI)	Female
H. amphibius	USNM 254978		Juvenile (Stage IX)	Female
H. amphibius	MFN ZMB 43132		Adult (Stage XII)	
H. lemerlei	AMPG (V) 939	Madagascar	Adult (Stage XVIII)	
H. lemerlei	MFN MBMa 308a	Madagascar	Juvenile (Stage VIII)	
H. madagascariensis	MFN MBMa 42517	Madagascar	Adult (Stage XIV)	
H. madagascariensis	MNHN Mad 7352	Madagascar	Adult (Stage XIV)	
H. minor	AMPG dkm c	Cyprus	Adult (Stage XV)	
H. creutzburgi	KA-A-109	Crete	Adult (Stage XVII)	

AMPG(V) Museum of Palaeontology and Geology, University of Athens (Greece); MGG Museo Geologigo G.G. Gemmelaro, Palermo (Italy); MFN Museum für Naturkunde, Berlin (Germany); MNHN Muséum National d'Histoire Naturelle, Paris (France); SFN Senckenberg Forschungsinstitut und Naturmuseum, Frankfurt (Germany); SMNS Staatliches Museum für Naturkunde, Stuttgart (Germany).

Appendix II

Specimen	Alignment Time	Overall Processing Time	Texturing Time	Overall Time	Registered Images	Faces	Vertices	Mean Edge Length (mm)
PCUP.14.77	07m:14s	6m:38s	03m:15s	17m:07s	332/337	4,791,106	2,395,551	0.37
KA-A-109	18m:44s	25m:59s	05m:29s	50m:12s	599/643	3,615,684	1,807,842	0.42
KA-A-109 (Broken Part)	04m:54s	16m:58s	03m:53s	25m:45s	538/538	5,555,314	2,777,659	0.12
KA-A-105	08m:59s	25m:59s	05:26s	40m:24s	361/372	4,647,021	2,325,739	0.3
KA-A-106	11m:25s	17m:16s	06m:01s	34m:42s	603/626	4,343,112	2,171,554	0.4

Reports from Reality Capture.

Appendix III

Length (mm)	Skull	Muzzle	Orbit	Face
H. amphibius	458.75	257.73	62	257
H. creutzburgi	296.212	143.466	58	173

Skull and muzzle measurements for the muzzle to skull ratios.